REVIEWS OF MODERN PHYSICS, VOLUME 93, APRIL–JUNE 2021

Near-field radiative heat transfer in many-body systems

S.-A. Biehs

Institut für Physik, Carl von Ossietzky Universität,
D-26111 Oldenburg, Germany

R. Messina

Laboratoire Charles Fabry, UMR 8501,
Institut d'Optique, CNRS, Université Paris–Saclay,
2 Avenue Augustin Fresnel, 91127 Palaiseau Cedex, France

P. S. Venkataram and A. W. Rodriguez

Department of Electrical Engineering,
Princeton University, Princeton, New Jersey 08544, USA

J. C. Cuevas

Departamento de Física Teórica de la Materia
Condensada and Condensed Matter Physics Center (IFIMAC),
Universidad Autónoma de Madrid, E-28049 Madrid, Spain

P. Ben-Abdallah*

Laboratoire Charles Fabry, UMR 8501,
Institut d'Optique, CNRS, Université Paris–Saclay,
2 Avenue Augustin Fresnel, 91127 Palaiseau Cedex, France
and Université de Sherbrooke, Department of Mechanical Engineering,
Sherbrooke, Québec J1K 2R1, Canada

(published 16 June 2021)

Many-body physics aims to understand emergent properties of systems made of many interacting objects. This review examines recent progress on the topic of radiative heat transfer in many-body systems consisting of thermal emitters interacting in the near-field regime. Near-field radiative heat transfer is a rapidly emerging field of research in which the cooperative behavior of emitters gives rise to peculiar effects that can be exploited to control heat flow at the nanoscale. Using an extension of the standard Polder and van Hove stochastic formalism to deal with thermally generated fields in N-body systems, along with their mutual interactions through multiple scattering, a generalized Landauer-like theory is derived to describe heat exchange mediated by thermal photons in arbitrary reciprocal and nonreciprocal multiterminal systems. In this review, this formalism is used to address both transport and dynamics in these systems from a unified perspective. The discussion covers (i) the description of nonadditivity of heat flux and its related effects, including fundamental limits as well as the role of nanostructuring and material choice; (ii) the study of equilibrium states and multistable states; (iii) the relaxation dynamics (thermalization) toward local and global equilibria; (iv) the analysis of heat transport regimes in ordered and disordered systems composed of a large number of objects, density, and range of interactions; and (v) the description of thermomagnetic effects in magneto-optical systems and heat transport mechanisms in non-Hermitian many-body systems. The review concludes with a listing of outstanding challenges and promising future research directions.

DOI: 10.1103/RevModPhys.93.025009

CONTENTS

---

*pba@institutoptique.fr

I. INTRODUCTION

Heat transfer in a given system is in its simplest sense [i.e., ignoring any cross-coupling between the different irreversible transport processes (Onsager, 1931)] thermal energy in transit due to a spatial temperature difference (Bergman *et al.*, 2011). There are three basic heat-transfer modes: *conduction*, *convection*, and *radiation*. In the case of a stationary medium, which could be a solid or a fluid, conduction refers to heat transfer through local agitation of atoms or charges that occurs across the medium in response to a temperature difference. Ultimately, the carriers responsible for heat conduction are phonons, molecular vibrations, or electrons or ions in the case of electrical conductors. The second mode of transport is convection and refers to heat transfer that occurs between a surface and a moving fluid when they are at different temperatures (or by advection inside the fluid itself). Finally, the third heat-transfer mechanism is *thermal radiation*, which is the topic of this review. All bodies at a finite temperature emit energy in the form of electromagnetic waves (or photons). Hence, even in the absence of an intervening medium, there is always heat transfer via thermal radiation between bodies at different temperatures. This makes thermal radiation one of the most ubiquitous physical phenomena and its understanding of critical importance in many different areas of science and engineering (Zhang, 2007; Modest, 2013; Howell, Mengüç, and Siegel, 2016).

Traditionally, our understanding of thermal radiation is based on Planck's law (Planck, 1914), which establishes that a blackbody (an object that absorbs all the radiation that impinges on it) emits thermal radiation following a broadband distribution that depends only on the body's temperature. Planck's law provides a unified description of a variety of thermal-radiation phenomena and, in particular, it sets an upper limit (Stefan-Boltzmann's law) for the radiative heat transfer (RHT) between bodies. However, Planck's law was derived using ray optics, and hence it is expected to fail when the spatial dimensions in a thermal problem are smaller than or comparable to the thermal wavelength λ_{Th} defined by Wien's displacement law ($\sim 10\ \mu$m at room temperature) (Planck, 1914). In particular, Planck's law fails to describe RHT between objects separated by distances $\lesssim \lambda_{\mathrm{Th}}$; for a detailed discussion, see Pendry (1999) and Volokitin and Persson (2007). In this *near-field* regime, RHT can be dominated by evanescent waves (or photon tunneling), not taken into account in Planck's law, and the Planckian (or blackbody) limit can be greatly overcome by bringing objects sufficiently close; see Fig. 1. This phenomenon was first predicted within the rigorous framework of fluctuational electrodynamics (FE)

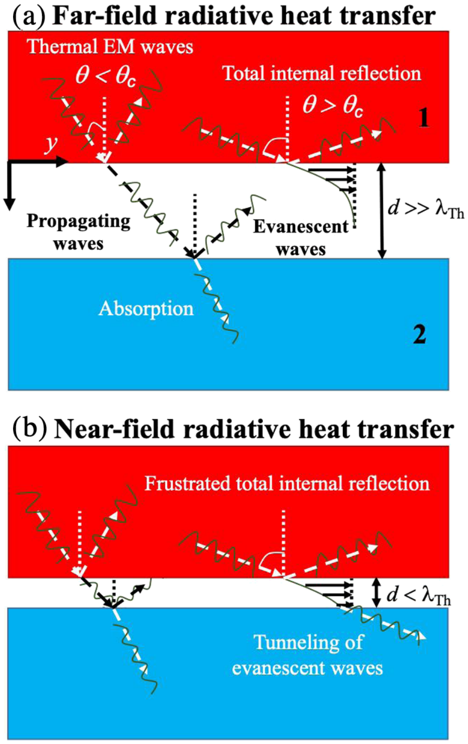

FIG. 1. (a) Far-field radiative heat transfer between two infinite parallel plates (media 1 and 2) separated by a vacuum gap. In this scenario, the gap size d is much larger than the thermal wavelength λ_{Th}, and the two plates exchange heat only via propagating waves. The evanescent waves generated in the vacuum gap by total internal reflection are not able to reach the second plate and do not contribute to the heat transfer. (b) When $d < \lambda_{\mathrm{Th}}$ the tunneling of evanescent waves can give a significant contribution to the radiative heat transfer and in this way the Planckian (or blackbody) limit can be greatly overcome in this near-field regime.

(Rytov, Kravtsov, and Tatarskii, 1989) by Polder and van Hove in the early 1970s (Polder and van Hove, 1971); see Sec. II. This near-field radiative heat transfer (NFRHT) enhancement was first hinted at in several experiments in the late 1960s (Hargreaves, 1969; Domoto, Boehm, and Tien, 1970), but it was not firmly confirmed until the 2000s (Kittel *et al.*, 2005; Hu *et al.*, 2008; Narayanaswamy, Shen, and Chen, 2008; Rousseau *et al.*, 2009; Shen, Narayanaswamy, and Chen, 2009). Since then, numerous experiments exploring different aspects of NFRHT have been reported and have boosted the field of thermal radiation (Ottens *et al.*, 2011; Guha *et al.*, 2012; Kralik *et al.*, 2012; Shen *et al.*, 2012; van Zwol, Ranno, and Chevrier, 2012; van Zwol *et al.*, 2012; Shi *et al.*, 2013; Worbes, Hellmann, and Kittel, 2013; St-Gelais *et al.*, 2014, 2016; Ito *et al.*, 2015; Kim *et al.*, 2015; Lim, Lee, and Lee, 2015; Song *et al.*, 2015, 2016; Bernardi, Milovich, and Francoeur, 2016; Ito *et al.*, 2017; Králík *et al.*, 2017; Lang *et al.*, 2017; Fiorino *et al.*, 2018; Fiorino, Thompson *et al.*, 2018; Fiorino, Zhu *et al.*, 2018; Ghashami *et al.*, 2018; DeSutter, Tang, and Francoeur, 2019; Musilová *et al.*, 2019; Salihoglu *et al.*, 2020). These experiments have, in turn, generated hope that NFRHT may have an impact on different technologies such as heat-assisted magnetic recording, thermal lithography, scanning thermal microscopy, coherent thermal sources, near-field-based thermal management, thermophotovoltaics, and other energy-conversion devices; see Basu, Zhang, and Fu (2009), Song, Fiorino *et al.* (2015), Cuevas and García-Vidal (2018), and Komiyama (2019) and references therein.

In parallel to these experimental advances, over the last two decades there has been a significant amount of theoretical activity. Initially, attention was devoted to the importance of choice of materials and the elucidation of the different mechanisms of near-field thermal radiation. In that regard, polar dielectrics exhibiting polaritonic resonances that lead to surface modes have played a prominent role in this field (Mulet *et al.*, 2002). Then, following nanophotonics concepts, a lot of work has been devoted to assess the possibility of further enhancing NFRHT and to tune its spectral properties by using nanostructures such as thin films and multilayer systems (Biehs, 2007; Biehs, Reddig, and Holthaus, 2007; Volokitin and Persson, 2007; Francoeur, Mengüç, and Vaillon, 2008; Ben-Abdallah *et al.*, 2009a; Maslovski, Simovski, and Tretyakov, 2013), photonic crystals and gratings (Ben-Abdallah, Joulain, and Pryamikov, 2010; Biehs *et al.*, 2011; Rodriguez *et al.*, 2011; Guérout *et al.*, 2012; Messina, Noto *et al.*, 2017), and metasurfaces (Liu and Zhang, 2015a; Dai *et al.*, 2016; Fernández-Hurtado *et al.*, 2017). The investigation of the use of metamaterials for further enhancing NFRHT (Joulain, Drevillon, and Ben-Abdallah, 2010; Biehs *et al.*, 2011; Biehs, Tschikin, and Ben-Abdallah, 2012; Guo *et al.*, 2012) or low-dimensional materials like graphene or phosphorene to tune NFRHT (Volokitin and Persson, 2011; Ilic *et al.*, 2012a; Svetovoy, van Zwol, and Chevrier, 2012; Liu, Zhang, and Zhang, 2014a; Rodriguez-Lopez, Tse, and Dalvit, 2015; Zhang, Yi, and Tan, 2018; Liu, Shen, and Xuan, 2019) has also attracted significant attention. Another topic of great importance has been the study of the active control of NFRHT by different means, including the use of phase-transition materials (van Zwol, Joulain, Ben Abdallah, Greffet, and Chevrier, 2011; van Zwol, Joulain, Ben-Abdallah, and Chevrier, 2011; Menges *et al.*, 2016), the application of an external magnetic field (Moncada-Villa *et al.*, 2015), or the regulation of chemical potentials for photons with an external bias (Chen *et al.*, 2015). There are also several theoretical proposals for functional devices that make use of NFRHT for thermal management (Otey, Lau, and Fan, 2010; Ben-Abdallah and Biehs, 2015), thermophotovoltaics (Narayanaswamy and Chen, 2003; Laroche, Carminati, and Greffet, 2006; Basu, Chen, and Zhang, 2007; Zhao, Chen *et al.*, 2017), and other energy applications (Chen *et al.*, 2015; Chen, Santhanam, and Fan, 2016). On a more fundamental level, quantum approaches based on the Huttner-Barnett model, quantum Langevin equations, the nonequilibrium Green's function method, and the master-equation approach for open quantum systems have been proposed (Janowicz, Reddig, and Holthaus, 2003; Biehs and Agarwal, 2013a; Sääskilahti, Oksanen, and Tulkki, 2014; Barton, 2016; Wang and Peng, 2017; Sasihithlu and Agarwal, 2018).

From a broader perspective, a new general picture of RHT has emerged in recent years with profound similarities to other heat and charge transport phenomena, including phonon conduction in nanoscale systems and coherent electronic transport in mesoscopic devices (Cuevas and Scheer, 2017). In particular, RHT is now routinely described in terms of the Landauer formula, originally proposed in the context of electronic mesoscopic systems (Datta, 1997; Imry and Landauer, 1999), where the energy and charge transport are determined mainly by the transmission function describing the transfer probability of the carriers. Moreover, techniques employed to compute transmission functions (scattering approaches, Green's function techniques, etc.) are conceptually similar in all those contexts. This connection between RHT and conduction not only allows us to profit from the experience in other fields but can also serve as the starting point for a unified description of different heat-transfer modes in situations where different types of carriers may compete or even interfere. An example of this type of situation is realized in the context of the heat transfer in subnanometer gaps where recent experiments have reported conflicting observations in an intermediate regime where the contribution of different carriers (photons, phonons, and electrons) may be comparable (Cui, Jeong, Fernández-Hurtado *et al.*, 2017; Kloppstech *et al.*, 2017). While the situation seems to be clear in the limiting cases where either conduction (Cui, Jeong, Hur *et al.*, 2017; Mosso *et al.*, 2017; Cui *et al.*, 2019) or NFRHT (Kim *et al.*, 2015) is expected to dominate, the description of the crossover between them might require novel theories where different carriers are treated on an equal footing (Chiloyan *et al.*, 2015; Venkataram *et al.*, 2018).

Conceptually speaking, a major advance in the field in the last decade has been the development of theoretical models of RHT in many-body systems, which is the central topic of this review. Such a theory deals with radiative heat exchange in systems composed of multiple thermal emitters able to cooperatively interact. The collective behaviors in these systems give rise to singular phenomena that we discuss in this review. Until 2011, FE had been primarily used to describe RHT between two bodies, but the situation changed with the report of the first version of a many-body theory of

RHT describing a collection of small dipolar particles (Ben-Abdallah, Biehs, and Joulain, 2011). Soon after, this many-body theory was generalized to deal with bodies of arbitrary size and shape (Messina and Antezza, 2011a; Krüger *et al.*, 2012), and new refinements of the theory are constantly being reported to deal with more complex optical materials. Again, there is an analogy here with developments in mesoscopic physics, where Büttiker's extension of the Landauer formalism to multiterminal systems laid down the basis for the understanding of numerous charge and energy transport phenomena in mesoscopic systems (Datta, 1997). As we discuss in this review, the many-body theory of NFRHT opened the door for predicting and analyzing a plethora of novel physical phenomena with no analogs in two-body systems. Thus, for instance, it became possible to explore thermal analogs of intrinsic many-body phenomena like the Hall effect (Ben-Abdallah, 2016) and heat persistent current (Zhu and Fan, 2016). It has also made it possible to propose a wide range of thermal functional devices that are intrinsically many body in nature, such as the thermal transistor (Ben-Abdallah and Biehs, 2014). This theory also allowed us to understand for the first time the different heat propagation regimes in disordered systems involving a large collection of objects and paved the way for hydrodynamic modeling of transport in these media. Although recent experimental works have explored the possibility of tuning radiative heat transfers in many-body systems (Thompson *et al.*, 2020) by actively changing the relative position of nearby objects, to our knowledge many-body systems have yet to be experimentally investigated in the purely near-field regime.

The field of NFRHT has been the subject of different reviews over the years. Reviews by Joulain *et al.* (2005) and Volokitin and Persson (2007) covered the FE theory and basic concepts of NFRHT but do not include crucial theoretical and experimental advances achieved in recent years. Reviews by Basu, Chen, and Zhang (2007) and Ben-Abdallah and Biehs (2019) focused on potential applications of near-field thermal radiation in thermophotovoltaics. There are recent reviews like that of Song, Fiorino *et al.* (2015) that already presented some of the most recent advances and, in particular, described the main experimental techniques developed in recent years. The review by Cuevas and García-Vidal (2018) provided an interesting and updated perspective of the field but did not contain an in-depth description of theoretical developments. This review focuses on the theory of NFRHT in many-body systems, which has not been covered thus far in a self-contained and unified framework. This topic is becoming a central focus of the field of thermal radiation, as it promises an entirely new generation of thermal-radiation applications, and its understanding is likely to determine the future of RHT as a forefront research line.

The structure of the review is as follows. In Sec. II, we set the stage for this review by discussing NFRHT in two-body systems. Here we put the emphasis on the modern view of NFRHT and review the most important theoretical advances in this topic, as well as the experimental state of the art. Specifically, we begin by recalling the basics of the theory of FE and then discussing its application to the important case of two parallel plates (Sec. II.A). This basic configuration is used to illustrate the critical role of material choice (Sec. II.B), including a preliminary discussion of nonreciprocal materials in Sec. II.C. Section II.D is devoted to an analysis of the role of nanostructuring in tailoring and, most importantly, enhancing NFRHT, including recent works focused on multilayer structures, photonic crystals, metamaterials, gratings, metasurfaces, graphene sheets, and surface roughness. We then move beyond planar structures in Sec. II.E to discuss NFRHT between objects of arbitrary size and shape. General-purpose numerical methods developed to date for the description of NFRHT in arbitrary geometries are then discussed in Sec. II.F. We conclude this first part of the review in Sec. II.G with an in-depth discussion of recently derived limits on the largest NFRHT rates that could ever be realized by an optimal choice of material and geometric configuration. Specifically, we highlight the prohibitive role that multiple scattering (a critical feature of many-body physics that is further discussed in subsequent sections) plays in limiting heat-transfer enhancements that may be achieved through nanostructuring, resulting in optimal flux rates not much larger than what is observed in planar polaritonic materials, at least in the context of two-body heat exchange.

Section III constitutes the bulk of this review and covers a variety of aspects of the theory of near-field thermal radiation in many-body systems. We first discuss the problem of light absorption with a set of nonemitting objects that collectively interact and show that these systems can be treated as a whole with a dressed susceptibility that takes into account both cooperative interactions and the resonant response of individual objects. Next a generalized Landauer formula is derived to describe radiative heat transfer in the general situation in which all objects are emitting, using transmission coefficients describing the pairwise efficiency of coupling between any two objects. Using this theoretical framework, we highlight the singular aspects of heat transport in these systems compared to those seen in two-body systems. We illustrate these peculiarities in Secs. III.A.3 and III.B.2, where we prove the nonadditivity of heat flux, a fundamental feature of these systems. We also show that N-body interactions can amplify heat flux or lead to saturation mechanisms close to the contact without the need to introduce nonlocality in material responsivity. In Sec. III.B.3, we discuss equilibrium conditions for any given system and show that equilibrium states are generally not unique and can be, along with their stability, identified and characterized by standard perturbative techniques. We also show that multistable systems can be exploited to make a Boolean treatment of information with thermal photons or build thermal self-oscillators. In Sec. III.C, we address the problem of heat transport in various complex systems using both a kinetic approach, based on the approximate Boltzmann transport equation for the resonant modes supported by the system, and a generalized Landauer theory that takes into account all modes in the continuum. Several physical effects (radiative drag effect, heat-flux focusing, heat pumping, and long-range heat transport) inherent to many-body systems are then introduced and discussed. In Sec. III.C.4, we address the relaxation problem of many-body systems and show that the temperature field can evolve at different timescales, depending on the nature of the interactions. Furthermore, we discuss the current solutions proposed to dynamically control the heat flux exchanged in these systems by modulating either geometrical configuration or optical properties or via adiabatic control of their temperature. In Sec. III.C.6, we analyze various heat transport regimes in systems consisting of a large number of objects and show that RHT can be described as a generalized random walk with a non-Gaussian probability distribution function. For a situation unlike that of solid-state physics for heat conduction in bulk materials, we demonstrate the existence of anomalous heat transport regimes and highlight that these regimes closely depend on the system dimension, drastically changing from dilute to dense systems. The next few sections are devoted to nonreciprocal systems. Unlike reciprocal systems, in these non-Hermitian systems the classical notion of Lorentz reciprocity is violated, giving rise to specific heat-transfer mechanisms. After extending in Secs. III.D.2 and III.D.3 the theoretical framework to deal with heat exchange in such systems, we discuss in Sec. III.D.4 several thermomagnetic effects (magnetoresistance, permanent currents, and the Hall effect) that take place in magneto-optical systems, and we underline in Sec. III.D.5 the link between these effects and the topological structure of the Poynting field. We also stress in Sec. III.D.7 the potential of these systems to efficiently tune the direction of heat flow. We conclude this review by listing outstanding challenges and a broader outlook of potential future research directions.

II. TWO-BODY SYSTEMS

Most theoretical work on the topic of NFRHT is primarily based on Rytov's FE theory. Developed in the 1950s (Rytov, Kravtsov, and Tatarskii, 1989), FE is a semiclassical theory that assumes that thermal radiation is generated by random, thermally activated electric currents inside the bodies. Thus, the technical problem in the description of RHT between different objects boils down to the solution of the stochastic Maxwell's equations, with random electric currents as radiation sources. To illustrate the idea, we consider two optically isotropic and nonmagnetic bodies separated by a vacuum gap; see Fig. 2. In the framework of FE, the RHT problem is completely specified by the temperature distributions $T_i(\mathbf{r})$ $(i = 1, 2)$ and the dielectric functions of the materials $\epsilon_i(\mathbf{r}, \omega)$. The macroscopic Maxwell's equations to be solved adopt the following form in the frequency domain:

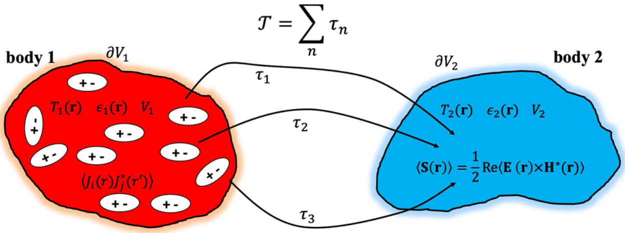

FIG. 2. Fluctuational electrodynamics. Schematic of radiative heat transfer in a two-body system. The two bodies of volumes V_1 and V_2 have temperature profiles $T_1(\mathbf{r})$ and $T_2(\mathbf{r})$ and frequency-dependent dielectric functions $\epsilon_1(\mathbf{r}, \omega)$ and $\epsilon_2(\mathbf{r}, \omega)$. Electromagnetic fields $\mathbf{E}$ and $\mathbf{H}$ are generated by the random currents $\mathbf{J}$ in the bodies due to their nonvanishing correlations given by the fluctuation-dissipation theorem. The net power exchanged by the two bodies is determined by the total transmission $\mathcal{T}$ that can be expressed as a sum of individual transmission coefficients τ_n.

$$\nabla \times \mathbf{E}(\mathbf{r}, \omega) = i\omega\mu_0 \mathbf{H}(\mathbf{r}, \omega), \tag{1}$$

$$\nabla \times \mathbf{H}(\mathbf{r}, \omega) = -i\omega\epsilon_0 \epsilon(\mathbf{r}, \omega)\mathbf{E}(\mathbf{r}, \omega) + \mathbf{J}(\mathbf{r}, \omega), \tag{2}$$

where $\mathbf{E}$ and $\mathbf{H}$ are the electric and magnetic fields, $\mathbf{r}$ is the position vector, and ϵ_0 and μ_0 are the vacuum permittivity and permeability, respectively. In Eq. (2), the fluctuating current density distributions $\mathbf{J}(\mathbf{r}, \omega)$ within the bodies are the sources of the thermal radiation. The statistical average of these currents vanishes, i.e., $\langle \mathbf{J} \rangle = 0$, but their correlations are finite and given by the fluctuation-dissipation theorem (Eckhardt, 1984; Rytov, Kravtsov, and Tatarskii, 1989; Joulain *et al.*, 2005)

$$\begin{aligned}\langle \mathbf{J}(\mathbf{r}, \omega) \otimes \mathbf{J}^*(\mathbf{r}', \omega) \rangle = {} & \frac{4\hbar\omega^2\epsilon_0}{\pi} \mathrm{Im}\{\epsilon(\mathbf{r}, \omega)\} \\ & \times n(\omega, T(\mathbf{r}))\delta(\mathbf{r} - \mathbf{r}'),\end{aligned} \tag{3}$$

where $\hbar$ is the Planck constant and $n(\omega, T) = 1/(\exp[\hbar\omega/k_B T] - 1)$ is the Bose function. In simple terms, the calculation of the radiative power exchanged by bodies 1 and 2 is done by first solving the Maxwell equations with the appropriate boundary conditions defined by geometries of the bodies and assuming that the random electric currents occupy the entire body 1. Then, with the solution for the fields around body 2, the statistical average of the Poynting vector is computed: $\langle \mathbf{S}(\mathbf{r}, \omega) \rangle = 2\mathrm{Re}\langle \mathbf{E}(\mathbf{r}, \omega) \times \mathbf{H}(\mathbf{r}, \omega) \rangle$. Finally, the results are integrated over frequency and over a closed surface enclosing body 2. To evaluate the net RHT, one needs to calculate in a similar way the heat transferred from body 2 to body 1.

This innocent-looking problem is, however, challenging in general, and analytical solutions are known in only a handful of situations. One of the main goals of the rest of this section is to present the solution in cases of increasing complexity focusing on two-body systems. As mentioned in the Introduction, the net power P_{net} exchanged via thermal radiation between two objects of homogeneous temperatures T_1 and T_2 can always be expressed via means of the Landauer formula, as one can easily understand with the following heuristic argument. The net radiative power is the balance between the heat power transferred from one body to the other $P_{\mathrm{net}} = P_{1\to 2} - P_{2\to 1}$, where the individual contributions are given by

$$\mathcal{P}_{i\to j} = \int_0^\infty \frac{d\omega}{2\pi} \hbar\omega n(\omega, T_i) \mathcal{T}_{ji}(\omega). \tag{4}$$

Here $\hbar\omega$ is the energy of an electromagnetic mode of frequency ω and the Bose function $n(\omega, T)$ is describing the thermal occupation of that mode and $\mathcal{T}_{ji}(\omega)$ is the total transmission coefficient that corresponds to the sum of the probabilities over all the modes of frequency ω that can be transferred from body i to body j. In the case of a two-body system with no environment, detailed balance imposes that $\mathcal{T}_{21}(\omega) = \mathcal{T}_{12}(\omega) = \mathcal{T}(\omega)$ and the expression of the net power reduces to the Landauer formula (Polder and van Hove, 1971; Ben-Abdallah and Joulain, 2010; Biehs and Greffet, 2010a)

$$\mathcal{P}_{\mathrm{net}} = \int_0^\infty \frac{d\omega}{2\pi} \hbar\omega[n(\omega, T_1) - n(\omega, T_2)]\mathcal{T}(\omega). \qquad (5)$$

Following the spirit of the Landauer approach in mesoscopic physics, the total transmission can be analyzed in terms of radiation channels and can be expressed as

$$\mathcal{T}(\omega) = \sum_n \tau_n(\omega), \qquad (6)$$

where the τ's are the individual transmission probabilities of the different open channels (bounded between 0 and 1). This point is particularly useful to establish simple upper bounds for RHT, as we discuss later in this review.

A. Parallel plates

As mentioned in the Introduction, the importance of the contribution of evanescent waves in the RHT between two objects and the possibility of overcoming the Planckian limit in the near-field regime was first put forward in around 1970 by Cravalho, Tien, Domoto, Caren, and Boehm (Cravalho, Tien, and Caren, 1967; Boehm and Tien, 1970; Domoto and Tien, 1970). Polder and van Hove (1971) were the first to use the rigorous framework of fluctuational electrodynamics to calculate the NFRHT rate between two infinite parallel plates, a geometry that has become the workhorse of NFRHT and that is schematically represented in Fig. 1. We refer to the upper plate as medium 1 and the lower plate as medium 2 and assume that they are at constant temperatures T_1 and T_2, respectively. In the case of optically isotropic and nonmagnetic materials, Polder and van Hove showed that the radiative power per unit area, i.e., the heat flux Φ, between the parallel plates is given by Eq. (5) with the following replacement of the transmission coefficient with a transmission coefficient per unit area:

$$\mathcal{T}(\omega) \to \int_0^\infty \frac{d\kappa}{2\pi} \kappa\tau(\omega, \kappa, d). \qquad (7)$$

Here $\kappa = \sqrt{k_x^2 + k_y^2}$ is the magnitude of the wave vector parallel to the plates [see coordinate system in Fig. 1(a)], d is the gap size, and $\tau(\omega, \kappa, d)$ is the total sum over polarizations transmission probability of an electromagnetic mode of frequency ω and parallel wave vector κ. In the case of isotropic materials, this total transmission is equal to $\tau(\omega, \kappa, d) = \tau_s(\omega, \kappa, d) + \tau_p(\omega, \kappa, d)$, where the contributions of s- and p-polarized waves (or, alternatively, TE and TM waves) are given by ($\alpha = s, p$)

$$\tau_\alpha(\omega, \kappa, d) = \begin{cases} \frac{(1-|r_1^\alpha|^2)(1-|r_2^\alpha|^2)}{|D^\alpha|^2}, & \kappa < k_0, \\ \frac{4\mathrm{Im}(r_1^\alpha)\mathrm{Im}(r_2^\alpha)e^{-2|q_{\mathrm{v}}|d}}{|D^\alpha|^2}, & \kappa > k_0, \end{cases} \qquad (8)$$

where $k_0 = \omega/c$ is the wave number in vacuum and $D^\alpha = 1 - r_1^\alpha r_2^\alpha e^{2iq_{\mathrm{v}}d}$, c is the speed of light, $q_{\mathrm{v}} = \sqrt{k_0^2 - \kappa^2}$ is the perpendicular component of the wave vector in the vacuum gap, and r_i^α are Fresnel (or amplitude reflection) coefficients given by

$$r_i^s = \frac{q_{\mathrm{v}} - q_i}{q_{\mathrm{v}} + q_i}, \qquad r_i^p = \frac{\epsilon_i q_{\mathrm{v}} - q_i}{\epsilon_i q_{\mathrm{v}} + q_i}. \qquad (9)$$

Here $\epsilon_i(\omega)$ is the dielectric function of medium $i = 1, 2$, assumed to depend only on frequency (local media), and $q_i = \sqrt{\epsilon_i k_0^2 - \kappa^2}$.

The key point of this result is that the integral in Eq. (7) is carried out over all possible values of κ, and therefore it includes the contribution of both propagating waves ($\kappa < k_0$) and evanescent waves ($\kappa > k_0$). The latter are not taken into account in Stefan-Boltzmann's law. The contribution of the evanescent waves decays exponentially with the gap size [see Eq. (8)], and it becomes negligible in the far-field regime ($d \gg \lambda_{\mathrm{Th}}$). However, in the near-field regime ($d < \lambda_{\mathrm{Th}}$) the contribution of evanescent waves, often referred to as photon tunneling, can become significant and, for sufficiently small gaps, it may completely dominate the heat transfer. The blackbody result is obtained from Eq. (7) by ignoring the evanescent waves and assuming perfect transmission for the propagating waves for all frequencies and wave vectors. In that case, the radiative power per unit area is given by Stefan-Boltzmann's law $\Phi_{\mathrm{BB}} = \sigma(T_1^4 - T_2^4)$, where $\sigma = 5.67 \times 10^{-8}\ \mathrm{W/(m^2\,K^4)}$.

B. Metals versus dielectrics

The parallel-plate configuration allows us to illustrate not only the impact of evanescent waves in the near-field regime but also the importance of the choice of materials. There are two main classes of materials when it comes to NFRHT, namely, metals (or related materials with free carriers like doped semiconductors) and dielectrics (especially polar dielectrics that exhibit polaritonic resonances like $\mathrm{SiO_2}$, SiN, and SiC). As an example of the results for these two types of materials, we show in Figs. 3(a) and 3(c) the gap dependence of the room-temperature heat-transfer coefficient, i.e., the radiative heat conductance per unit area, for two parallel plates made of Au and $\mathrm{SiO_2}$. In those panels we also show the individual contributions of propagating and evanescent waves for TE and TM polarizations. Notice that in both cases the Planckian limit (indicated with an horizontal line) is largely overcome for sufficiently small gaps. This is particularly noteworthy in the silica case, where for $d = 1$ nm the heat flux is almost 5 orders of magnitude larger than the blackbody limit. Notice also that there are clear differences between Au and $\mathrm{SiO_2}$. For Au, the NFRHT rate is dominated by TE evanescent waves, which originate from eddy currents inside the Au plates (Polder and van Hove, 1971; Chapuis, Volz *et al.*, 2008). This typically leads to a saturation of the heat-transfer coefficient for small gaps. On the contrary, in the silica case NFRHT is dominated by TM evanescent waves that can be shown to stem from surface phonon polaritons (SPhPs): quasiparticle excitations that arise from the strong coupling of electromagnetic fields with the optical phonon modes of polar dielectrics (Mulet *et al.*, 2002). These surface electromagnetic waves are hybrid or cavity modes that reside in both plates and have a penetration depth that is of the order of the gap size (Basu and Zhang, 2009), which implies that they are increasingly confined to the surfaces as the gap is reduced (Song *et al.*, 2015). The increase of the density of the states of theses modes (Ben-Abdallah and Joulain, 2010; Biehs and Greffet, 2010a) upon reducing the gap size is reflected in a characteristic $1/d^2$ dependence of the heat-transfer coefficient for polar dielectrics.

Apart from enhancing NFRHT, evanescent waves are also responsible for a drastic modification of the spectral heat flux (or heat conductance per unit frequency); see Figs. 3(b) and 3(d). Thus, in the SiO_2 case the spectral heat flux is dominated by two peaks that appear at the frequencies of the SPhP resonances of this polar dielectric. This is dramatically different than the broadband Planck's distribution and is also due to the fact that NFRHT in this case is dominated by SPhPs.

In principle, the previously discussed plate-plate configuration is ideally suited to experimentally investigating NFRHT because some of the largest enhancements in this regime are expected to occur in this setting. However, this configuration is difficult to realize in practice because it is very complicated to achieve and maintain good parallelism between macroscopic plates at nanometer separations. In recent years several groups have overcome this hurdle and developed novel techniques to explore the plate-plate configuration in the near-field regime, and they have been able to confirm the results of the FE theory. Some of those experiments have made use of macroscopic (approximately centimeter × centimeter) planar surfaces (Hu *et al.*, 2008; Ottens *et al.*, 2011; Bernardi, Milovich, and Francoeur, 2016; Ghashami *et al.*, 2018; DeSutter, Tang, and Francoeur, 2019), while others are based on microscopic plates ($50 \times 50\ \mu m^2$) (St-Gelais *et al.*, 2014, 2016; Song *et al.*, 2016; Fiorino, Thompson *et al.*, 2018). The use of macroscopic planar surfaces is conceptually simple, but in practice it is more difficult to ensure the parallelism and to have clean and smooth surfaces over such large areas. For this reason, the smallest gaps achieved with this strategy are still above 100 nm (DeSutter, Tang, and Francoeur, 2019). On the other hand, the use of microdevices facilitates the parallelization of the systems and the characterization of the surfaces. With this approach, it has become possible to explore gaps as small as 30 nm (Fiorino, Thompson *et al.*, 2018), as we illustrate in Fig. 4. In this example, a microdevice comprising a Pt resistor that heats up the emitter and measures its temperature was used to measure the NFRHT rate between two SiO_2 surfaces down to gaps of about 30 nm. For these small gaps, it was found that the heat conductance was about 1200 times larger than in the far-field regime and about 700 times larger than the blackbody limit, in agreement with the theory results based on FE. Recently it has even been claimed that distances below 10 nm are reachable (Salihoglu *et al.*, 2020).

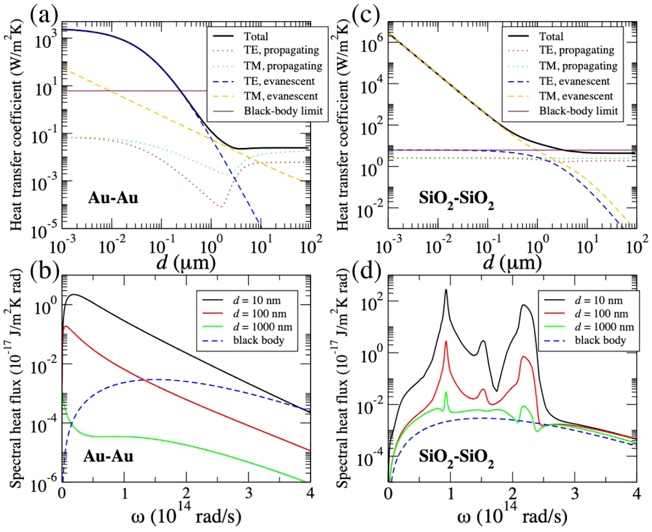

FIG. 3. (a) Heat-transfer coefficient at room temperature (300 K) as a function of the gap size for two infinite thick parallel plates made of Au. The different lines correspond to the total contribution (black solid line) and to the contributions of propagating and evanescent waves for TE and TM polarizations. The horizontal line shows the result for two black bodies: $6.124\ W/(m^2\,K)$. (b) The spectral heat flux (or conductance per unit area and frequency) as a function of the radiation frequency corresponding to the case in (a). The solid lines correspond to three different values of the gap size in the near-field regime, while the blue dashed line is the result for two black bodies. (c),(d) The same as in (a),(b) for SiO_2.

C. Nonreciprocal materials

A special class of materials that has attracted significant attention in the context of thermal radiation is that of nonreciprocal materials. These materials do not satisfy

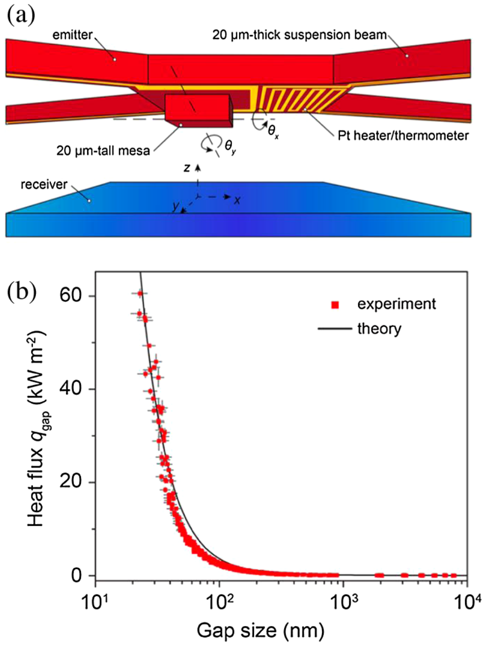

FIG. 4. (a) Schematic illustration of NFRHT measurement configuration used by Fiorino, Thompson *et al.* (2018). The emitter microdevice is composed of a square mesa and Pt heater or thermometer suspended on a thermally isolated island. The receiver is a macroscopically large ($1 \times 1\ cm^2$) plate. (b) The corresponding heat flux vs gap size in the case of an emitter and an receiver made of SiO_2. Measured data (red squares) are compared to the theoretical result (solid black line) obtained within FE. From Fiorino, Thompson *et al.*, 2018.

Lorentz reciprocity (Caloz *et al.*, 2018) and, in practice, are optically anisotropic materials with dielectric tensors that are nonsymmetric. A paradigmatic example is that of magneto-optical (MO) materials where the nonreciprocity is induced either by an internal magnetization as in ferromagnets or by an external magnetic field as in doped semiconductors. Part of the attention is due to the suggestion that these materials might violate Kirchhoff's law (Zhu and Fan, 2014), which establishes the equality of thermal emissivity and absorptivity. Although it has been shown that this is not the case in a two-body situation (one body could be an environment) (Ekeroth, García-Martín, and Cuevas, 2017), this class of materials does give rise to countless novel thermal-radiation phenomena in the context of many-body systems, as discussed later in this review.

In the context of NFRHT in two-body nonreciprocal systems, most of the work thus far has focused on the analysis of MO materials and, in particular, on the study of the use of an external magnetic field as a way to actively control thermal radiation. Special attention has been devoted to doped semiconductors, which in the presence of an external magnetic field exhibit strong MO activity in the infrared. The first theoretical study of this kind was reported by Moncada-Villa *et al.* (2015), who analyzed the magnetic-field dependence of the heat-transfer coefficient of two parallel plates made of doped semiconductors (InSb or Si). These materials become optically anisotropic and nonreciprocal in the presence of an external magnetic field. Thus, the problem is computing the RHT between two anisotropic parallel plates. This generic problem was addressed by Bimonte (2009) and Biehs *et al.* (2011) and, as in the isotropic case discussed in Sec. II.A, the net power per unit area or heat flux Φ is given by the Landauer formula of Eq. (5) with the substitution

$$\mathcal{T}(\omega) \to \int \frac{d\boldsymbol{\kappa}}{(2\pi)^2}\,\tau(\omega,\boldsymbol{\kappa},d). \tag{10}$$

Here $\boldsymbol{\kappa} = (k_x, k_y)^t$ (and therefore $d\boldsymbol{\kappa} = dk_x dk_y$) is the wave vector parallel to the surface planes and $\tau(\omega,\boldsymbol{\kappa},d)$ is the transmission probability of the individual electromagnetic waves. Notice that the integral in Eq. (10) is now carried out over all possible directions of $\boldsymbol{\kappa}$ [τ is no longer isotropic in $\boldsymbol{\kappa}$ space (Fan *et al.*, 2020)] and, as usual, it includes the contribution of both propagating and evanescent waves. The transmission coefficient $\tau(\omega,\boldsymbol{\kappa},d)$ can be expressed as

$$\tau(\omega,\boldsymbol{\kappa},d) = \begin{cases} \mathrm{Tr}\{[\mathbb{1} - \mathbb{R}_1\mathbb{R}_1^\dagger]\mathbb{D}^\dagger[\mathbb{1} - \mathbb{R}_2^\dagger\mathbb{R}_2]\mathbb{D}\}, & \kappa < k_0, \\ \mathrm{Tr}\{[\mathbb{R}_1 - \mathbb{R}_1^\dagger]\mathbb{D}^\dagger[\mathbb{R}_2^\dagger - \mathbb{R}_2]\mathbb{D}\}e^{-2|q_\mathrm{v}|d}, & \kappa > k_0, \end{cases} \tag{11}$$

where the 2×2 matrices $\mathbb{R}_i$ (with $i = 1, 2$) are the reflection matrices characterizing the two interfaces. These matrices have the following generic structure:

$$\mathbb{R}_i = \begin{pmatrix} r_i^{ss} & r_i^{sp} \\ r_i^{ps} & r_i^{pp} \end{pmatrix}, \tag{12}$$

where $r_i^{\alpha\beta}$, with $\alpha, \beta = s, p$, is the reflection amplitude for the scattering of an incoming α-polarized plane wave into an outgoing β-polarized wave. In particular, the off-diagonal elements describe the polarization conversion, which does not occur for isotropic materials. Finally, the 2×2 matrix $\mathbb{D}$ in Eq. (11) is defined as

$$\mathbb{D} = [\mathbb{1} - \mathbb{R}_1\mathbb{R}_2 e^{2iq_\mathrm{v}d}]^{-1}. \tag{13}$$

The different reflection matrices appearing in Eq. (12) can be computed within standard approaches for anisotropic multilayer systems.

This formalism was used by Moncada-Villa *et al.* (2015) to show that the NFRHT rate between two parallel plates made of doped InSb and Si can be strongly affected by the application of a static magnetic field, and relative changes

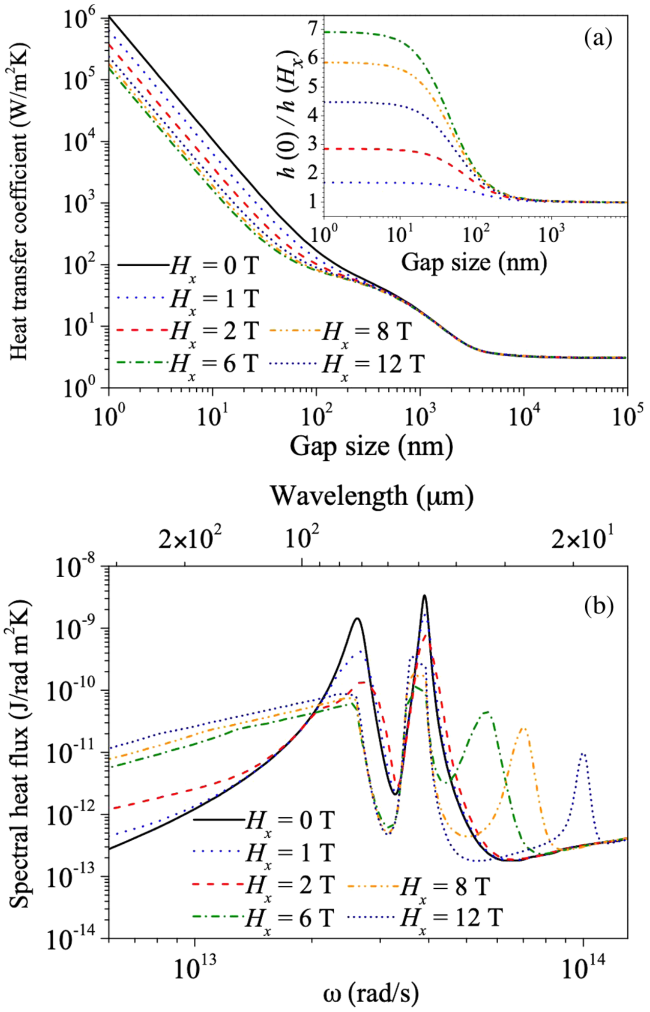

FIG. 5. (a) Heat-transfer coefficient for two parallel plates made of n-doped InSb at room temperature (300 K) as a function of the gap size for different values of a magnetic field applied parallel to the surfaces of the plates (x direction). Inset: ratio between the zero-field coefficient and the coefficient for different values of the field in the near-field region. (b) The corresponding spectral heat flux as a function of the frequency (and wavelength) for a gap of $d = 10$ nm and different values of the parallel field. From Moncada-Villa *et al.*, 2015.

of up to 700% were predicted for fields of a few teslas. These results are illustrated in Fig. 5 for the case of a magnetic field oriented parallel to the plates. More recently Moncada-Villa and Cuevas (2020) also showed that NFRHT between two parallel plates made of MO materials can be modulated by simply changing the orientation of the external magnetic field, which is the thermal analog of well-known phenomenon of anisotropic thermal magnetoresistance in the field of spintronics. This and other thermomagnetic phenomena in the context of small MO particles are discussed in more detail in Sec. III.D.

D. Nanostructuring, roughness, and materials

Following ideas and concepts of nanophotonics, many groups have explored nanostructuring as a strategy to further enhance NFRHT and to tune its spectral properties. Here we review some of the ideas put forward in recent years in the context of NFRHT in nanostructured planar systems and also discuss the impact of deviations from planarity.

1. Multilayer structures and photonic crystals

A natural extension of the previously discussed plate-plate configuration is to replace the plates by planar multilayer structures or 1D photonic crystals (Biehs, 2007; Biehs, Reddig, and Holthaus, 2007; Francoeur, Mengüç, and Vaillon, 2008, 2010a, 2011; Ben-Abdallah *et al.*, 2009a, 2009b; Ben-Abdallah, Joulain, and Pryamikov, 2010; Basu and Francoeur, 2011; Maslovski, Simovski, and Tretyakov, 2013; Miller, Johnson, and Rodriguez, 2014; Jin, Messina, and Rodriguez, 2017a; Iizuka and Fan, 2018). A central idea in this case is to incorporate thin films in layered systems to make better use of surface electromagnetic modes. In practice, the RHT rate between two planar multilayer bodies comprising an arbitrary number of layers can be formally described with the same formulas as in the plate-plate case [see Eqs. (7) and (8)], but in this case r_1^α and r_2^α have to be interpreted as the reflection coefficients of the two subsystems (including their complete layered structures); see Bimonte (2009) and Ben-Abdallah, Joulain, and Pryamikov (2010). To give a concrete example, we follow Song *et al.* (2015) and consider the multilayer structure shown in the inset of Fig. 6, where the first body is an infinite SiO$_2$ plate (medium 1) and the second body features a SiO$_2$ film of thickness t (medium 3) deposited on a semi-infinite layer of Au (medium 4), while medium 2 is the vacuum gap of size d. In this case, r_2^α in Eq. (8) has to be replaced by (Biehs, 2007)

$$R^\alpha = \frac{r_{23}^\alpha + r_{34}^\alpha e^{2iq_3t}}{1 - r_{34}^\alpha r_{32}^\alpha e^{2iq_3t}}, \tag{14}$$

which is the reflection coefficient of the subsystem formed by media 3 and 4. Here, as usual, r_{ij}^α are the Fresnel coefficients of the different interfaces:

$$r_{ij}^s = \frac{q_i - q_j}{q_i + q_j}, \qquad r_{ij}^p = \frac{\epsilon_j q_i - \epsilon_i q_j}{\epsilon_j q_i + \epsilon_i q_j}, \tag{15}$$

where $q_i = \sqrt{\epsilon_i k_0^2 - \kappa^2}$. Finally, the Fabry-Perot denominator in Eq. (8) now adopts the form $D^\alpha = 1 - r_{21}^\alpha R^\alpha e^{2iq_2 d}$.

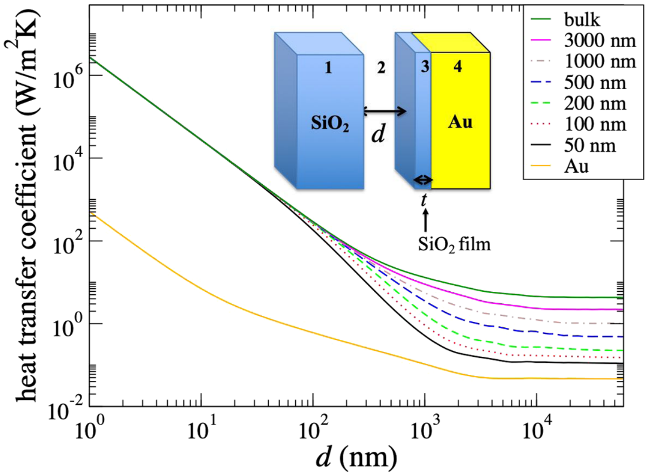

FIG. 6. Computed heat-transfer coefficient as a function of gap size for the multilayer system shown in the inset at room temperature (300 K). This structure comprises a thick, semi-infinite silica surface separated by a vacuum gap of size d from a silica thin film coating on a semi-infinite Au surface. Different curves correspond to different thicknesses of the silica coating. Adapted from Song *et al.*, 2015.

In Fig. 6 we show representative results of the gap dependence of the heat-transfer coefficient of this multilayer structure for different values of the thickness of the silica film, ranging from 50 nm to bulk. We also show the result with no SiO$_2$ film for comparison. Notice that for small gaps ($d < 100$ nm) the results are independent of the silica film thickness, which shows that the extraordinary NFRHT enhancements that occur in the bulk systems made of polar dielectrics are also possible in thin-film structures as long as the gap size is smaller than the film thickness (Biehs, 2007; Biehs, Reddig, and Holthaus, 2007). As previously explained, the physical origin of these results can be traced back to the fact that NFRHT is dominated by electromagnetic cavity modes arising from SPhPs whose penetration depth scales with the gap size. Thus, when the gap is sufficiently small, all the heat transfer comes from a shallow region on the surface of the two bodies and NFRHT becomes independent of the film thickness. These qualitative predictions were subsequently experimentally confirmed by Song *et al.* (2015) using a 53-μm-diameter silica sphere as an emitter, instead of the silica plate used in the calculations of Fig. 6. The finite curvature of the sphere results in smaller NFRHT enhancements relative to the planar structure, as is easily understood with the standard proximity approximation; see Song *et al.* (2015) for details. The validity of this approximation for the description of NFRHT has been amply discussed in the literature; see Otey and Fan (2011) and references therein.

To increase NFRHT beyond bulk systems, different groups have proposed combining several thin films to make use of the hybridization of the surface modes in different interfaces (Biehs, 2007; Francoeur, Mengüç, and Vaillon, 2008, 2011; Ben-Abdallah *et al.*, 2009a; Jin, Messina, and Rodriguez, 2017a; Iizuka and Fan, 2018). Another proposed strategy to outperform bulk systems relies on the use of 1D photonic crystals (Ben-Abdallah, Joulain, and Pryamikov, 2010; Tschikin, Ben-Abdallah, and Biehs, 2012). In this case the heat-transfer mechanism involves the surface Bloch state coupling supported by these media.

2. Metamaterials

Another topic that has been extensively studied in the context of NFRHT between nanostructured systems is the use of metamaterials, i.e., artificial structures with subwavelength features designed to exhibit complex optical properties that are difficult to find in naturally occurring bulk materials. In particular, special attention has been devoted to hyperbolic metamaterials, which are a special class of highly anisotropic media whose electromagnetic modes have a hyperbolic dispersion relation. To be precise, they are uniaxial materials for which one of the principal components of either the permittivity or the permeability tensor is opposite in sign to the other two principal components. These systems have been primarily fabricated based on designs involving hybrid metal-dielectric superlattices and metallic nanowires embedded in dielectric hosts (Poddubny *et al.*, 2013). The interest in these metamaterials in the context of NFRHT lies in the fact that they have been predicted to behave as broadband super-Planckian thermal emitters (Nefedov and Simovski, 2011; Biehs, Tschikin, and Ben-Abdallah, 2012; Guo *et al.*, 2012). This behavior originates from the fact that these metamaterials can support large wave vector frustrated modes that are evanescent in a vacuum gap, but that are propagating inside the material. This leads to broadband enhancement of the transmission efficiency of the evanescent modes (Biehs, Tschikin, and Ben-Abdallah, 2012). From the computational point of view, the heat transfer between hyperbolic metamaterials can be described using either the scattering approach for multilayer media described in Sec. II.D.1 or the more general method discussed in Sec. II.D.3 and applicable to laterally periodic patterned structures. In the latter case, and for appropriate subwavelength periodicities, it is typical to expoit an effective medium theory in order to reduce the problem to one involving planar but optically anisotropic materials, allowing application of the approach described in Sec. II.C.

The special properties of hyperbolic metamaterials have spurred many theoretical investigations of their use in the context of NFRHT (Biehs *et al.*, 2013; Guo and Jacob, 2013, 2014; Liu, Zhang, and Zhang, 2013, 2014b; Tschikin *et al.*, 2013; Lang *et al.*, 2014; Miller, Johnson, and Rodriguez, 2014). These works have in turn demonstrated that metamaterials do not outperform thin-film-based structures exhibiting SPhPs, as their increased density of states is compensated for by a decrease in the strength of the evanescent fields (Miller, Johnson, and Rodriguez, 2014). Nevertheless, metamaterials exhibit other interesting properties: for instance, the long penetration depth of the hyperbolic modes can be advantageous for applications in near-field thermophotovoltaics (Simovski *et al.*, 2013).

3. Gratings and metasurfaces

Also inspired by nanophotonic concepts, NFRHT between periodically patterned systems has been intensively investigated from a theoretical point of view, both in one dimension (gratings) and in two dimensions (photonic crystals and periodic metasurfaces). Again, the goal of such nanostructuring is to tune the spectral heat transfer and enhance net NFRHT. Technically speaking, the previously discussed Landauer formula can be straightforwardly generalized to deal with periodic systems by making use of Bloch's theorem. This was first done by Bimonte; see Bimonte (2009) for technical details. Using that generalized formula in combination with different techniques for the computation of reflection coefficients in periodic systems, typically via the rigorous coupled wave analysis method, several groups have reported calculations of NFRHT between periodic metallic nanostructures in both one dimension (Guérout *et al.*, 2012; Dai, Dyakov, and Yan, 2015; Dai *et al.*, 2016; Messina, Noto *et al.*, 2017) and two dimensions (Dai, Dyakov, and Yan, 2016; Jin *et al.*, 2019). The key idea in this case is to use nanostructuring to create new surface modes, referred to as spoof plasmons (Pendry, Martin-Moreno, and Garcia-Vidal, 2004), whose frequencies can be adjusted by tuning the length scales of these periodic systems so that their surface modes can be thermally populated at the desired working temperature. The reported results have demonstrated the possibility of enhancing NFRHT over the corresponding planar bulk materials. However, NFRHT in these periodically patterned metallic structures continues to be smaller than that observed in simple (unstructured) planar polar dielectrics, with few exceptions (Jin *et al.*, 2019).

There has also been significant theoretical work on the topic of NFRHT between dielectric photonic crystals and metasurfaces (Rodriguez *et al.*, 2011; Liu, Zhao, and Zhang, 2015; Liu and Zhang, 2015a). Again, these structured systems exhibit enhanced NFRHT with respect to their bulk counterparts, but the resulting NFRHT rates are again much smaller than those of planar polar dielectrics. In this regard, it has been predicted that metasurfaces can indeed provide a way to enhance NFRHT between extended structures (Fernández-Hurtado *et al.*, 2017). To be precise, it has been shown that Si-based metasurfaces featuring two-dimensional periodic arrays of holes (see Fig. 7) can exhibit a room-temperature near-field radiative heat conductance larger than that of any unstructured material to date. This enhancement relies on the possibility of largely tuning the spectral properties of the surface plasmon polaritons that dominate NFRHT in these structures. In particular, nanostructuring enables the appearance of broadband and lower-frequency surface modes, increasing their contribution and occupation at room temperature, which constitutes one of the main strategies being pursued to enhance NFRHT. We conclude here by noting that, to our knowledge, no experiment thus far has probed NFRHT between patterned structures.

4. Graphene

Two-dimensional materials are revolutionizing material science and they also hold promise in the field of NFRHT. In particular, graphene has attracted much attention, as it can support delocalized surface plasmon polaritons (SPPs) that can contribute to NFRHT in spite of graphene's ultrasmall (one-atom) thickness (Volokitin and Persson, 2011; Ilic *et al.*,

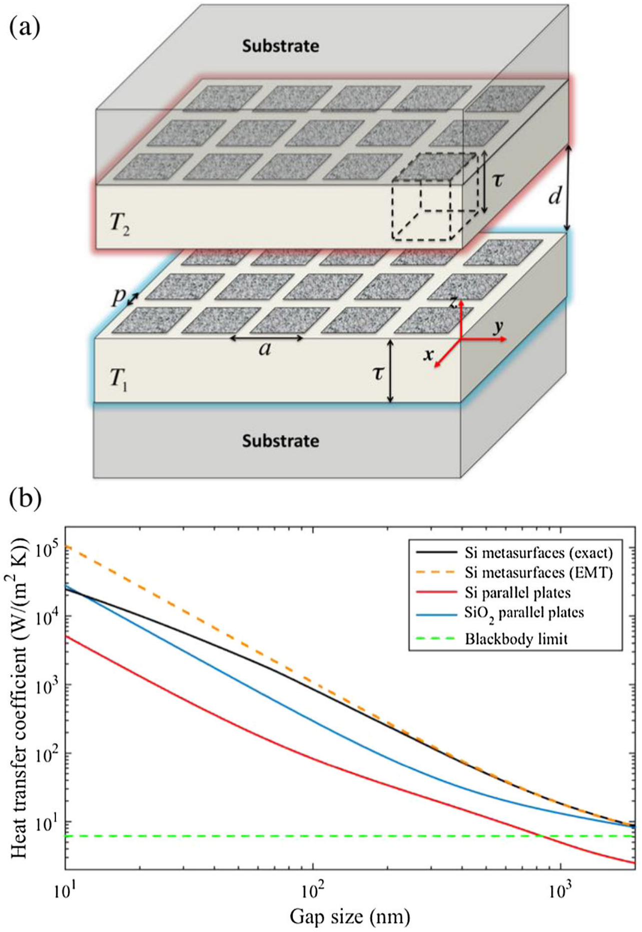

FIG. 7. (a) Schematic of two doped-Si metasurfaces made of 2D periodic arrays of square holes placed on semi-infinite planar substrates and held at temperatures T_1 and T_2. (b) Room-temperature heat-transfer coefficient as a function of the gap size for the doped-Si metasurfaces of (a) with $a = 50$ nm and a filling factor of 0.9 (black line). For comparison, the plot also includes the results for the Si metasurfaces computed with an effective medium theory (orange dashed line), SiO$_2$ parallel plates (blue line), and doped-Si parallel plates (red line). The horizontal dashed line shows the blackbody limit. From Fernández-Hurtado *et al.*, 2017.

2012a). What makes these surface modes so attractive compared to SPhPs in polar dielectrics is the possibility of modulating them electronically (Messina, Hugonin *et al.*, 2013), which can be achieved by controlling graphene's chemical potential by means of a nearby gate electrode. Such a mechanism provides an ideal strategy to actively control NFRHT in graphene-based structures (Papadakis *et al.*, 2019). On the other hand, several theoretical studies have shown that coating structures with graphene sheets may lead to a substantial increase in NFRHT (Svetovoy, van Zwol, and Chevrier, 2012; Lim, Lee, and Lee, 2013; Messina, Ben-Abdallah *et al.*, 2017). In this case, the idea is that appropriate engineering of the coupling of graphene's SPPs with other surface modes, like SPPs in doped Si or SPhPs in polar dielectrics, may increase the efficiency of heat exchange in the near-field regime. Another topic of great interest that has been theoretically investigated is the use of graphene-based structures in thermophotovoltaics (Ilic *et al.*, 2012b; Messina and Ben-Abdallah, 2013; Svetovoy and Palasantzas, 2014). Furthermore, the role of graphene in NFRHT has been theoretically studied in a wide variety of hybrid structures (Liu, Zhang, and Zhang, 2014b; Liu and Zhang, 2015b; Shi, Bao, and He, 2017; Zhao, Guizal *et al.*, 2017; Shi *et al.*, 2018; Shi, Bao *et al.*, 2019).

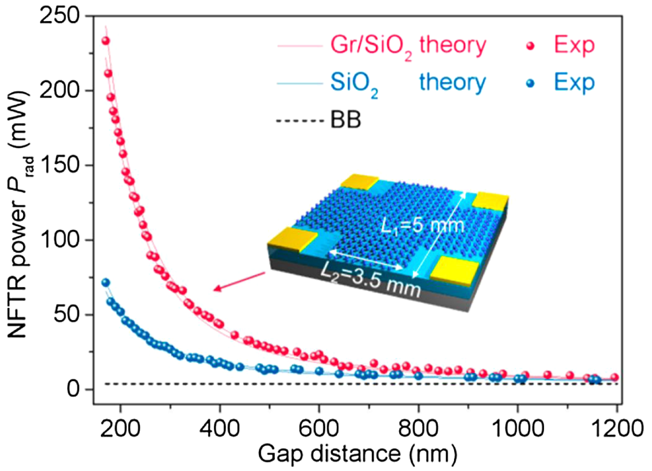

FIG. 8. Comparison of the NFRHT rate between graphene (Gr)/SiO$_2$ pair (red solid line) and SiO$_2$ pair (blue solid line) with various gap sizes. The temperatures of the emitter and the receiver are 323.2 and 301.5 K, respectively. Lines show the calculated values and spheres are the average values of four repeated measurements at each point. Inset: schematic illustration of the Gr/SiO$_2$ heterostructure. The blackbody limit has been plotted for comparison (black dashed line). From Shi, Sun *et al.*, 2019.

From an experimental perspective, recent works have confirmed that graphene enables enhanced NFRHT between polar dielectrics (van Zwol *et al.*, 2012; Shi, Sun *et al.*, 2019) and between Si substrates (both insulating and conductive) (Yang *et al.*, 2018). In particular, Shi, Sun *et al.* (2019) measured the NFRHT flux between two identical graphene-coated SiO$_2$ heterostructures with millimeter-scale surface area and reported a 64-fold enhancement relative to the corresponding blackbody limit for a gap size of 170 nm; see Fig. 8. Moreover, Shi, Sun *et al.* (2019) showed theoretically that the physical mechanism behind this large NFRHT enhancement is indeed the coupling between graphene's SPPs and silica's SPhPs. The first experimental demonstration of NFRHT modulation by electronic gating of a graphene field-effect heterostructure was only recently reported (Thomas *et al.*, 2019).

5. Surface roughness

Most calculations of NFRHT in planar structures assume that the corresponding surfaces are perfectly flat. Such an idealization ignores practical considerations such as surface roughness. The impact of surface roughness on NFRHT was addressed theoretically by Biehs and Greffet (2010b) in a plate-plate configuration. Using a form of perturbation theory, they showed that, assuming reasonable values for the height of the roughness profile (∼5 nm), corrections to the heat-transfer coefficient due to roughness can lead to roughly the same order of magnitude difference compared to perfectly flat surfaces when the gap size is of the order of a few tens of nanometers, for both metals and polar dielectrics. Moreover, they showed that proximity approximations previously used for describing rough surfaces are highly inaccurate when gap sizes become much larger than the correlation length of the surface roughness, even when the heat transfer is dominated by the coupling of surface modes. We also note that the influence of surface roughness has also been studied by way of the finite-difference time-domain method in combination with the Wiener chaos expansion approach (Chen and Xuan, 2015), along with its interplay with surface curvature (Krüger *et al.*, 2013).

E. Impact of geometry

Thus far, we have discussed NFRHT mainly in planar geometries in which the translational symmetry greatly simplifies the resolution of Maxwell's equations. In what follows, we turn to the analysis of the impact of geometry (heat exchange between structured bodies) and discuss how the aforementioned RHT formulas can be generalized to handle objects of arbitrary size and shape.

The Polder–van Hove formula expressing $\mathcal{T}(\omega)$ in terms of Fresnel reflection coefficients or generalized reflection matrices is well suited for calculations of heat transfer in systems with translational symmetry, including the aforementioned uniform planar slabs, thin films, gratings, photonic crystals, and periodic metamaterials. However, this leaves out a large class of systems of experimental and theoretical interest that do not exhibit such translational symmetries, particularly compact bodies like spheres or structured nanoparticles whose finite dimensions are relevant to the analysis of radiative heat transfer. Typically, in such cases it is incumbent to exploit general-purpose techniques to compute field response quantities entering $\mathcal{T}(\omega)$, for the geometry in question, in terms of the system's Green's function. One such powerful general scattering formalism was developed by Krüger *et al.* (2012) and Bimonte *et al.* (2017), arriving at the general formula (for reciprocal media)

$$\mathcal{T}(\omega) = 4\mathrm{Tr}[\mathbb{R}_2^*\mathbb{W}_{1,2}\mathbb{R}_1\mathbb{W}_{2,1}^*] \tag{16}$$

in terms of the radiation operator $\mathbb{R}_p = \mathbb{G}_0[\mathrm{Im}(\mathbb{T}_p) - \mathbb{T}_p\mathrm{Im}(\mathbb{G}_0)\mathbb{T}_p^*]\mathbb{G}_0^*$ and scattering operator $\mathbb{W}_{pq} = \mathbb{G}_0^{-1}(\mathbb{1} - \mathbb{G}_0\mathbb{T}_p\mathbb{G}_0\mathbb{T}_q)^{-1}$ for bodies $p, q \in \{1, 2\}$ defined in terms of the scattering T operators $\mathbb{T}_p$, which depend on the material properties and shape of the bodies and the Green's function operator $\mathbb{G}_0$ in vacuum. The strength of this formulation lies in its broad applicability, as it generalizes beyond systems with discrete or continuous translational symmetry: it can in principle be used for arbitrary geometries, including compact bodies whose finite sizes in each dimension are relevant, with faster numerical convergence for appropriate choices of basis functions. Additionally, while this T-operator formalism casts thermal radiation in terms of volumetric scattering quantities, related contemporaneous surface-integral equation formulations (Rodriguez, Reid, and Johnson, 2013) can similarly recover known semianalytical results for uniform planar media and be computationally amenable to general compact or extended geometries by casting thermal radiation purely in terms of surface unknowns, vastly reducing the computational complexity of calculations.

Furthermore, beyond simply aiding in generalizations of computations beyond extended media with translational symmetry, the T-operator formalism can shed further light on the number of contributing transmission channels to $\mathcal{T}(\omega)$. In the operators of Eq. (16), an operator of particular interest (Miller, 2000, 2007; Miller, Johnson, and Rodriguez, 2015; Molesky *et al.*, 2020; Venkataram *et al.*, 2020) is the off-diagonal block $\mathbb{G}_{0(2,1)}$ of the Green's function connecting points $\mathbf{r}'$ restricted to the volume of body 1 and $\mathbf{r}$ restricted to the volume of body 2. At first glance, the ability of electromagnetic fields to propagate through vacuum, or equivalently the coupling of all pairs of volumetric degrees of freedom in each of the different bodies, suggests that the number of channels will scale like the volume of each body. However, the electromagnetic surface equivalence theorem (Harrington, 1989; Rengarajan and Rahmat-Samii, 2000; Reid, White, and Johnson, 2013; Rodriguez, Reid, and Johnson, 2013; Otey *et al.*, 2014; Reid and Johnson, 2015) shows that the electromagnetic fields radiated by any volumetric polarization distribution to the exterior of some fictitious bounding surface can be exactly reproduced in that exterior region by an equivalent surface current distribution, therefore suggesting that the rank of $\mathbb{G}_{0(2,1)}$ actually scales with the *surface area* of each body; as shown by Polimeridis, Reid, Jin *et al.* (2015), it is indeed the effective rank of this off-diagonal scattering operator that determines the number of contributing transmission channels τ_n.

Based on the scattering approach and the standard Green's function formalism, there have been many studies of the heat flux between a sphere and a plane, as shown in Fig. 9, and between two spheres (Narayanaswamy, Shen, and Chen, 2008; Krüger, Emig, and Kardar, 2011; Otey and Fan, 2011; Sasihithlu and Narayanaswamy, 2011). Reviews highlighting other studies of NFRHT in nonplanar geometries were given by Otey *et al.* (2014) and Bimonte *et al.* (2017). Early studies of heat transfer between compact bodies typically focused on high-symmetry objects with simple shape. However, there have been far fewer studies of NFRHT in nanostructured compact bodies than of extended media (including the previously discussed gratings, photonic crystals, and metasurfaces) because the former, unlike the latter, does not easily succumb to semianalytical expressions for arbitrary geometries in the absence of symmetries like continuous or discrete translational invariance. Because of that, we discuss in Sec. II.F the development of various numerical methods to compute radiative heat transfer in a broad array of systems.

F. Numerical methods

Advances in computational hardware and numerical algorithms have led to an explosion of computational methods to study radiative heat transfer. The facts that the Landauer form of the radiative heat-transfer power depends only on the Bose function $n(\omega, T)$ and the Landauer energy transmission

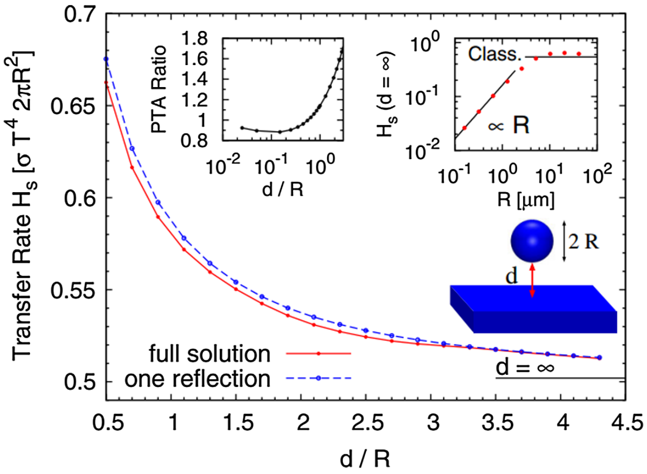

FIG. 9. Transferred power H_s by NFRHT between a SiO_2 sphere with radius $R = 5\ \mu m$ at 300 K and a SiO_2 plane at 0 K as a function of distance d. The transferred power is normalized to the power emitted by a blackbody with a surface area given by the cross section of the sphere. From Krüger, Emig, and Kardar, 2011.

spectrum $\mathcal{T}(\omega)$, and that the latter in Eq. (16) depends only on classical electromagnetic scattering quantities, means that standard computational techniques may be readily applied to studying radiative heat transfer. These methods, illustrated schematically with examples in Fig. 10, essentially fall into one of two categories, depending on the choice of either a spectral or a localized basis expansion (Reid, Rodriguez, and Johnson, 2013; Otey *et al.*, 2014; Song, Fiorino *et al.*, 2015; Bimonte *et al.*, 2017; Cuevas and García-Vidal, 2018), each of which brings a set of benefits and drawbacks.

1. Spectral methods

Techniques based on spectral expansions (Krüger *et al.*, 2012; Bimonte *et al.*, 2017) express the T operators of each individual body in terms of delocalized spectral functions (such as spherical vector waves). These basis functions include but are not limited to plane waves (Fourier basis) (Bimonte, 2009; Messina and Antezza, 2011b; Messina and Ben-Abdallah, 2013; Messina, Jin, and Rodriguez, 2016; Jin, Messina, and Rodriguez, 2017a), Bloch waves (Narayanaswamy and Chen, 2005; Francoeur, Mengüç, and Vaillon, 2009; Ben-Abdallah, Joulain, and Pryamikov, 2010; Tschikin, Ben-Abdallah, and Biehs, 2012; Messina, Noto *et al.*, 2017), and spherical or cylindrical harmonics (Narayanaswamy, Shen, and Chen, 2008; Krüger, Emig, and Kardar, 2011; Otey and Fan, 2011; McCauley *et al.*, 2012). The use of these basis functions is most convenient when the geometries involved exhibit discrete or continuous symmetries, like translation or rotation, as that can make the resulting matrix expressions for the relevant operators nearly diagonal, making computations far more efficient. However, in the absence of such symmetries, or when different bodies have shapes of different symmetries, not only are the resulting matrices dense, but also the convergence with respect to increasing numbers of basis functions slows dramatically. Furthermore, we note that with few exceptions, such as work on graphene sheets (Wunsch *et al.*, 2006; Neto *et al.*, 2009; Ilic *et al.*, 2012a; Sernelius, 2012), most applications of these spectral techniques have in practice focused on simple local isotropic homogeneous susceptibilities $\chi(\omega)$.

2. Decomposition methods

By contrast, techniques based on localized expansions (Otey *et al.*, 2014; Song, Fiorino *et al.*, 2015; Cuevas and García-Vidal, 2018) express either T operators or Maxwell Green's functions in terms of localized basis functions. One such technique is the finite-difference frequency domain method (Wen, 2010; Jin *et al.*, 2019), in which Maxwell's equations in the frequency domain are discretized on a lattice of grid points. In the context of RHT, fields in response to individual dipolar sources embedded in the radiating objects can be computed independently and then summed according to weights determined by the fluctuation-dissipation theorem; alternatively, the uncorrelated nature of dipolar sources at different spatial positions means that all such fluctuating sources can be simultaneously introduced and modeled as stochastic, random sources with correlation functions given by the fluctuation-dissipation theorem (requiring ensemble averages over many source realizations to reduce noise, as in Monte Carlo integration). The latter interpretation lends itself to a direct Langevin or stochastic time-domain simulation of Maxwell's equations (Rodriguez *et al.*, 2011). This last class of time-domain method has the added benefit that discretized spatial differential operators are represented as sparse matrices and allows representations of select classes of nonlocal (spatially dispersive) susceptibility models (particularly those arising in metals) in terms of spatial differential operators, such as the hydrodynamic model (Klimchitskaya and Mostepanenko, 2015; Xiao *et al.*, 2016), all the while being applicable to arbitrary body shapes. On the other hand, multiscale or large problems become particularly challenging to simulate, as the propagation of electromagnetic fields through vacuum means that the entire space between bodies must also be discretized, even if the separation is much larger than relevant body feature sizes, so the resulting convergence with respect to resolution can be prohibitively slow.

A related class of technique is the so-called volume-integral formulation of Maxwell's equations (Polimeridis, Reid, Jin *et al.*, 2015; Jin, Polimeridis, and Rodriguez, 2016; Jin, Messina, and Rodriguez, 2017b), of which the discrete dipole approximation (DDA) (Edalatpour and Francoeur, 2014, 2016; Edalatpour, DeSutter, and Francoeur, 2016; Ekeroth, García-Martín, and Cuevas, 2017) may be thought of as a special case. In general, volume-integral formulations use various classes of localized basis functions as basis expansions for T operators and $\mathbb{G}_0$. Unlike finite-difference methods, these techniques have the advantage of requiring basis functions only within the volumes of material bodies, with the full scattering problem represented by expressing the full Green's function in terms of the individual materials' scattering matrices and the analytically known free-space Green's function of the corresponding intervening medium. As expected, however, different choices of basis function offer challenges and trade-offs with respect to numerical convergence. As further elucidated later, DDA is effectively a

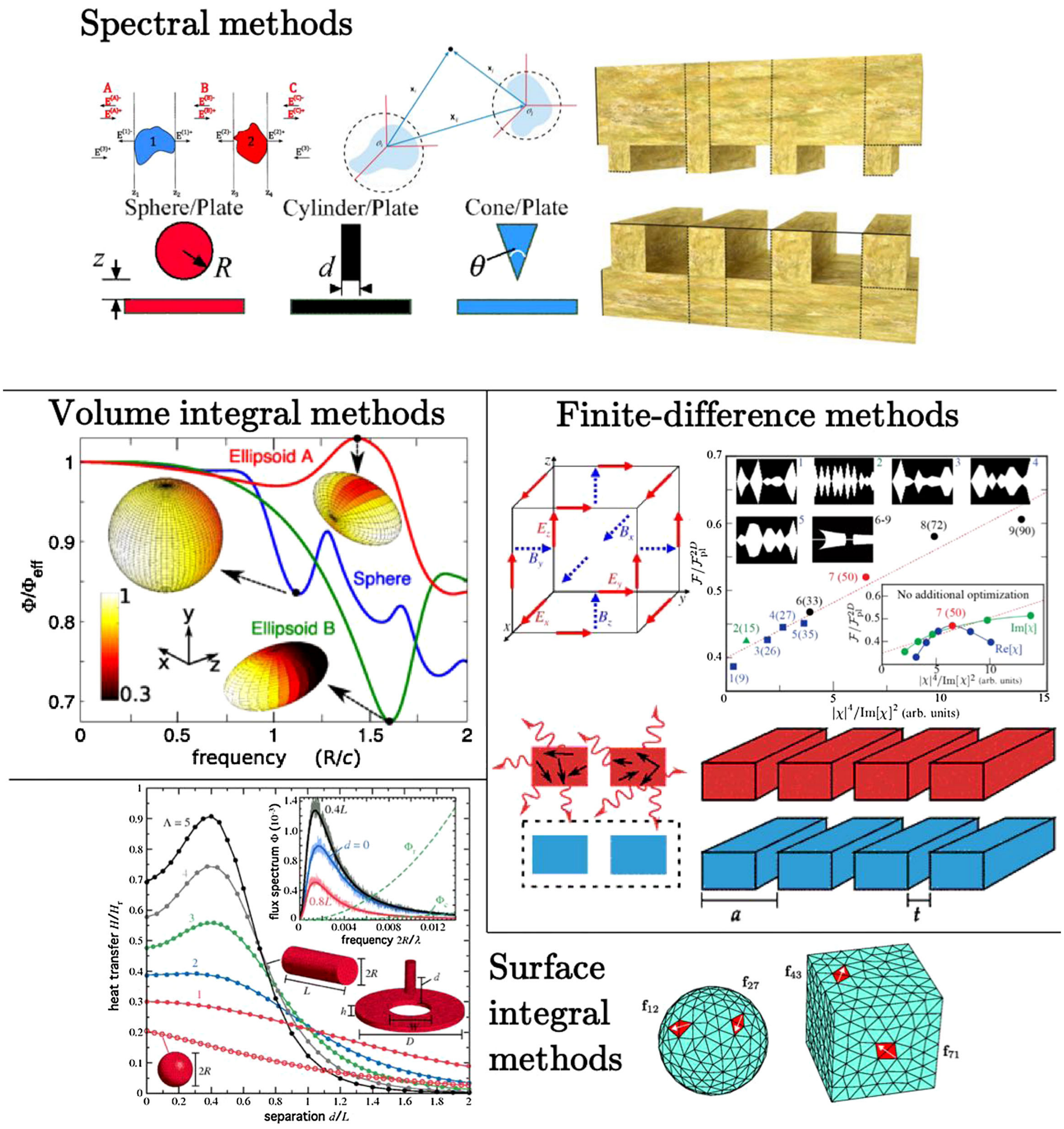

FIG. 10. Collage of selected computational methods. Schematics of basis functions, along with selected results, for spectral (Messina and Antezza, 2011b; McCauley *et al.*, 2012; Bimonte *et al.*, 2017; Messina, Noto *et al.*, 2017), finite-difference (Rodriguez *et al.*, 2011; Werner, Bauer, and Cary, 2013; Jin *et al.*, 2019), volume-integral (Polimeridis, Reid, Jin *et al.*, 2015), and surface-integral (Reid, White, and Johnson, 2013; Rodriguez, Reid, and Johnson, 2013; Rodriguez *et al.*, 2013) methods.

volume-integral formulation in which each body is discretized into point dipolar particles with equivalent Clausius-Mossotti polarizabilities: this approximation typically yields accurate results for dielectric media but suffers from poor convergence when simulating metals with highly delocalized plasmons. In contrast, volume-integral formulations guaranteed to converge require a so-called Galerkin discretization of the problem based on the use of either voxel (Polimeridis, Reid, Johnson *et al.*, 2015) or Schaubert-Wilton-Glisson tetrahedral (Reid *et al.*, 2017) basis functions. In either case, the basis functions may be identical and displaced on a regular grid or lattice covering each body, in which case the matrix representation of $\mathbb{G}_0$ may be sparse (and therefore computationally easier to handle) due to the translational symmetries inherent in $\mathbb{G}_0$, although this often comes at the cost of computing matrix elements of $\mathbb{G}_0$ for regions where no materials are present or of losing flexibility over discretizing certain regions more finely than others (Polimeridis, Reid, Jin *et al.*, 2015). Exactly the opposite trade-off occurs if the volumes are discretized in an irregular manner, with different weights given to different basis functions (Reid *et al.*, 2017): it then becomes possible to discretize certain regions more finely than others, which is of particular relevance to near-field radiative heat transfer between large bodies where only a few fine features are close to one another, but at the cost of the matrix representation of $\mathbb{G}_0$ becoming dense due to the loss of obvious symmetries in the representation. Furthermore, in all cases volume-integral formulations can model inhomogeneous and anisotropic susceptibilities and even temperature gradients (Polimeridis, Reid, Jin *et al.*, 2015; Jin, Polimeridis, and Rodriguez, 2016), but modeling nonlocal susceptibilities has proven to be more of a challenge.

A class of techniques related to the volume-integral formulation are those based on the surface-integral formulation (Rodriguez, Reid, and Johnson, 2013; Rodriguez *et al.*, 2013) of Maxwell's equations. These techniques compute the Landauer energy transmission spectrum $\mathcal{T}$ according to a formula that looks superficially similar to Eq. (16) but whose derivation and implementation require a different set of techniques. In particular, surface-integral formulations make consistent use of the surface equivalence theorem (Harrington, 1989; Rengarajan and Rahmat-Samii, 2000; Reid, White, and Johnson, 2013; Rodriguez, Reid, and Johnson, 2013; Otey *et al.*, 2014; Reid and Johnson, 2015) to recast all free polarization sources and total electromagnetic fields in terms of equivalent surface currents, with the relevant operators being the Green's functions of the homogeneous susceptibilities composing each body, as well as the surface-integral operator relating incident fields to induced equivalent surface currents. In principle, the operators relevant to the surface-integral formulation can be expanded in a spectral basis (Rodriguez, Reid, and Johnson, 2013), but, as in the T-operator formulation, convergence suffers for bodies that do not exhibit requisite symmetries. Instead, it is more common to expand the relevant operators in a localized basis like the Rao-Wilton-Glisson basis (Rodriguez, Reid, and Johnson, 2013; Rodriguez *et al.*, 2013) of tetrahedral functions.

Finally, we point out that any of these frequency domain methods could have instead been cast in the time domain. In the context of computational electromagnetism, this is most commonly achieved by using the finite-difference time-domain method (Luo *et al.*, 2004; Rodriguez *et al.*, 2011). This has many of the same benefits and detriments of the aforementioned finite-difference frequency domain method. Techniques based on molecular dynamics have also been used to compute radiative heat transfer in systems comprising nanoparticles (Domingues *et al.*, 2005), although the scaling of the volume with the cube of the number of atoms makes computations unwieldy in practice for large nanoparticles. For both of these time-domain techniques, the main advantages are their generality with respect to materials, the simple computational implementation (as the temporal evolution operators are represented as sparse matrices), the ability to extract dynamical information, and their ability in principle to incorporate *nonlinear* material response. In the case of molecular dynamics, susceptibilities can be simulated fairly generally, as the method is based on simulating classical Newtonian particle dynamics, though interactions other than harmonic or Coulomb couplings are typically based on empirical rather than *ab initio* models. The main disadvantages for both sets of techniques are losses in computational efficiency from needing to explicitly simulate fluctuating polarization sources obeying fluctuation-dissipation statistics, which requires that averages be taken over a large ensemble of calculations.

G. Upper bounds on near-field heat transfer

As previously noted, the Stefan-Boltzmann formula or blackbody limit was derived over a century ago under the assumptions of ray optics, and it consequently fails to provide an upper bound of the maximum heat flux that can be extracted from an object in the near-field regime. While it is known that, as in far-field emission, the appropriate choice of object geometry (nanostructuring) and materials can enhance NFRHT, the lack of such a limit applicable in the near field begs the question: how much more room for improvement can be expected from either of these design criteria? Over the past few decades, there have been several successful attempts at addressing this fundamental question, starting with analyses of maximum NFRHT achievable in planar geometries (where the main design criterion is the choice of material) (Volokitin and Persson, 2004; Ben-Abdallah and Joulain, 2010; Biehs, Tschikin, and Ben-Abdallah, 2012) and followed more recently by limits applicable to arbitrary nanostructures and materials (Miller, Johnson, and Rodriguez, 2015; Venkataram *et al.*, 2020). Technically speaking, upper limits to the heat flux are determined by bounds on the transmission coefficient $\mathcal{T}(\omega)$ per unit area in Eq. (5), which is itself determined by the per-channel transmission factors $\tau_n(\omega)$ entering Eq. (6). The aim of arriving at a bound on RHT is therefore to discern the maximum number and contribution of tranmission channels that may be excited by a yet unknown optimal choice of material and geometry.

In the case of two planar bodies, the maximum heat flux is determined by the bounds on the transmission coefficient $\mathcal{T}(\omega)$ per unit area in Eq. (7), which is determined by the transmission factor $\tau_\alpha(\omega, \kappa) \in [0, 1]$ corresponding to transversal waves of frequency ω, lateral wave vector κ, and polarization $\alpha = s, p$. We then see that $\mathcal{T}(\omega)$ can be maximized if the transmission factor $\tau_\alpha(\omega, \kappa)$ is maximal over a broad frequency and lateral wave vector range. For example, when assuming that at a given frequency all transversal waves contribute a maximal transmission factor of unity up to some threshold value $\kappa_{\max}$, the upper bound for the transmission coefficient per unit area between two planar bodies can be written as

$$\mathcal{T}_{\text{pl}}(\omega) \leq 2 \int_0^{\kappa_{\max}} \frac{d\kappa}{2\pi} \kappa = N(\omega), \tag{17}$$

where $N(\omega)$ may be interpreted as the number of contributing transmission modes or channels per unit area (Ben-Abdallah and Joulain, 2010; Biehs and Greffet, 2010a). By definition, the contribution of propagating waves is restricted to $\kappa < k_0$. Hence, setting $\kappa_{\max} = k_0$ one obtains the maximum value of $\mathcal{T}(\omega) = k_0^2/2\pi$ for propagating waves. Inserting this maximum value into Eq. (7), one finds that the largest heat flux $\Phi_{\text{pr}}^{\max}$ that can ever be carried by propagating waves is precisely the blackbody value Φ_{BB} given by Stefan-Boltzmann's law (Planck, 1914; Bergman *et al.*, 2011). Thus, it is the additional contribution coming from evanescent waves with $\kappa \geq k_0$ and not accounted for in Stefan-Boltzmann's law that allows NFRHT to surpass the blackbody limit.

At first glance, it may appear that there is no upper bound to $\kappa_{\max}$ in the evanescent sector, at least within the scope of local continuum electromagnetism, suggesting that $\mathcal{T}_{\mathrm{pl}}(\omega)$ is unbounded. However, even simple considerations imply otherwise. For instance, inside a dielectric the largest possible lateral wave vector allowed is given by the edge of the Brillouin zone π/a, where a is the lattice constant of the medium. Hence, only waves up to wave vectors $\kappa_{\max} \approx \pi/a$ contribute heat flux. Ignoring possible band degeneracies and physical constraints imposed by material and geometric considerations, this gives the following idealized upper bound on the maximum possible heat flux between two dielectrics (Volokitin and Persson, 2004):

$$\Phi_{\mathrm{pl,ideal}}^{\max} \approx \frac{k_{\mathrm{B}}^2 \pi^2}{24\hbar a^2}(T_1^2 - T_2^2). \tag{18}$$

Assuming a wave vector cutoff set by a lattice constant of the order of the atomic scale ($a \approx 10^{-10}$ m) and room-temperature operation ($T_1 = 300$ K and $T_2 = 0$ K) yields a heat flux of the order of 10^{13} W m^{-2} that is unrealistically large compared to the blackbody value of about 460 W m^{-2}. Taking into account the nature of evanescent waves within the vacuum gap between the two planar materials, one may derive a more sensible upper bound. For instance, the field amplitude of evanescent waves of a given κ in the quasistatic regime drops exponentially as $\exp(-\kappa z)$ with respect to the distance z from the interface. As a consequence, one can expect that only evanescent waves having $1/\kappa \approx z > d$ or $\kappa < 1/d$ can meaningfully contribute to the heat flux between two planar interfaces a distance d apart, suggesting that $\kappa_{\max} \approx 1/d$. Ben-Abdallah and Joulain (2010) argued that only evanescent modes with $1/\kappa \approx z > d/2$ overlap significantly and contribute, so a distance-dependent cutoff $\kappa_{\max} \approx 2/d$ is used to provide an estimate of the upper limit for $\mathcal{T} \leq 2/\pi d^2$, leading to the following gap-dependent upper bound on the net heat flux (Ben-Abdallah and Joulain, 2010):

$$\Phi_{\mathrm{pl,gap}}^{\max} = \frac{k_{\mathrm{B}}^2}{6\hbar d^2}(T_1^2 - T_2^2). \tag{19}$$

The choice of $\kappa_{\max} = 1/d$ would decrease this estimate by a factor of 1/4. Note that this cutoff is consistent with the fact that $\mathcal{T}$ scales as $\exp(-2\kappa d)$ with the separation distance d. A similar simple and general, albeit material-independent, expression for the upper limit of the heat-flux contribution has also been found in the case of two hyperbolic metamaterials (Biehs, Tschikin, and Ben-Abdallah, 2012).

Material considerations further constrain the allowed heat flux between planar media. In particular, Biehs and Greffet (2010a) derived a more realistic frequency-dependent cutoff $\kappa_{\max} = \ln[2/\mathrm{Im}(\chi)]/d$ that accounts for the impact of material absorption through the material-specific loss rate $\mathrm{Im}[\chi(\omega)]$, where χ is the medium's susceptibility. In particular, knowledge of the analytical form of the reflection coefficients at an interface can be used to show that the maximum flux occurs for materials satisfying the surface-mode resonance condition $\mathrm{Re}(1/\chi) = -1/2$. The fact that in the quasistatic regime the heat flux scales like $1/d^2$ can be understood from the fact that the number of contributing evanescent modes per unit area scales like $1/d^2$ (Ben-Abdallah and Joulain, 2010; Biehs and Greffet, 2010a; Biehs, Tschikin, and Ben-Abdallah, 2012). Generalizations of related analyses to bound the performance of planar metasurfaces (nanstructured materials with subwavelength systems) have recently been made (Biehs, Tschikin, and Ben-Abdallah, 2012; Miller, Johnson, and Rodriguez, 2014), showing for instance that metasurfaces cannot significantly enhance NFRHT beyond planar thin films.

Efforts aimed at identifying the number and relative contribution of transmission channels that may arise in nonplanar media require a different framework. Recently Miller, Johnson, and Rodriguez (2015) recast radiative heat transfer between two bodies as a series of independent absorption and emission problems (ignoring additional constraints posed by the presence of multiple scattering among the two objects) to obtain bounds that depend only on the bodies' material susceptibilities and separation. In particular, recent work showed that, given an incident field on an object of susceptibility $\chi(\omega)$, the maximum polarization field that can arise at any point inside the object at a frequency ω depends on the "material response factor" (Miller *et al.*, 2016)

$$\zeta(\omega) = \frac{|\chi(\omega)|^2}{\mathrm{Im}[\chi(\omega)]}. \tag{20}$$

Such a figure of merit yields a measure of the resistivity or dissipation of the medium and thereby captures the impact of losses on the resonant optical response of a body. The material response factor arises from the optimal magnitude of the T operator for maximal absorption in isolation (Miller *et al.*, 2016) and encodes electromagnetic many-body and multiple-scattering effects within the body in isolation; this optimal magnitude is achievable at a polaritonic resonance, determined by the value of $\mathrm{Re}(1/\chi)$, which in turn can be tailored through nanostructuring. Exploiting the maximum polarization responsivity of a medium in combination with electromagnetic reciprocity, Miller *et al.* (2016) found an upper bound on the net transmission $\mathcal{T} \leq 4\zeta_1\zeta_2 \int_{V_1} d\mathbf{r}' \int_{V_2} d\mathbf{r} \sum_{i,j} |G_0(\omega, \mathbf{r}, \mathbf{r}')|^2$ that depends quadratically on the effective loss rate of the system $\zeta = \sqrt{\zeta_1\zeta_2}$, with ζ_1 and ζ_2 denoting the material factors of the bodies, and on the integral of the vacuum Green's function over volumes V_1 and V_2 representing *any convenient domain* that may contain bodies 1 and 2, respectively. Such a double integral may be cast as a Frobenius norm of the off-diagonal matrix $\mathbb{G}_{0(2,1)}$, which was previously identified in related works by Miller (2000, 2007) on optical communication limits. However, such an analysis crucially depends on the assumption that each body is capable of simultaneously and optimally emitting electromagnetic fields in the absence of the other, and of optimally absorbing electromagnetic fields in the presence of the other, which effectively neglects additional physical constraints arising from the unavoidable impact of multiple scattering between the two bodies. As a result, the limits have been shown to be tight in situations where multiple scattering can be neglected, namely, quasistatic media subject to relatively large material losses (Jin *et al.*, 2019). This problem becomes particularly acute in the context of bounds on extended structures, where the inability to account for tighter bounds on the transmission eigenvalues causes the quadratic dependence on ζ to far outstrip the observed logarithmic dependence on ζ seen in polaritonic planar media near the resonance condition $\mathrm{Re}(1/\chi) = -1/2$ (and predicted by the previous planar bounds), suggesting more room for enhancements in NFRHT through nanostructuring than has been observed in practice.

In recent work, Molesky *et al.* (2020) and Venkataram *et al.* (2020) developed a set of algebraic techniques to derive tighter bounds on NFRHT that incorporate not only constraints on material response but also multiple scattering. Specifically, the transmission coefficient for two arbitrarily shaped bodies at any given frequency ω was found to be bounded above by

$$\mathcal{T}_{\mathrm{arb}}(\omega) = \sum_n \tau_n(\omega) \leq \sum_n \begin{cases} 1, & \zeta_1\zeta_2 g_n^2 \geq 1, \\ \frac{4\zeta_1\zeta_2 g_n^2}{(1+\zeta_1\zeta_2 g_n^2)^2}, & \zeta_1\zeta_2 g_n^2 < 1, \end{cases} \tag{21}$$

where the dependence on ω inside the various factors has been deprecated. These bounds depend on not only the resistivity $\zeta_i(\omega)$ of each body $i = \{1,2\}$ at the given frequency but also a set of "radiative efficacy" coefficients $g_n(\omega)$ denoting the singular values of the *vacuum* off-diagonal Maxwell Green's function $\mathbb{G}_{0(2,1)}$ connecting dipoles in one object to the resulting fields on the other, and thereby quantifying how strongly these two volumes may be coupled by electromagnetic waves. Moreover, the bounds move beyond simply identifying the set of channels able to contribute to heat transfer, previously estimated on the basis of the effective rank of $\mathbb{G}_{0(2,1)}$, and instead exploit the specific singular values of $\mathbb{G}_{0(2,1)}$ in combination with the loss rate of the medium to quantitatively determine the maximum possible transmission for each channel. Once the set of channels that could possibly contribute (having nonzero radiative coupling g_n) is identified, the ability of each transmission channel to saturate the Landauer upper bound of unity ($\tau_n \leq 1$) is determined by the degree to which the radiative rate of energy transport is able to overcome material losses, captured by the condition $\zeta_1\zeta_2 g_n^2 \geq 1$; the per-channel bound is less than unity for those channels unable to meet such a condition. In addition to correctly reproducing the transition and eventual saturation in the growth of NFRHT between dipolar nanoparticles, from material-loss-dominated growth in the polarization response to the Landauer transmission bounds of unity, these limits reveal that extended nanostructured bodies cannot significantly outperform resonant planar polaritonic slabs even in principle. Specifically, evaluation of the radiative efficacies for any set of nanostructures contained within semi-infinite half-space domains yields a limit on the net transmission of

$$\mathcal{T}_{\mathrm{arb}}(\omega) \times d^2/A \leq \frac{1}{2\pi} \times \begin{cases} \ln\left(1 + \frac{\zeta_1\zeta_2}{4}\right), & \zeta_1\zeta_2 < 4, \\ \frac{1}{2}\ln(\zeta_1\zeta_2) + \frac{1}{8}\left[\ln\left(\frac{\zeta_1\zeta_2}{4}\right)\right]^2, & \zeta_1\zeta_2 \geq 4, \end{cases} \tag{22}$$

which exhibits a weak squared-logarithmic dependence on ζ, in line with the observed logarithmic peak value of $\mathcal{T}$ for planar slabs at a polaritonic resonance (Biehs and Greffet, 2010a; Miller, Johnson, and Rodriguez, 2015).

Based on this recent analysis, it is evident that the observed inability of nanostructuring to significantly enhance the amplitude of $\mathcal{T}$ at any given frequency beyond what is achievable with resonant planar materials is a "feature" of the underlying physics of NFRHT, not a "bug" in sampling a limited design space: the maximum channel able to saturate the Landauer transmission limit of unity for any nanostructure scales logarithmically as $(1/2d)\ln(\zeta_1\zeta_2/4)$ provided that the system is in the underdamped resonant regime $\zeta_1\zeta_2 \geq 4$. Intuitively, this result may be seen as dissonant with the established utility of nanostructuring for enhancing far-field electromagnetic absorption and scattering, and the significantly stronger enhancements of local densities of states that can arise in the vicinity of structured materials. However, the channels of radiative heat transfer between two separable bodies in proximity have little to do with the channels that carry energy away from a body (or an aggregate two-body system), so there is no reason to believe that enhancement of the latter transmission channel contributions would necessarily increase the former.

The transition from a quadratic (Miller, Johnson, and Rodriguez, 2015) to a much weaker logarithmic (Venkataram *et al.*, 2020) dependence of the bounds on material conductivity once multiple-scattering constraints are introduced illustrates the restricted and prohibitive nature of nanostructuring in tailoring mutual scattering across a wide range of resonant channels. Such a trade-off precisely explains why the success of nanostructuring in enhancing local fields does not readily translate into equivalent enhancements in NFRHT. As reviewed in Secs. II.B and II.D, metallic nanostructures can indeed greatly enhance heat exchange compared to their planar counterparts, but, as these limits suggest, not much more than what may be achieved with planar polar dielectrics. Finally, while multiple scattering ultimately hampers the maximum heat exchange that any two bodies can experience, as we see in Sec. III, it underlies several important transport effects in many-body systems.

III. MANY-BODY SYSTEMS

Until the past decade, theoretical and experimental work on the topic of near-field radiative heat transport was primarily relegated to the study of heat exchange between two objects, while transport in systems composed of objects in mutual interactions remained largely unexplored and out of the reach of classical FE. Ben-Abdallah, Biehs, and Joulain (2011) laid out the theoretical foundations for studying NFRHT in simple many-body systems made of small interacting objects in the dilute regime, paving the way for a new research direction on the topic of nanoscale heat-transfer. Since 2011, numerous works have revealed new many-body effects, including the emergence of new physical and transport behaviors, and unraveling a large number of potential applications in domains such as nanoscale thermal management, energy-conversion technology, and information processing. In Secs. III.A–III.D, we describe these peculiarities.

A. Heat flux in dipolar many-body systems

Understanding the mechanisms that drive light matter interactions is one of the main goals of optics. In the following, we address the problem of light absorption and thermal emission by a set of small objects in which cooperative interactions as well as heat exchange take place.

1. Light absorption in dipolar systems

To start we consider the case of nonemitting objects that are able to scatter and absorb light only from an external source, i.e., we are neglecting thermal radiation at this stage. In the simplest case of a small isolated particle located at position $\mathbf{r}'$ in vacuum, the optical response of this particle can be described by the response to a simple permanent dipolar electric moment $\mathbf{p}(\mathbf{r}')$.

The electric field produced at point $\mathbf{r}$ around this dipole takes the following form:

$$\mathbf{E}_{\mathrm{p}}(\mathbf{r}) = \omega^2\mu_0\mathbb{G}_0(\mathbf{r},\mathbf{r}')\mathbf{p}(\mathbf{r}'). \tag{23}$$

Here (Novotny and Hecht, 2006)

$$\mathbb{G}_0(\mathbf{r},\mathbf{r}') = \frac{\exp(ik_0\rho)}{4\pi\rho}\left[\left(1+\frac{ik_0\rho-1}{k_0^2\rho^2}\right)\mathbb{1} + \frac{3-3ik_0\rho-k_0^2\rho^2}{k_0^2\rho^2}\hat{\boldsymbol{\rho}}\otimes\hat{\boldsymbol{\rho}}\right] \tag{24}$$

is the free-space Green tensor defined with the unit vector $\hat{\boldsymbol{\rho}} \equiv \boldsymbol{\rho}/\rho$, $\boldsymbol{\rho} = \mathbf{r}-\mathbf{r}'$, $k_0 = \omega/c$ is the wave vector, $\mathbb{1}$ denotes the unit dyadic tensor, and μ_0 denotes the vacuum permeability. When this particle is illuminated by an incident field $\mathbf{E}_{\mathrm{inc}}$, the local electric field $\mathbf{E}_{\mathrm{loc}}$ measured at any point $\mathbf{r}$ is the superposition of the incident field and the field generated (scattered) by the dipole. Therefore, according to Eq. (23), this field decomposes into

$$\mathbf{E}_{\mathrm{loc}}(\mathbf{r}) = \mathbf{E}_{\mathrm{inc}}(\mathbf{r}) + \omega^2\mu_0\mathbb{G}_0(\mathbf{r},\mathbf{r}')\mathbf{p}(\mathbf{r}'). \tag{25}$$

The electromagnetic power $\mathcal{P}$ dissipated in the particle can be calculated from the rate of work

$$\mathcal{P}_{\mathrm{abs}} = \frac{1}{2}\int_V dV\,\mathrm{Re}(\mathbf{j}^*\cdot\mathbf{E}_{\mathrm{loc}}) \tag{26}$$

done by the electromagnetic field in a volume V including the particle. Here $\mathbf{j}$ denotes the local electric current density in the volume V. In the dipolar approximation $\mathbf{j}(\mathbf{r}') = -i\omega\mathbf{p}\delta(\mathbf{r}-\mathbf{r}')$ so that

$$\mathcal{P}_{\mathrm{abs}} = \frac{1}{2}\mathrm{Re}(i\omega\mathbf{p}^*\cdot\mathbf{E}_{\mathrm{loc}}) = -\frac{\omega}{2}\mathrm{Im}(\mathbf{p}^*\cdot\mathbf{E}_{\mathrm{loc}}). \tag{27}$$

Using the relation

$$\mathbf{p}(\mathbf{r}') = \epsilon_0\alpha\mathbf{E}_{\mathrm{inc}}(\mathbf{r}') \tag{28}$$

between the incident field and the dipolar moment, where α is the electric polarizability, the power dissipated in the particle reads (Tretyakov, 2014)

$$\mathcal{P}_{\mathrm{abs}} = \frac{\omega|\mathbf{E}_{\mathrm{inc}}|^2\epsilon_0}{2}\left(\mathrm{Im}[\alpha] - \frac{k_0}{6\pi}|\alpha|^2\right). \tag{29}$$

It is common to quantify light absorption using the absorption cross section defined as the ratio

$$\sigma_{\mathrm{abs}} = \frac{\mathcal{P}_{\mathrm{abs}}}{\mathcal{F}_{\mathrm{inc}}} \tag{30}$$

of this dissipated power by the incident flux

$$\mathcal{F}_{\mathrm{inc}} = \frac{c\epsilon_0}{2}|\mathbf{E}_{\mathrm{inc}}|^2. \tag{31}$$

For a collection of dipoles located at the position $\mathbf{r}_i$ $(i = 1,\ldots,N)$ the multiscattering process between the particles must be taken into account (Langlais *et al.*, 2014). Under an external illumination by an incident field $\mathbf{E}_{\mathrm{inc}}$, the local electric field $\mathbf{E}_{\mathrm{loc}}$ measured at any point results from the superposition of the incident and all scattered fields as

$$\mathbf{E}_{\mathrm{loc}}(\mathbf{r}) = \mathbf{E}_{\mathrm{inc}}(\mathbf{r}) + \omega^2\mu_0\sum_{j=1}^{N}\mathbb{G}_0(\mathbf{r},\mathbf{r}_j)\mathbf{p}_j. \tag{32}$$

When we introduce the notation $\mathbf{p}_i = \mathbf{p}(\mathbf{r}_i)$, $\mathbf{E}_{\mathrm{loc},i} = \mathbf{E}_{\mathrm{loc}}(\mathbf{r}_i)$, and $\mathbf{E}_{\mathrm{inc},i} = \mathbf{E}_{\mathrm{inc}}(\mathbf{r}_i)$ the total power absorbed by this set of dipoles takes the general form (Hugonin, Besbes, and Ben-Abdallah, 2015)

$$\mathcal{P}_{\mathrm{abs}} = \frac{\omega}{2}\left(\sum_{i=1}^{N}\mathrm{Im}(\mathbf{p}_i\cdot\mathbf{E}^*_{\mathrm{inc},i}) - \sum_{i,j=1}^{N}\mathrm{Im}(\mathbf{p}^*_i\boldsymbol{D}_{ij}\mathbf{p}_j)\right), \tag{33}$$

where we have introduced the $N\times N$ block matrix

$$\boldsymbol{D}_{ij} = \mu_0\omega^2\mathbb{G}_0(\mathbf{r}_i,\mathbf{r}_j). \tag{34}$$

Equation (34) generalizes Eq. (29) to arbitrary systems of coupled dipoles. For isotropic and homogeneous particles the generalized vector field of dipolar moments reads

$$\begin{pmatrix} \mathbf{p}_1 \\ \vdots \\ \mathbf{p}_N \end{pmatrix} = \mathbf{A} \begin{pmatrix} \mathbf{E}_{\mathrm{loc},1} \\ \vdots \\ \mathbf{E}_{\mathrm{loc},N} \end{pmatrix}, \tag{35}$$

introducing the block matrix

$$\boldsymbol{A}_{ij} = \epsilon_0 \delta_{ij} \underline{\underline{\alpha}}_i, \tag{36}$$

where $\underline{\underline{\alpha}}_i$ is the electric polarizability tensor associated with the particle i. Using Eq. (32), this expression can be reformulated with respect to the vectorial incident field as

$$\begin{pmatrix} \mathbf{p}_1 \\ \vdots \\ \mathbf{p}_N \end{pmatrix} = \boldsymbol{A}\tilde{\boldsymbol{T}}^{-1} \begin{pmatrix} \mathbf{E}_{\mathrm{inc},1} \\ \vdots \\ \mathbf{E}_{\mathrm{inc},N} \end{pmatrix}, \tag{37}$$

with

$$\tilde{\boldsymbol{T}}_{ij} = \delta_{ij}\mathbb{1} - (1-\delta_{ij}) k_0^2 \mathbb{G}_0(\mathbf{r}_i, \mathbf{r}_j) \underline{\underline{\alpha}}_j. \tag{38}$$

This block matrix $\tilde{\boldsymbol{T}}^{-1}$ defines the interplay between all dipoles and the block matrix

$$\boldsymbol{\alpha}_{\mathrm{dr}} = \frac{1}{\epsilon_0} \boldsymbol{A}\tilde{\boldsymbol{T}}^{-1}, \tag{39}$$

also called dressed polarizability (Castanié *et al.*, 2012), results from the multiscattering process in the set of dipoles. Using the slightly different block matrix

$$\boldsymbol{T}_{ij} = \delta_{ij}\mathbb{1} - (1-\delta_{ij}) k_0^2 \underline{\underline{\alpha}}_i \mathbb{G}_0(\mathbf{r}_i, \mathbf{r}_j), \tag{40}$$

it can also be expressed as

$$\boldsymbol{\alpha}_{\mathrm{dr}} = \frac{1}{\epsilon_0} \boldsymbol{T}^{-1}\boldsymbol{A} \tag{41}$$

because $\boldsymbol{T}\boldsymbol{A} = \boldsymbol{A}\tilde{\boldsymbol{T}}$ and $\boldsymbol{T}^{-1}\boldsymbol{A} = \boldsymbol{A}\tilde{\boldsymbol{T}}^{-1}$. This dressed polarizability shows that two types of resonances play a role in the interaction of light with the set of coupled dipoles. The first ones are the resonances of the isolated particles themselves (i.e., the poles of $\underline{\underline{\alpha}}_i$), while the second ones (i.e., the poles of the determinant of α_{dr} or $\boldsymbol{T}^{-1}$) are configurational resonances (see Fig. 11) and they depend on the spatial distribution of dipoles. Therefore, the $3N$ dipolar resonances that are degenerate for spherical nanoparticles couple and form a band of $3N$ resonances in general. Depending on the symmetry in the configuration some of the resonances remain degenerate despite the coupling. A simple example is a chain of nanoparticles. There one finds N twofold degenerate vertical and N longitudinal resonances (Weber and Ford, 2004) forming bands of coupled modes. A general consequence of this dressing due to the coupling is a broadening of the absorption spectrum in a coupled N-dipole system.

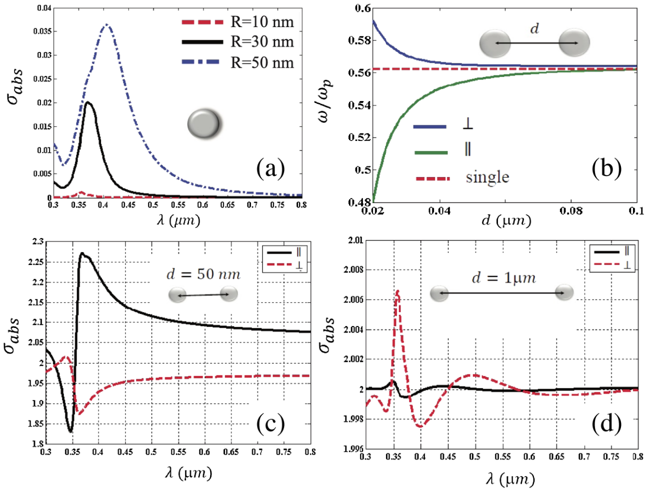

FIG. 11. (a) Absorption cross section of spherical silver nanoparticles with respect to the wavelength. (b) Orthogonal and parallel configurational resonance frequencies for a dimer of silver nanoparticles ($R = 10$ nm) in vacuum with respect to their separation distance d. The red horizontal line represents the plasmon resonance of an isolated particle. (c),(d) Absorption cross sections for a dimer of silver nanoparticles ($R = 10$ nm) normalized by the absorption of a single particle. From Raj, Van de Voorde, and Mahajan, 1995.

2. Exchanged power and Poynting vector

Now we consider the most general situation where the particles are also emitting heat radiation. The fundamental relations to describe heat exchange in a system of N dipoles having temperatures $T_1, \ldots, T_N$ within the framework of the FE were first derived by Ben-Abdallah, Biehs, and Joulain (2011). Messina, Tschikin *et al.* (2013) generalized the relations for the heat exchange to also treat the interaction of the N dipolar objects with an environment or background in thermal equilibrium at some temperature T_b (i.e., the temperature of the surrounding radiation field), but only for isotropic dipolar objects. Subsequently, these expressions were extended to anisotropic and nonreciprocal systems by also taking the radiation correction into account (Nikbakht, 2014; Ekeroth, García-Martín, and Cuevas, 2017), and the expression for the mean Poynting vector of such an N-dipole system has been determined to quantify its far-field thermal emission (Ekeroth, García-Martín, and Cuevas, 2017). Finally, Ott *et al.* (2019a) and Ott and Biehs (2020) used the method of Messina, Tschikin *et al.* (2013) to determine the general expressions for the mean Poynting vector and the exchanged heat in a system of N dipoles immersed in an environment at temperature T_b that can also be nonreciprocal. A further generalization that takes the possibility of magnetic polarizabilities into account was given by Manjavacas and de Abajo (2012) and Dong, Zhao, and Liu (2017a). Here we review mainly the derivation of the heat exchange and the mean Poynting vector for N dipolar objects described by an electric polarizability tensor $\underline{\underline{\alpha}}$ within the framework of Messina, Tschikin *et al.* (2013). This approach is valid for nanoparticles with a size much smaller than the thermal wavelength and for interparticle distances and distance between the particles and interfaces of the environment larger than twice the diameter (Narayanaswamy and Chen, 2008; Otey and Fan, 2011; Becerril and Noguez, 2019).

To derive the exchanged power and the mean Poynting vector in an N-dipole system, we consider the total electric and magnetic fields

$$\mathbf{E}(\mathbf{r},\omega) = \omega^2\mu_0 \sum_{i=0}^{N} \mathbb{G}^{\mathrm{EE}}(\mathbf{r},\mathbf{r}_i)\mathbf{p}_i + \mathbf{E}^b(\mathbf{r},\omega), \tag{42}$$

$$\mathbf{H}(\mathbf{r},\omega) = \omega^2\mu_0 \sum_{i=0}^{N} \mathbb{G}^{\mathrm{HE}}(\mathbf{r},\mathbf{r}_i)\mathbf{p}_i + \mathbf{H}^b(\mathbf{r},\omega), \tag{43}$$

which are generated by the fluctuational background fields $\mathbf{E}^b(\mathbf{r})$ and $\mathbf{H}^b(\mathbf{r})$ and the induced and fluctuational dipoles of all particles ($i = 1, \ldots, N$)

$$\mathbf{p}_i = \mathbf{p}_i^{\mathrm{ind}} + \mathbf{p}_i^{\mathrm{fl}}, \tag{44}$$

where the induced dipole moments

$$\mathbf{p}_i^{\mathrm{ind}} = \epsilon_0 \underline{\underline{\alpha}}_i \mathbf{E}(\mathbf{r}_i) \tag{45}$$

can be expressed in terms of the polarizability tensor $\underline{\underline{\alpha}}_i$ of the ith dipole. Here we have introduced the electric and magnetic Green's functions $\mathbb{G}^{\mathrm{EE}}$ and $\mathbb{G}^{\mathrm{HE}}$ generated by electric dipole moments as defined by Eckhardt (1984), which are now not necessarily the vacuum Green's functions, but rather the general Green's functions taking the geometry and material properties of the background into account. As a consequence the total electric field $\mathbf{E}_i = \mathbf{E}(\mathbf{r}_i)$ at the position of the ith dipole is given by the field contributions due to the fluctuating dipole moments $\mathbf{p}_j^{\mathrm{fl}}$ of all other dipoles $j \neq i$ and the background field $\mathbf{E}_i^b = \mathbf{E}^b(\mathbf{r}_i)$ including direct thermal emission and multiple scattering. It can be written as (Messina, Tschikin *et al.*, 2013)

$$\begin{pmatrix} \mathbf{E}_1 \\ \vdots \\ \mathbf{E}_N \end{pmatrix} = \boldsymbol{D}\boldsymbol{T}^{-1} \begin{pmatrix} \mathbf{p}_1^{\mathrm{fl}} \\ \vdots \\ \mathbf{p}_N^{\mathrm{fl}} \end{pmatrix} + (\mathbf{1} + \boldsymbol{D}\boldsymbol{T}^{-1}\boldsymbol{A}) \begin{pmatrix} \mathbf{E}_1^b \\ \vdots \\ \mathbf{E}_N^b \end{pmatrix}. \tag{46}$$

Similarly the induced dipole moments $\mathbf{p}_i$ for each particle i can be expressed in terms of the fluctuating dipole moments of all other particles and the background field (Messina, Tschikin *et al.*, 2013)

$$\begin{pmatrix} \mathbf{p}_1 \\ \vdots \\ \mathbf{p}_N \end{pmatrix} = \boldsymbol{T}^{-1} \begin{pmatrix} \mathbf{p}_1^{\mathrm{fl}} \\ \vdots \\ \mathbf{p}_N^{\mathrm{fl}} \end{pmatrix} + (\boldsymbol{T}^{-1}\boldsymbol{A}) \begin{pmatrix} \mathbf{E}_1^b \\ \vdots \\ \mathbf{E}_N^b \end{pmatrix}. \tag{47}$$

The auxiliary $(3N \times 3N)$-block matrices $\boldsymbol{D}$, $\boldsymbol{A}$, and $\boldsymbol{T}$ are defined as in Eqs. (34), (36), and (40) but with the vacuum Green's function $\mathbb{G}_0(\mathbf{r}_i, \mathbf{r}_j)$ replaced by $\mathbb{G}_{ij}^{\mathrm{EE}} = \mathbb{G}^{\mathrm{EE}}(\mathbf{r}_i, \mathbf{r}_j)$ and $\mathbf{1}_{ij} = \delta_{ij}\mathbb{1}$.

Equipped with this set of expressions it is now possible to derive the dissipated heat in a given dipole i and the mean Poynting vector in a general N-dipole system. Analogous to Eq. (26) the mean power received by the ith dipole is defined as the power dissipated in dipole i

$$\begin{aligned} \mathcal{P}_i &= \left\langle \frac{d\mathbf{p}_i(t)}{dt} \cdot \mathbf{E}_i(t) \right\rangle \\ &= 2\mathrm{Im} \int_0^\infty \frac{\mathrm{d}\omega}{2\pi} \omega \langle \mathbf{p}_i(\omega) \cdot \mathbf{E}_i^*(\omega) \rangle. \end{aligned} \tag{48}$$

Hence, by definition the dissipated power inside dipole i, i.e., the heat flowing into that dipole, is positive. The mean Poynting vector due to the dipoles and the background fields is given by

$$\begin{aligned} \langle \mathbf{S}(\mathbf{r}) \rangle &= \langle \mathbf{E}(t) \times \mathbf{H}(t) \rangle \\ &= 2\mathrm{Re} \int_0^\infty \frac{d\omega}{2\pi} \langle \mathbf{E}(\mathbf{r},\omega) \times \mathbf{H}^*(\mathbf{r},\omega) \rangle. \end{aligned} \tag{49}$$

These expressions already include the fact that the fluctuational fields and dipole moments are stationary so that the mean power and mean Poynting vector do not depend on time. They can be evaluated by assuming that the fluctuational dipole moments and the background fields are in local thermal equilibrium at temperatures T_i ($i = 1, \ldots, N$) and T_b. Then the mean values for the power and Poynting vector that are given by the correlation functions of the fields and the dipole moments can be evaluated by employing the fluctuation-dissipation theorem (Kubo, 1966) and assuming that the background fields and the dipole moments are statistically independent, i.e., correlation functions between the background field and the fluctuating dipoles $\langle \mathbf{E}^b \otimes \mathbf{p}_i \rangle$ vanish. For the fields the fluctuation-dissipation theorems are (Agarwal, 1975a)

$$\langle \mathbf{E}_i^b \otimes \mathbf{E}_j^{b*} \rangle = 2\omega^2\mu_0\hbar \left(n_b + \frac{1}{2} \right) \frac{\mathbb{G}_{ij}^{\mathrm{EE}} - \mathbb{G}_{ji}^{\mathrm{EE}\dagger}}{2i}, \tag{50}$$

$$\langle \mathbf{E}_i^b \otimes \mathbf{H}_j^b \rangle = 2\omega^2\mu_0\hbar \left(n_b + \frac{1}{2} \right) \frac{\mathbb{G}_{ij}^{\mathrm{EH}} - \mathbb{G}_{ji}^{\mathrm{HE}\dagger}}{2i} \tag{51}$$

using the notation $\mathbb{G}_{ij}^{\mathrm{EH}} = \mathbb{G}^{\mathrm{EH}}(\mathbf{r}_i, \mathbf{r}_j)$ and $\mathbb{G}_{ij}^{\mathrm{HE}} = \mathbb{G}^{\mathrm{HE}}(\mathbf{r}_i, \mathbf{r}_j)$, $n_b = n(\omega, T_b)$. Analogously, for the dipole moments the fluctuation-dissipation theorem is determined by (Messina, Tschikin *et al.*, 2013)

$$\langle \mathbf{p}_i^{\mathrm{fl}} \otimes \mathbf{p}_j^{\mathrm{fl}*} \rangle = 2\epsilon_0\hbar\delta_{ij}(n_i + \tfrac{1}{2}) \underline{\underline{\chi}}_i. \tag{52}$$

The generalized susceptibility of the ith particle is given by (Messina, Tschikin *et al.*, 2013; Ekeroth, García-Martín, and Cuevas, 2017; Herz and Biehs, 2019)

$$\underline{\underline{\chi}}_i = \frac{\underline{\underline{\alpha}}_i - \underline{\underline{\alpha}}_i^\dagger}{2i} - k_0^2 \underline{\underline{\alpha}}_i \frac{\mathbb{G}_{ii}^{\mathrm{EE}} - \mathbb{G}_{ii}^{\mathrm{EE}\dagger}}{2i} \underline{\underline{\alpha}}_i^\dagger. \tag{53}$$

The first term of the generalized susceptibility describes simply the intrinsic absorptivity of the dipole, whereas the second term is a radiation correction taking into account the fact that the dipole is coupled to the environment that modifies its absorptivity. In free space this second term simply reads $-k_0^3/(6\pi)\underline{\underline{\alpha\alpha}}^\dagger$ (Ekeroth, García-Martín, and Cuevas, 2017). Hence, upon comparison with Eq. (29) we see that with $\underline{\underline{\chi}}_i$ we retrieve the absorptivity of a dipole i placed in vacuum for the isotropic case $\underline{\underline{\alpha}}_i = \alpha_i \mathbb{1}$.

Inserting the expressions for the fields and dipole moments into Eq. (48) one obtains for the mean power received by particle i (Ott and Biehs, 2020)

$$\mathcal{P}_i = 3\int_0^\infty \frac{d\omega}{2\pi}\hbar\omega\sum_{j=1}^{N}(n_j - n_b)\mathcal{T}_{ij}, \tag{54}$$

where the transmission coefficients are defined as

$$\mathcal{T}_{ij} = \tfrac{4}{3}\epsilon_0 \mathrm{Im}\mathrm{Tr}[\boldsymbol{T}_{ij}^{-1}\underline{\underline{\chi}}_j(\boldsymbol{D}\boldsymbol{T}^{-1})^\dagger_{ij}]. \tag{55}$$

Equation (54) is the general expression for the dissipated power or heat flowing into a dipole at temperature T_i surrounded by $N-1$ dipoles at temperatures T_j $(j \neq i)$ described by an anisotropic or even nonreciprocal polarizability immersed in a general environment or background at temperature T_b that can itself be anisotropic or nonreciprocal, properties that are taken into account via the polarizability and the Green's function. In general, if the dipole or the background or both are nonreciprocal, one has $\mathcal{T}_{ij} \neq \mathcal{T}_{ji}$ (Zhu, Guo, and Fan, 2018; Herz and Biehs, 2019). Note that in the literature a variety of different equivalent expressions for the transmission coefficients $\mathcal{T}_{ij}$ can be found (Ben-Abdallah, Biehs, and Joulain, 2011; Messina, Tschikin *et al.*, 2013; Nikbakht, 2014; Ekeroth, García-Martín, and Cuevas, 2017; Ott *et al.*, 2019a; Ott and Biehs, 2020). Finally, when replacing $n_j - n_b$ with $n_j - n_i + n_i - n_b$ Eq. (54) can be recast into the more intuitive form (Messina, Tschikin *et al.*, 2013)

$$\mathcal{P}_i = 3\int_0^\infty \frac{d\omega}{2\pi}\hbar\omega\left(\sum_{j\neq i}(n_j - n_i)\mathcal{T}_{ij} + (n_b - n_i)\mathcal{T}_{ib}\right), \tag{56}$$

with $\mathcal{T}_{ib} = \sum_j \mathcal{T}_{ij}$. Equation (56) has the advantage that it expresses the power dissipated into dipole i by the power exchanged between dipole i and all the other dipoles and the power of dipole i exchanged with the environment.

Similarly, by starting with the definition of the mean Poynting vector in Eq. (49) one obtains for the spectral heat flux for the N fluctuating dipoles immersed in a background (Ott and Biehs, 2020)

$$\begin{aligned}\langle S_{\omega,\alpha}\rangle = 4\hbar\omega^2\mu_0 k_0^2 \sum_{\beta,\gamma=x,y,z}\epsilon_{\alpha\beta\gamma}\mathrm{Re}\Bigg[&\sum_{j=1}^{N}(n_j - n_b)\sum_{i=1}^{N}(\mathbb{G}_{0i}^{\mathrm{EE}}\boldsymbol{T}_{ij}^{-1})\underline{\underline{\chi}}_j\sum_{k=1}^{N}(\mathbb{G}_{0k}^{\mathrm{HE}}\boldsymbol{T}_{kj}^{-1})^\dagger \\ &+ \frac{n_b}{2i}\sum_{i,j=1}^{N}[\mathbb{G}_{0i}^{\mathrm{EE}}\boldsymbol{T}_{ij}^{-1}\underline{\underline{\alpha}}_j\mathbb{G}_{j0}^{\mathrm{EH}} - (\mathbb{G}_{0i}^{\mathrm{HE}}\boldsymbol{T}_{ij}^{-1}\underline{\underline{\alpha}}_j\mathbb{G}_{j0}^{\mathrm{EE}})^\dagger] + \frac{n_b}{k_0^2}\left(\frac{\mathbb{G}_{00}^{\mathrm{EH}} - \mathbb{G}_{00}^{\mathrm{HE}\dagger}}{2i}\right)\Bigg]_{\beta\gamma},\end{aligned} \tag{57}$$

where $\epsilon_{\alpha\beta\gamma}$ is the Levi-Civita tensor and $\mathbb{G}_{0i}^{\mathrm{EE}} = \mathbb{G}^{\mathrm{EE}}(\mathbf{r}, \mathbf{r}_i)$, $\mathbb{G}_{00}^{\mathrm{EE}} = \mathbb{G}^{\mathrm{EE}}(\mathbf{r}, \mathbf{r})$, etc. The first term describes the heat flux emitted by the particles into the background, the last term describes the heat flux of the background fields without the dipoles, and the second term describes the interference of the background fields due to the presence of the dipoles. In the case in which the background geometry fulfills Lorentz reciprocity (Caloz *et al.*, 2018), the last term vanishes since then $\mathbb{G}_{ij}^{\mathrm{EH}\dagger} = -\mathbb{G}_{ji}^{\mathrm{HE}*}$. This simply means that if we have no dipoles, the mean heat flux in the background $\langle\mathbf{S}^b\rangle = \langle\mathbf{E}^b(t)\times\mathbf{H}^b(t)\rangle$ that is at local thermal equilibrium vanishes. On the other hand, as shown by Silveirinha (2017) for a nonreciprocal background, there can be a nonvanishing mean Poynting vector even in thermal equilibrium.

In certain cases the heat flux between the dipolar objects is dominant so that the emission into the background is negligibly small. If the dipoles are placed into a vacuum at temperature T_b, then the power exchanged between the dipoles is for distances much smaller than the thermal wavelength, i.e., in the near-field regime, much larger than the power exchange with the background (Messina, Tschikin *et al.*, 2013). When placing the dipolar objects close to a substrate, the interdipole heat exchange still dominates if the distance between the dipoles is much smaller than the distance to the substrate (Ott and Biehs, 2020). In such situations, the N-dipole system can also be treated as a closed system. This can be done by neglecting in the previous expressions the heat exchange between the dipoles and the background and the heat flux due to the background fields so that

$$\mathcal{P}_i = 3\int_0^\infty \frac{d\omega}{2\pi}\hbar\omega\sum_{j\neq i}(n_j - n_i)\mathcal{T}_{ij} \tag{58}$$

and

$$\begin{aligned}\langle S_{\omega,\alpha}\rangle = 4\hbar\omega^2\mu_0 k_0^2 \sum_{\beta,\gamma=x,y,z}\epsilon_{\alpha\beta\gamma}\sum_{j=1}^{N} n_j \\ \times \mathrm{Re}\left[\sum_{i=1}^{N}(\mathbb{G}_{0i}^{\mathrm{EE}}\boldsymbol{T}_{ij}^{-1})\underline{\underline{\chi}}_j\sum_{k=1}^{N}(\mathbb{G}_{0k}^{\mathrm{HE}}\boldsymbol{T}_{kj}^{-1})^\dagger\right]_{\beta\gamma}.\end{aligned} \tag{59}$$

Note that, even though $\mathcal{P}_i$ contains only the power dissipated in dipole i due to the heat exchange with all other dipoles, the mean Poynting vector also includes the thermal radiation of all dipoles into their background, which is assumed to have zero temperature. To be fully consistent with the assumption that the background is simply removed from the description, the second term in the generalized susceptibility $\underline{\underline{\chi}}_j$ in Eq. (53) might be neglected. For systems where the dipole approximation is valid this term is typically small and can therefore often be neglected anyway.

The same equations can be obtained by neglecting in the derivation right from the start any contribution from the background fields. In this case $\mathcal{P}_i$ can also be obtained by considering only the power exchanged between all pairs of dipoles, as originally done in many works, including that of Ben-Abdallah, Biehs, and Joulain (2011). To this end, the heat dissipated in dipole i due to a fluctuational field $\mathbf{E}_{ij} = (\boldsymbol{D}\boldsymbol{T}^{-1})_{ij}\mathbf{p}_j^{\mathrm{fl}}$ generated by a fluctuational dipole $\mathbf{p}_j^{\mathrm{fl}}$ is considered as the power flow from dipole j to i yielding

$$\begin{aligned}\mathcal{P}_{j\to i} &= \left\langle \frac{d\mathbf{p}_i(t)}{dt}\cdot\mathbf{E}_{ij}(t)\right\rangle \\ &= 3\int_0^\infty \frac{d\omega}{2\pi}\hbar\omega n_j \mathcal{T}_{ij}(\omega).\end{aligned} \tag{60}$$

Then the power dissipated by the ith dipole is just the sum of the power flowing between dipole i and the other objects

$$\begin{aligned}\mathcal{P}_i &= \sum_{j\neq i}(\mathcal{P}_{j\to i} - \mathcal{P}_{i\to j}) \\ &= \sum_{j\neq i} 3\int_0^\infty \frac{d\omega}{2\pi}\hbar\omega[n_j\mathcal{T}_{ij}(\omega) - n_i\mathcal{T}_{ji}(\omega)].\end{aligned} \tag{61}$$

Since in thermal equilibrium $\mathcal{P}_i = 0$ we can derive the condition (Latella and Ben-Abdallah, 2017; Ott et al., 2019a)

$$\sum_{j\neq i}\mathcal{T}_{ij}(\omega) = \sum_{j\neq i}\mathcal{T}_{ji}(\omega). \tag{62}$$

Equation (62) simply expresses the fact that, even though $\mathcal{T}_{ij} \neq \mathcal{T}_{ji}$ in general, the heat flux from i to all other dipoles [rhs of Eq. (62)] must be the same as the heat flow from all other dipoles to i [lhs of Eq. (62)] in equilibrium. By inserting this equilibrium condition into the second term of Eq. (61) we retrieve Eq. (58).

3. Nonadditivity in many-dipole systems

Before we discuss the nonadditivity of the power exchange in an N-dipole system based on Eq. (60), we focus on the power exchange between two dipoles ($N = 2$). The first derivation of the heat exchange between two dipolar objects within the framework of FE was given by Volokitin and Persson (2001) and was extended to take magnetic dipole moments into account (Chapuis, Laroche et al., 2008a; Manjavacas and de Abajo, 2012), as well as multipolar contributions (Pérez-Madrid, Rubi, and Lapas, 2008; Becerril and Noguez, 2019). A quantum dynamical description was given by Biehs and Agarwal (2013a) and Barton (2016), and discussions of different prefactors found were conducted by Dedkov and Kyasov (2011) and Sasihithlu (2018). Using our expression in Eq. (60) for $N = 2$ and temperatures $T_1 \neq 0$ K and $T_2 = 0$ K, we obtain for the power received by dipole 2

$$\mathcal{P}_{1\to 2} = 3\int_0^\infty \frac{d\omega}{2\pi}\hbar\omega n_1\mathcal{T}_{21}. \tag{63}$$

The transmission coefficient $\mathcal{T}_{12}$ can be expressed as

$$\mathcal{T}_{21} = \tfrac{4}{3}k_0^4\mathrm{Im}\mathrm{Tr}[\mathbb{D}^{-1}\mathbb{G}_{21}\underline{\underline{\chi}}_1(\mathbb{D}^{-1}\mathbb{G}_{21})^\dagger\underline{\underline{\tilde{\chi}}}_2], \tag{64}$$

with $\mathbb{D} = \mathbb{1} + k_0^4\mathbb{G}_{21}\underline{\underline{\alpha}}_1\mathbb{G}_{12}\underline{\underline{\alpha}}_2$ introducing the generalized susceptibility

$$\underline{\underline{\tilde{\chi}}}_2 = \frac{\underline{\underline{\alpha}}_2 - \underline{\underline{\alpha}}_2^\dagger}{2i} - k_0^2\underline{\underline{\alpha}}_2^\dagger\frac{\mathbb{G}_{22} - \mathbb{G}_{22}^\dagger}{2i}\underline{\underline{\alpha}}_2. \tag{65}$$

Note that this general susceptibility differs only slightly from Eq. (53), whereas for isotropic dipoles the two definitions coincide. This is the most general expression of the transmission coefficient for two dipolar objects in a given environment of any shape. The appearance of the terms $\mathbb{D}^{-1}$ in the transmission coefficient are due to multiple interactions between the dipoles. Therefore, the hybridization of any localized dipole resonance due to the strong coupling for small distances is accounted for in this expression. Note that Eq. (64) resembles Eq. (36) of Ekeroth, García-Martín, and Cuevas (2017), but with the slight difference that they used $\underline{\underline{\chi}}_2$ instead of $\underline{\underline{\tilde{\chi}}}_2$. On the other hand, the form of the transmission coefficient (64) was also used by Krüger et al. (2012) and Herz and Biehs (2019) within the scattering approach of Krüger et al. (2012). However, within the range of validity of the dipole approximation the second term in $\underline{\underline{\chi}}$ or $\underline{\underline{\tilde{\chi}}}$ typically can be neglected and many researchers simply use

$$\underline{\underline{\chi}}_i \approx \underline{\underline{\tilde{\chi}}}_i = \frac{\underline{\underline{\alpha}}_i - \underline{\underline{\alpha}}_i^\dagger}{2i}. \tag{66}$$

When adding a third dipole at $T_3 = 0$ K, we still can use Eqs. (63) and (64) to quantify the power exchanged between dipoles 1 and 2. The main difference is that $\boldsymbol{T}_{12}^{-1}$ now also contains the coupling with the third dipole. Hence, the sheer presence of the third particle changes the transmission coefficients due to the fact that it changes the mode structure, which is for dipoles with a localized resonance again due to the hybridization for three dipoles this time (see Fig. 13) responsible for the broadening of the absorption spectrum, as discussed in Sec. III.A.1. As a consequence, the presence of a third dipole changes the power exchange $\mathcal{P}_{1\to 2}$, proving that the heat exchange in an N-dipole system is nonadditive. This formalism is valid only for interparticles distances larger than $4R$, with R the radius of the particles. It can be extended to

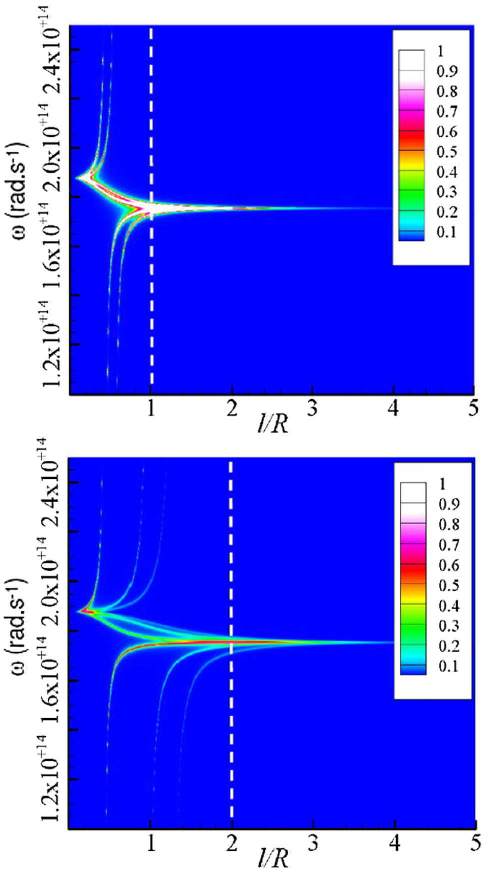

FIG. 12. Power flow exchanged between two SiC nanoparticles at $T_1 = 300$ K (red line) and at $T_2 = 0$ K (blue line) in the presence of a third SiC nanoparticle at temperature $T_3 = 0$ K (gray line) and normalized by the power exchanged between two isolated particles, i.e., $\varphi_{12}^* = \mathcal{P}_{1\to 2}(T_1, T_2, T_3)/\mathcal{P}_{1\to 2}(T_1, T_2)$. From Ben-Abdallah, Biehs, and Joulain, 2011.

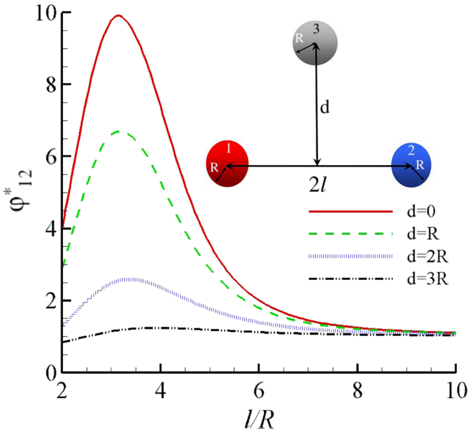

FIG. 13. Transmission coefficient $\mathcal{T}_{21}$ (a) between two SiC nanoparticles and (b) between two SiC nanoparticles in the presence of a third SiC nanoparticles as in Fig. 12 for $d = 0$. The dashed line marks the region where the particles would touch. The unphysical region beyond this line is shown to illustrate the hybridization mechanism of dipolar resonances, which can be seen in that region. From Ben-Abdallah, Biehs, and Joulain, 2011.

smaller distances by including multipolar contributions (Czapla and Narayanaswamy, 2019).

This many-body effect can be exploited to enhance the exchanged power between two dipolar objects 1 and 2 by bridging the distance via a third dipole that is placed between 1 and 2, as shown by Ben-Abdallah, Biehs, and Joulain (2011); see Fig. 12. However, keep in mind that the heat flux between two dipoles in an N-dipole system cannot be arbitrarily enhanced. As discussed by Ben-Abdallah, Biehs, and Joulain (2011), it can be easily shown that each of the conductances between two dipoles can be at most 3 times the quantum of thermal conductance. Nonetheless, this upper limit is difficult to achieve, leaving much room for optimization. Several researchers have shown that it is possible to tailor the interdipole heat flux via a third dipole or third object. Messina, Tschikin *et al.* (2013) studied the relaxation dynamics for the three-body configuration, and Dong, Zhao, and Liu (2017a) also included the possibility of having a magnetic polarizability as needed to describe metallic nanoparticles in the infrared. Furthermore, using prolate (Incardone, Emig, and Krüger, 2014; Nikbakht, 2014, 2015) or oblate (Choubdar and Nikbakht, 2016) spheroidal nanoparticles, it has been demonstrated that by changing the relative orientation of the nanoparticles and, in particular, an intermediate nanoparticle the heat flux can be switched and enhanced efficiently; see also Fig. 31. Furthermore, the coupling of two nanoparticles via the surface modes of an interface or intermediate medium has been studied, as discussed in Sec. III.C.3. Finally, the nonadditivity of the heat exchange has consequences for the transport properties in nanoparticle chains and complex nanoparticle networks, as discussed in Sec. III.C.2.

4. Application: Thermal discrete dipole approximation

The expressions for the heat exchange in systems with N dipolar objects in Eq. (58) without the contribution of the background derived by Ben-Abdallah, Biehs, and Joulain (2011) were employed first by Edalatpour and Francoeur (2014) to determine the heat exchange between macroscopic objects with isotropic and later by Ekeroth, García-Martín, and Cuevas (2017) for macroscopic objects with anisotropic and magneto-optical material properties. The idea is to replace the macroscopic objects with a large number N of small cubes of volume V_i $(i = 1, \ldots, N)$ that can be approximated as dipoles with the corresponding polarizabilities. The polarizability including the radiative corrections, as rederived by Albaladejo *et al.* (2010) and originally also used by Draine (1988), was written by Ekeroth, García-Martín, and Cuevas (2017) as

$$\underline{\underline{\alpha}}_i = \left(\mathbb{1} - i\frac{k_0^3}{6\pi}\underline{\underline{\alpha}}_{0i}\right)^{-1}\underline{\underline{\alpha}}_{0i} \tag{67}$$

in terms of the quasistatic polarizability

$$\underline{\underline{\alpha}}_{0i} = 3V_i(\varepsilon - \mathbb{1})(\varepsilon + 2\mathbb{1})^{-1}. \tag{68}$$

Note that Edalatpour and Francoeur (2014) used another expression for the dressed polarizability known as the strong form of the coupled dipole method. A detailed discussion on

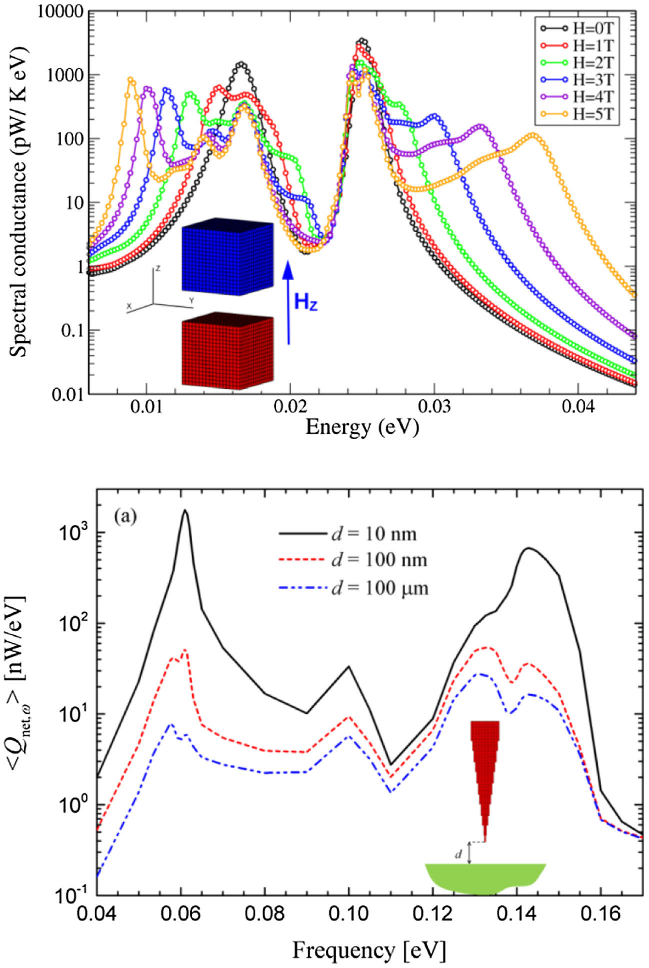

FIG. 14. (a) Spectral conductance as a function of the energy for InSb cubes with a cube side of 1 μm separated by a 500 nm gap at $T = 300$ K, and for various values of the magnetic field H applied along the z direction. Inset: discretization geometry. The number of dipoles per cube is 4913 (each one has an edge length of 59 nm). From Ekeroth, García-Martín, and Cuevas, 2017. (b) Spectral heat flux between a silica probe and a silica surface. From Edalatpour and Francoeur, 2016.

the different expressions of the dressed polarizabilities in the context of classical coupled dipole method (Purcell and Pennypacker, 1973) was given by Lakhtakia (1992).

Known as DDA, this method for describing thermal-radiation phenomena between macroscopic objects is called (Edalatpour and Francoeur, 2014) thermal discrete dipole approximation (TDDA). It has been successfully employed to determine the heat flux between macroscopic reciprocal and nonreciprocal cubes and spheres (Edalatpour and Francoeur, 2014; Edalatpour *et al.*, 2015; Ekeroth, García-Martín, and Cuevas, 2017; Ekeroth *et al.*, 2018), and also for the heat flux between a sharp conical tip and a planar substrate (Edalatpour and Francoeur, 2016), as shown in Fig. 14. In principle this method can also be used to determine the heat flux between two macroscopic objects in arbitrary many-body systems. As discussed by Edalatpour *et al.* (2015), the large number of dipolar subvolumes needed to describe macroscopic objects or have a convergent numerical result sets a certain limit on this numerical method. See also the discussion in Sec. II.F.

Finally, the TDDA method also allows one to determine the thermal emission of macroscopic objects by calculation of the mean Poynting vector from Eq. (59) in the far-field regime (Ekeroth, García-Martín, and Cuevas, 2017). This can also be done with a standard DDA by determining the absorptivity discussed in Sec. III.A.1 of the macroscopic object modeled by an assembly of dipoles and then using the Kirchhoff law to determine the emissivity. The main advantage of the TDDA is that it allows one to attribute to each volume element a given temperature. Hence, TDDA opens up the possibility of calculating thermal emission of macroscopic objects with a given temperature distribution, whereas the standard DDA can handle only emission of isothermal objects or dipolar assemblies. Note that the assumption of local thermal equilibrium sets strict bounds on the spatial variation of temperature distributions (Eckhardt, 1984).

B. Heat flux in macroscopic many-body systems

In Sec. III.A we described a formalism allowing one to account for the heat exchange in an arbitrary set of dipolar particles. As previously clarified, although formally and computationally simpler, this framework is limited in terms of distance between the particles. For this reason, in the past decade several theoretical schemes have been developed to account for the heat transfer in configurations of two or more macroscopic bodies. The purpose of these techniques is to address bodies with in principle arbitrary geometry and optical properties. As we saw in Secs. II.E and II.F, several techniques have been introduced to successfully treat this problem. We focus here on scattering-matrix techniques, where each macroscopic body is described in terms of its scattering operators, accounting for its response to an incoming electromagnetic field.

1. Scattering-matrix formalism

Two closely related formalisms based on this approach were introduced between 2009 and 2011 by Bimonte (2009), Krüger, Emig, and Kardar (2011) and Krüger *et al.* (2012), and Messina and Antezza (2011a, 2011b). The main difference between the these works is that Krüger *et al.* derived expressions that are suitable to any choice of basis for the electromagnetic field, while Messina and Antezza explicitly used a plane-wave basis, thus providing more explicit (albeit less general) expressions in terms of the individual scattering operators. To define these operators, the electric field in any region of the system is decomposed in plane waves as

$$\mathbf{E}^{\phi}(\mathbf{r},t) = 2\mathrm{Re}\Bigg[\sum_{p}\int_{0}^{+\infty}\frac{d\omega}{2\pi}\int\frac{d^{2}\boldsymbol{\kappa}}{(2\pi)^{2}}\exp[i\mathbf{k}^{\phi}\cdot\mathbf{r}] \times \exp[-i\omega t]\hat{\epsilon}_{p}^{\phi}(\boldsymbol{\kappa},\omega)E_{p}^{\phi}(\boldsymbol{\kappa},\omega)\Bigg], \qquad (69)$$

where ω is the frequency, $\boldsymbol{\kappa} = (k_x, k_y)$ is the projection of the wave vector on the x-y plane, p is the polarization index taking values 1 (transverse electric) and 2 (transverse magnetic), and ϕ is the propagation direction along the z axis.

Moreover, $\mathbf{k}^\phi = (\boldsymbol{\kappa}, \phi k_z)$ is the full wave vector, while the unit polarization vectors are defined as follows:

$$\hat{\epsilon}^\phi_{\mathrm{TE}}(\boldsymbol{\kappa},\omega) = \hat{\mathbf{z}} \times \hat{\boldsymbol{\kappa}} = \frac{1}{\kappa}(-k_y\hat{\mathbf{x}} + k_x\hat{\mathbf{y}}),$$
$$\hat{\epsilon}^\phi_{\mathrm{TM}}(\boldsymbol{\kappa},\omega) = \frac{c}{\omega}(-\kappa\hat{\mathbf{z}} + \phi k_z\hat{\boldsymbol{\kappa}}). \tag{70}$$

Each body is described in terms of four scattering operators $\mathcal{R}^\phi(\omega)$ and $\mathcal{T}^\phi(\omega)$ ($\phi = +,-$), connecting the amplitudes $E^\phi_p(\boldsymbol{\kappa},\omega)$ of the incoming and scattered fields as (suppressing the frequency arguments)

$$E^{(\mathrm{re})\phi}_p(\boldsymbol{\kappa}) = \sum_{p'}\int\frac{d^2\boldsymbol{\kappa}'}{(2\pi)^2}\langle p,\boldsymbol{\kappa}|\mathcal{R}^\phi|p',\boldsymbol{\kappa}'\rangle E^{(\mathrm{in})-\phi}_{p'}(\boldsymbol{\kappa}'),$$
$$E^{(\mathrm{tr})\phi}_p(\boldsymbol{\kappa}) = \sum_{p'}\int\frac{d^2\boldsymbol{\kappa}'}{(2\pi)^2}\langle p,\boldsymbol{\kappa}|\mathcal{T}^\phi|p',\boldsymbol{\kappa}'\rangle E^{(\mathrm{in})\phi}_{p'}(\boldsymbol{\kappa}'), \tag{71}$$

where each mode $(\omega, \boldsymbol{\kappa}, p)$ of the scattered field has in general components from each mode $(\omega, \boldsymbol{\kappa}', p')$ of the incoming field, with the frequency ω conserved since we are addressing only stationary processes. The action of these operators is schematically represented in Fig. 15.

At this stage, we sketch the main steps and assumptions leading to the expression of the radiative heat flux on each body, which can be summarized as follows:

(1) The fields generated by the fluctuating charges inside each body are identified as the source fields, along with the environmental field in which the system is embedded.
(2) The correlation functions of the individual source fields are deduced from the assumption of local thermal equilibrium.
(3) The total field in each region is explicitly written, in terms of the source fields, as a result of the scattering reflection and transmission processes occurring due to the presence of the bodies.
(4) The correlation functions of the total field in each region can be deduced.
(5) These are used for the calculation of the average value of the Poynting vector.

We stress that in (2) the assumption of local thermal equilibrium is equivalent to stating that the statistical properties of the field emitted by each body are the same as we would have if the body were at thermal equilibrium at its own temperature. Details about the derivation of such correlation functions were given by Messina and Antezza (2011b). This step leads to a source correlation function equivalent to Eq. (52) that was already seen in the case of dipoles, with the difference that in this case the scattering operator, accounting for the geometric and optical properties of the body, explicitly appear.

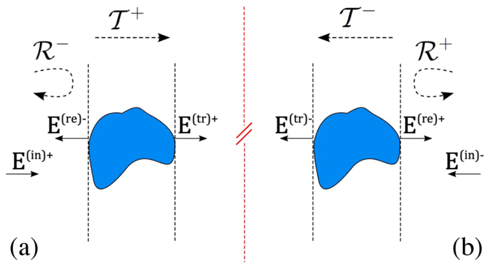

FIG. 15. Definition of reflection and transmission operators associated with an individual body. From Messina and Antezza, 2011b.

These steps allow us to explicitly write the power absorbed by each body i under the form

$$\mathcal{P}_i = \mathrm{Tr}\left[\hbar\omega\left(\sum_{j\neq i}(n_j - n_i)\mathcal{T}_{ij} + (n_b - n_i)\mathcal{T}_{ib}\right)\right], \tag{72}$$

which is analogous to Eq. (56), already encountered in the dipolar case, where the trace operator is defined as

$$\mathrm{Tr}\mathcal{A} = \sum_p\int\frac{d^2\boldsymbol{\kappa}}{(2\pi)^2}\int_0^{+\infty}\frac{d\omega}{2\pi}\langle p,\boldsymbol{\kappa}|\mathcal{A}|p,\boldsymbol{\kappa}\rangle. \tag{73}$$

We focus here on the contribution to the heat flux on body 1 associated with the presence of body 2. The corresponding transmission coefficient $\mathcal{T}_{12}$ reads

$$\mathcal{T}_{12} = U^{(2,1)}\chi_2 U^{(2,1)\dagger}\tilde{\chi}_1, \tag{74}$$

where $U^{(2,1)} = (1 - \mathcal{R}^{(2)-}\mathcal{R}^{(1)+})^{-1}$ is the operator describing the infinite series of reflections inside the cavity formed by bodies 1 and 2 and the generalized susceptibilities are defined as

$$\chi_2 = f_{-1}(\mathcal{R}^{(2)-}) - \mathcal{T}^{(2)-}P^{(\mathrm{pw})}_{-1}\mathcal{T}^{(2)-\dagger}, \tag{75}$$

$$\tilde{\chi}_1 = f_1(\mathcal{R}^{(1)+}) - \mathcal{T}^{(1)-\dagger}\mathcal{P}^{(\mathrm{pw})}_1\mathcal{T}^{(1)-}, \tag{76}$$

by means of the auxiliary functions

$$f_\alpha(\mathcal{R}) = \begin{cases}\mathcal{P}^{(\mathrm{pw})}_{-1} - \mathcal{R}\mathcal{P}^{(\mathrm{pw})}_{-1}\mathcal{R}^\dagger + \mathcal{R}\mathcal{P}^{(\mathrm{ew})}_{-1} - \mathcal{P}^{(\mathrm{ew})}_{-1}\mathcal{R}^\dagger, & \alpha = -1,\\ \mathcal{P}^{(\mathrm{pw})}_1 - \mathcal{R}^\dagger\mathcal{P}^{(\mathrm{pw})}_1\mathcal{R} + \mathcal{R}^\dagger\mathcal{P}^{(\mathrm{ew})}_1 s - \mathcal{P}^{(\mathrm{ew})}_1\mathcal{R}, & \alpha = 1.\end{cases} \tag{77}$$

The operators $\mathcal{P}^{(\mathrm{pw})}_n$ and $\mathcal{P}^{(\mathrm{ew})}_n$ are defined (for any integer n) as

$$\langle p,\boldsymbol{\kappa}|\mathcal{P}^{(\mathrm{pw/ew})}_n|p',\boldsymbol{\kappa}'\rangle = k_z^n\langle p,\boldsymbol{\kappa}|\Pi^{(\mathrm{pw/ew})}|p',\boldsymbol{\kappa}'\rangle, \tag{78}$$

where $\Pi^{(\mathrm{pw})} = \Theta(\omega - ck)$ and $\Pi^{(\mathrm{ew})} = \Theta(ck - \omega)$ are the projectors on the propagative and evanescent sectors, respectively. The transmission coefficient $\mathcal{T}_{12}$ has the same form as in Eq. (64) for two dipolar objects. By choosing the T operator for dipolar objects or using the plane-wave expansion of the T operators, both forms of transmission coefficients can be obtained from the general T-operator expression given by Krüger *et al.* (2012) and Herz and Biehs (2019).

This approach was later generalized to the case of three arbitrary bodies (Messina and Antezza, 2014). The Landauer-like expression (72) of the power absorbed by each body remains valid, meaning that the flux on body 1 has contributions coming from bodies 2 and 3, as well as from the environment. We now investigate the expression of the transmission coefficient $\mathcal{T}_{12}$ between bodies 1 and 2 in this three-body configuration. It reads

$$\mathcal{T}_{12} = U^{(23,1)}[f_{-1}(\mathcal{R}^{(23)-}) - \mathcal{T}^{(2)-}U^{(3,2)}f_{-1}(\mathcal{R}^{(3)-}) \\ \times U^{(3,2)\dagger}\mathcal{T}^{(2)-\dagger}]U^{(23,1)\dagger}\tilde{\chi}_1, \tag{79}$$

in which a two-body reflection operator (and the associated multireflection operator $U^{(23,1)}$) appears, defined as

$$\mathcal{R}^{(23)-} = \mathcal{R}^{(2)-} + \mathcal{T}^{(2)-}U^{(3,2)}\mathcal{R}^{(3)-}\mathcal{T}^{(2)+}. \tag{80}$$

We immediately see that Eqs. (74) and (79) are different. The important message behind this comparison is that, as for the dipolar case discussed in Sec. III.A.3, the presence of body 3 not only introduces an additional source for the energy transfer on body 1 but also modifies the transmission coefficient $\mathcal{T}_{12}$, and consequently the way bodies 1 and 2 exchange heat. In other words, the third body in the system acts both as a source or sink of radiation and as a scatterer (independently of its temperature), modifying the transmission amplitudes of other channels. We conclude that Eq. (79) is by itself a proof and a quantitative evaluation of the nonadditive nature of RHT, in the simplest possible many-body system made of three bodies.

The same approach described in Sec. III.B and applied to both two- and three-body systems was generalized some years later to the case of N bodies (Latella *et al.*, 2017). In this case, for simplicity only planar bodies, i.e., parallel slabs of finite thickness separated by vacuum gaps, have been considered. This assumption has two main advantages: first, the plane-wave development is particularly convenient for this configuration since it fully suits its symmetry; moreover the translational invariance along the transverse coordinates makes all the scattering operators diagonal with respect to both p and $\boldsymbol{\kappa}$, significantly simplifying all the expressions. We stress that, since we are dealing here with infinite systems, the power on each body has to be replaced with the heat flux Φ that it receives (power per unit surface).

2. Nonadditivity in many-body systems

In Sec. III.B.1, we analytically showed the nonadditivity of RHT. In the simplest case of three bodies, the appearance of the third one modifies the transmission amplitude $\mathcal{T}_{12}$, namely, the way in which bodies 1 and 2 exchange energy. This is shown by the comparison of Eqs. (74) and (79). In addition to making this formal comparison, we can quantitatively address the modification to the energy flux between bodies 1 and 2 due to the introduction of a third body in the system. This analysis has been performed analogous to the configuration discussed in Sec. III.A.3 by Müller *et al.* (2017), where they generalize the formalism developed by Krüger *et al.* (2012), which was already valid in the scenario of N bodies, to the case of the presence of a nonabsorbing background medium. In this work, Müller *et al.* (2017) applied their formalism to the calculation of RHT between two SiC planar slabs (bodies 1 and 2) separated by a vacuum gap of thickness d, when a pointlike particle or atom of polarizability α (assumed to be nondispersive and real) is placed between them at distance d_1 from body 1. The system is depicted in Fig. 16.

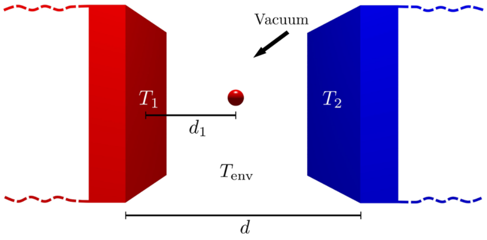

FIG. 16. Two planar slabs (bodies 1 and 2) are placed at distance d and separated by vacuum. A particle of polarizability α is placed at distance d_1 from slab 1. From Müller *et al.*, 2017.

The heat flux is evaluated after linearizing the general expressions with respect to the particle polarizability while assuming that the scattering contribution is weak. As a result, the heat flux Φ (power $\mathcal{P}$ per unit area) is expressed as

$$\Phi = \Phi_{\rm vac} + \Delta\Phi, \tag{81}$$

where $\Phi_{\rm vac}$ is the well-known heat flux between two slabs separated by a vacuum gap, and the correction term $\Delta\Phi$ (proportional to α in the linearized approximation) is a direct description of the nonadditivity of radiative heat flux.

The nonadditive correction is numerically evaluated for slab temperatures of 301 and 300 K in two different configurations: for a slab-slab distance $d = 10$ nm (near field) and for $d = 10\ \mu$m (far field), as a function of the particle position d_1; see Fig. 16. The results are shown in Fig. 17. In both configurations we observe the expected symmetry with respect to the central particle position $d_1 = d/2$. In the near field, we observe that the effect is maximized when the atom is close to one of the two slabs. This reflects, apart from the symmetry of the system, the typical exponentially decreasing behavior of heat flux in the near field, which is in turn a consequence of the dominating contribution of the evanescent waves. The situation is different in the far field. The effect is several orders of magnitude smaller that in the near field. Moreover, the external positions $d = 0, d_1$ are now minima of the effect, which oscillates with respect to d_1. These oscillations are due to the interferences between propagating waves (dominating in this scenario), reflected between the two plates and scattered by the particle inside the cavity, which change the local density of states (Dorofeyev, Fuchs, and Jersch, 2002; Francoeur, Mengüç, and Vaillon, 2010b) at the particle's position, which is also known from the context of spontaneous emission of atoms and molecules within such a configuration (Danz *et al.*, 2002).

Another consequence of three-body effects in NFRHT was discussed by Zheng and Xuan (2011) and Messina, Antezza, and Ben-Abdallah (2012). They considered a system made of three parallel slabs, as shown in the inset of Fig. 18. The intermediate slab, of thickness δ, is placed at distance d from the external slabs, which are assumed to have infinite thickness. This configuration is compared to the standard two-body

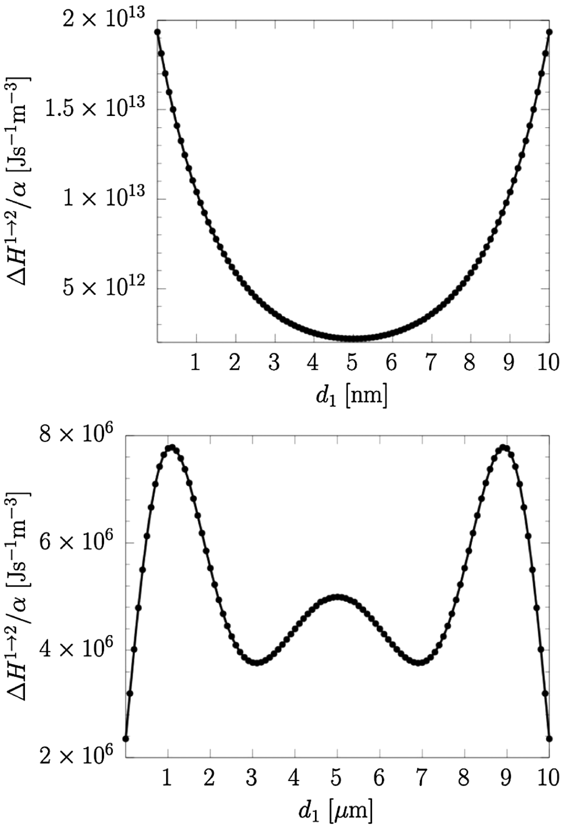

FIG. 17. Nonadditive correction to the two-body heat flux $\Delta H^{1\to 2} = \Delta\Phi$ [see Eq. (81)] in the presence of an atomic, i.e., pointlike, particle of polarizability α. The upper curve corresponds to the near-field configuration $d = 10$ nm, while the lower curve corresponds to the far field ($d = 10\ \mu$m). From Müller *et al.*, 2017.

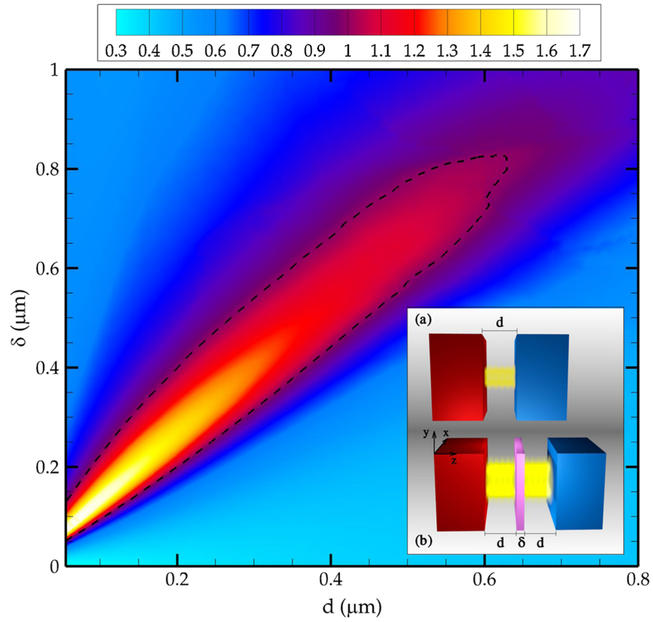

FIG. 18. Heat-flux amplification $\Phi_{3s}(d,\delta)/\Phi_{2s}(d)$ in a three-body configuration compared to a two-body configuration shown in the inset as a function of distance d and thickness of the intermediate slab δ. The black dashed line corresponds to the constant value $\Phi_{3s}(d,\delta)/\Phi_{2s}(d) = 1$. From Messina, Antezza, and Ben-Abdallah, 2012.

scenario, shown in the inset of Fig. 18, where the intermediate slab is removed and d is now the distance between the external slabs. We stress that in both systems the minimum distance between adjacent slabs, a relevant parameter in a near-field configuration, is the same. Moreover, for a chosen couple of temperatures (specifically, 400 and 300 K), the temperature of the intermediate slab is taken as the equilibrium one, i.e., the one at which the net flux on it vanishes. Based on this assumption, adding the third intermediate slab has no impact on the energy balance of the system, and thus the third body is acting only as a passive relay added to the two-body system. The heat-flux amplification, defined as the ratio $\Phi_{3s}(d,\delta)/\Phi_{2s}(d)$ between the three- and two-body fluxes, is shown in Fig. 18. The figure shows that the flux can be amplified for reasonable values (hundreds of nanometers) of both d and δ, and that this amplification factor goes up to a maximum value of around 70% for small distances. This amplification for $d \approx \delta$ is reminiscent of the superlens effect (Pendry, 2000; Biehs, Menon, and Agarwal, 2016), which leads to an optimal energy transfer between two atoms that are separated by a superlens if the distance d to the interface of the superlens coincides with the thickness of the superlens δ. Here it is a purely three-body effect, which is confirmed by the spectral and mode analysis performed by Messina, Antezza, and Ben-Abdallah (2012). More recently patterned intermediate media (Kan, Zhao, and Zhang, 2019), two-dimensional atomic systems (Simchi, 2017), and hyperbolic media (Song *et al.*, 2018) have also been considered to enhance the transfers. The use of such three-body control of heat flux was proposed to design many-body heat engines (Latella *et al.*, 2015), with thermodynamic performances better than their two-body counterpart and the thermal analog of the transistor (Ben-Abdallah and Biehs, 2014) driven by photons. In the proposed scheme, the combination of many-body effects and the presence of a phase-change material playing the role of the *gate* or *base* of the transistor allow one to switch, amplify, and modulate the heat flux between the *source* or *emitter* and the *drain* or *collector*; see also Fig. 32.

The role of a third thermally interacting body can also be played by a thermal bath, described as a body far from the rest of the system and emitting as a blackbody surface at a given temperature. This was recently shown by Latella *et al.* (2020), where the heat flux between two planar slabs or between a slab and a particle was considered in the presence of a thermal bath. It was shown that, in virtue of many-body interactions taking place in these three-body systems, the flux exchanged between the two slabs (or the slab and the particle) saturates to a constant value when the distance goes to zero even at a relatively large separation distance where the nonlocal optical effects are negligible, as shown in Fig. 19 for the case of two SiC slabs.

3. Steady-state temperatures and multistable states

In arbitrary many-body systems consisting of N objects at temperatures $T_1, \ldots, T_N$ the time evolution reads ($i = 1, \ldots, N$)

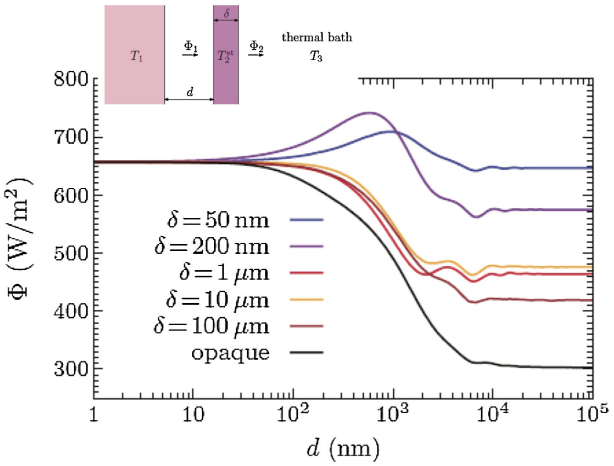

FIG. 19. Heat flux exchanged between two slabs immersed in a thermal bath with respect to their separation distance d. Slab 1 has a fixed temperature of $T_1 = 400$ K, while the thermal bath is at $T_3 = 300$ K. The second slab, of thickness δ, thermalizes to the equilibrium temperature at which the net flux it receives vanishes. From Latella *et al.*, 2020.

$$I_i \frac{dT_i}{dt} = \mathcal{P}_i(T_1, \ldots, T_N; t), \tag{82}$$

where $I_1 = \rho_i C_i V_i$ is the termal inertia defined by the heat capacity per unit mass C_i, the volume V_i, and the mass density ρ_i of object i, while $\mathcal{P}_i$ is the net power received by this object. Following expressions in Eqs. (72) and (56) the latter can be broken into

$$\mathcal{P}_i(T_1, \ldots, T_N; t) = \sum_{j \neq i} \mathcal{P}_{ij}(T_1, \ldots, T_N; t) + \mathcal{P}_{ib}(t), \tag{83}$$

where $\mathcal{P}_{ij}$ is the power exchanged between objects j and i and $\mathcal{P}_{ib}$ is the power exchanged between object i and the background, which can also be an external heat bath or thermostat connected to object i. If all $\mathcal{P}_i$ are linear functions of the temperatures, which is generally the case close to the global equilibrium or nonequilibrium steady state (in the following, for notation simplicity we use the abreviation T^{eq} for the steady-state temperatures), i.e., for small temperature differences $|T_i - T_j| \ll \min(T_1, \ldots, T_N)$, the system of equations can be linearized by introducing the conductances

$$G_{ij} = \frac{\partial \mathcal{P}_{ij}}{\partial T_j}. \tag{84}$$

For multilayer systems with infinitely large interfaces Eqs. (82)–(84) can be used as well by simply replacing the quantities by the corresponding quantities normalized to a surface area A so that the thermal inertia becomes the thermal inertial per area $I_i \to I_i/A$, the dissipated power becomes the heat flux $\mathcal{P}_i \to \mathcal{P}_i/A \equiv \Phi_i$, and the conductance becomes the heat-transfer coefficient $G_{ij} \to G_{ij}/A \equiv H_{ij}$.

When assuming that no energy is added to or removed from outside of the system, the thermal steady state is a solution of the system of equations $(i = 1, \ldots, N)$

$$\mathcal{P}_i(T_1, \ldots, T_N) = 0. \tag{85}$$

The local thermal equilibrium of object i is reached when $\mathcal{P}_i(T_1, \ldots, T_N) = 0$. This equation defines a hypersurface in temperature space. The intersection of the hypersurfaces associated with all local equilibria defines the global steady state of the system. In the specific case where the system is composed of two objects, the local equilibrium state of each object corresponds to a curve in the two-dimensional space of temperatures (T_1, T_2), and the intersection of the two local equilibrium lines defines the global steady-state temperatures.

If all $\mathcal{P}_i$ are linear functions of the temperatures, which is generally the case close to the global equilibrium or steady state and when the conductances G_{ij} can be considered as independent of the temperatures, i.e., when, in particular, the material properties can be considered as temperature independent, the system has a unique solution $(T_1^{\mathrm{eq}}, \ldots, T_N^{\mathrm{eq}})^t$. Conversely, when the optical properties of materials are temperature dependent $\mathcal{P}_i$ become nonlinear with respect to the temperatures. In this case, the system of equations (85) might admit more than one steady-state solution. Among these temperature solutions one finds in general stable and unstable solutions. The stability of these temperatures can be assessed by following a perturbative approach. Starting from a steady state α with temperature $(T_{1,\alpha}^{\mathrm{eq}}, \ldots, T_{N,\alpha}^{\mathrm{eq}})^t$ and adding a small perturbation then the dynamics is described by the following linearized system:

$$\frac{d}{dt} \begin{pmatrix} \delta T_{1,\alpha}(t) \\ \vdots \\ \delta T_{N,\alpha}(t) \end{pmatrix} = \mathbb{J} \begin{pmatrix} \delta T_{1,\alpha}(t) \\ \vdots \\ \delta T_{N,\alpha}(t) \end{pmatrix}, \tag{86}$$

where $\delta T_{i,\alpha}(t) = T_i - T_{i,\alpha}^{\mathrm{eq}}$ $(i = 1, \ldots, N)$ is the perturbation from the steady state α and

$$\mathbb{J} = \begin{pmatrix} \frac{\partial \mathcal{P}_1}{\partial T_1} & \cdots & \frac{\partial \mathcal{P}_1}{\partial T_N} \\ \vdots & & \vdots \\ \frac{\partial \mathcal{P}_N}{\partial T_1} & \cdots & \frac{\partial \mathcal{P}_N}{\partial T_N} \end{pmatrix} \tag{87}$$

is the Jacobian matrix associated with the dynamical system (82). As in any linear dynamical system the sign of the eigenvalues of $\mathbb{J}$ allows us to draw a conclusion on the stability of the thermal state.

The demonstration of multistable thermal behaviors in many-body systems shown in Fig. 20 has opened the possibility of designing thermal analogs of volatile electronic memories (Kubytskyi, Biehs, and Ben-Abdallah, 2014; Ben-Abdallah and Biehs, 2015, 2017; Dyakov *et al.*, 2015b; Khandekar and Rodriguez, 2017), logic gates (Ben-Abdallah and Biehs, 2016; Kathmann *et al.*, 2020) (see Fig. 21), and self-oscillating systems (Dyakov *et al.*, 2015a) that allow one to switch from one global equilibrium to another and that can potentially be interesting for a practical realization of heat engines (Latella *et al.*, 2014, 2015).

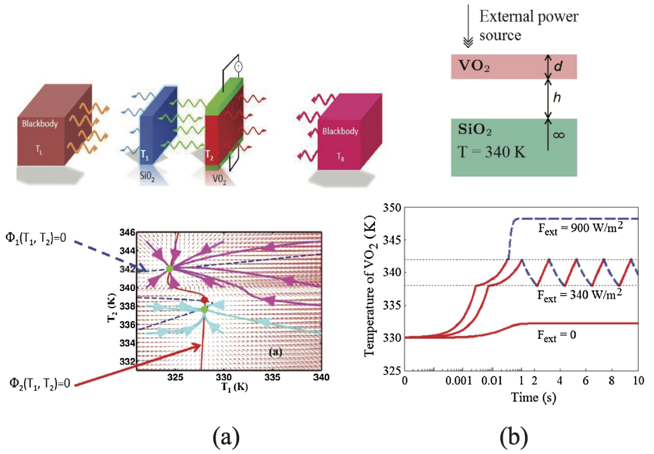

(a) (b)

FIG. 20. (a) Phase portrait (i.e., trajectories of temperatures) in a bistable system consisting of two membranes of SiO_2 and VO_2 in interaction with two thermal baths for different initial conditions. The green (red) points denote the stable (unstable) global steady-state temperatures. From Kubytskyi, Biehs, and Ben-Abdallah, 2014. (b) Self-oscillation of the temperature of a VO_2 membrane in the vicinity of a SiO_2 substrate when adding a specific external constant power F_{ext}. From Dyakov *et al.*, 2015a.

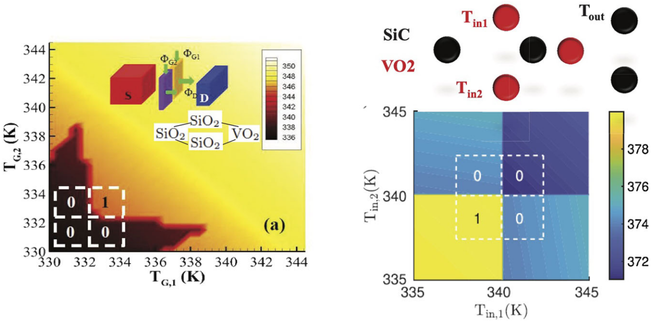

Inputs		Output
T_{G1}	T_{G2}	T_D
$T_{G1}<T_1 \leftrightarrow 0$	$T_{G2}<T_1 \leftrightarrow 0$	$T_D<T_{min} \leftrightarrow 0$
$T_{G1}<T_1 \leftrightarrow 0$	$T_{G2}>T_1 \leftrightarrow 1$	$T_D<T_{min} \leftrightarrow 0$
$T_{G1}>T_1 \leftrightarrow 1$	$T_{G2}<T_1 \leftrightarrow 0$	$T_D<T_{min} \leftrightarrow 0$
$T_{G1}>T_1 \leftrightarrow 1$	$T_{G2}>T_1 \leftrightarrow 1$	$T_D>T_{max} \leftrightarrow 1$

AND gate

T_{in1}	T_{in2}	T_{out}
0	0	1
0	1	0
1	0	0
1	1	0

NOR gate

FIG. 21. Left panels: AND gate made with two SiO_2 membranes (gates) suspended between a thermal SiO_2 source and a VO_2 drain. The color map represents the output temperature T_D of the drain with respect to the two input temperatures T_{G1} and T_{G2} of the two gates. At the bottom is the truth table for the AND gate. From Ben-Abdallah and Biehs, 2016. Right panels: NOR gate designed using a coupling of SiC and $V0_2$ nanoparticles. From Kathmann *et al.*, 2020.

C. Heat transport and heat-flux dynamics

In the 2000s the first attempts at treating heat transfer in N-body systems were made in order to quantify the contribution of plasmonic modes to the thermal conductance in one-dimensional arrays of nanoparticles in nanofluids (Ben-Abdallah, 2006; Ben-Abdallah *et al.*, 2008). Inside these simple networks (Fig. 22) all inner nanoparticles are assumed to be at zero temperature, while the two particles at either end of the chain are connected to two thermostats. In these systems heat carried by photons is simply scattered between the two thermostats. But in contrast to Polder and van Hove's theoretical framework, which is based on the FE theory, in these works a kinetic approach has been followed. The main features and limitations of this approach are discussed in Sec. III.C.1.

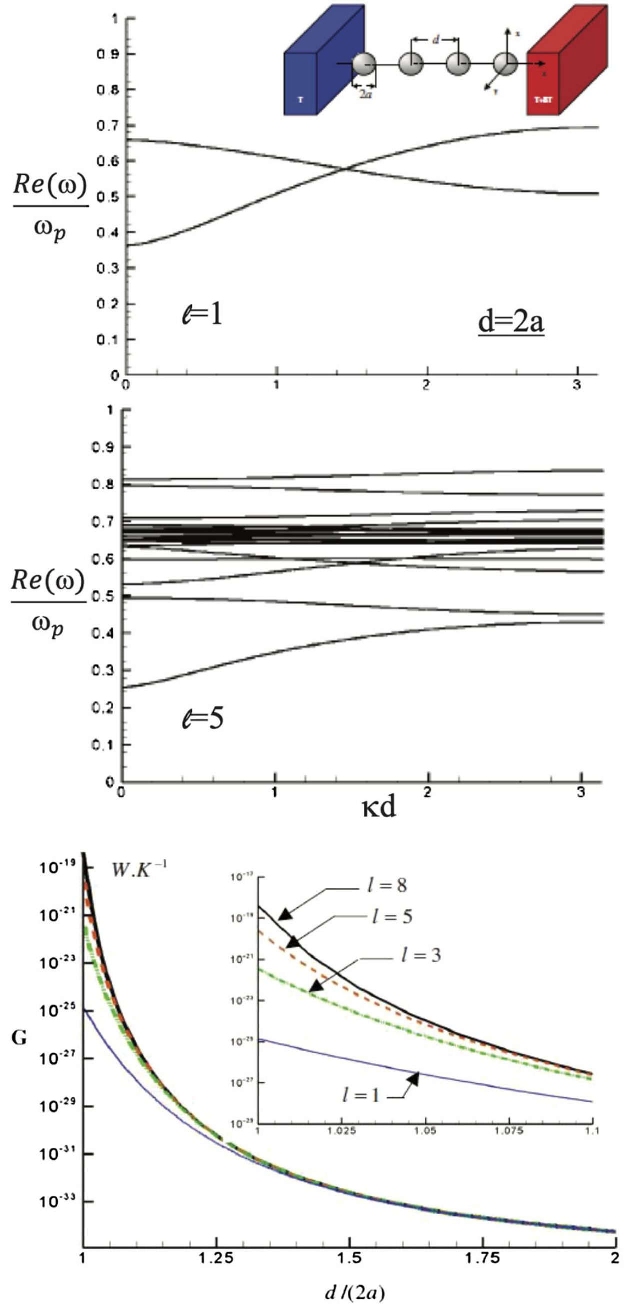

FIG. 22. Top panels: dispersion curves (real part) of collective plasmonic modes along a chain of copper nanoparticles (10 nm radius) dispersed in vacuum in the case of dipolar moments ($\ell = 1$), and for the multipolar moments of order $\ell = 5$. Bottom panel: thermal conductance G of linear chains of copper particles calculated from the kinetic theory for different multipole orders ℓ vs the separation distance d normalized to the particle diameter $2a$. Inset: enlargement of the near-contact region. From Ben-Abdallah *et al.*, 2008.

1. Kinetic approach versus exact calculations

This approximate theory is based on the solution of a Boltzmann transport equation

$$\frac{\partial f}{\partial t} + v_g(k)\frac{\partial f}{\partial z} = \left[\frac{\partial f}{\partial t}\right]_{\text{coll}} \tag{88}$$

for the distribution function f of thermal photons inside a given system. Here $v_g(k)$ is the group velocity of the mode k and the rhs of the equation stands for the collision term, which can be simplified within the relaxation time approximation. When assuming that one thermostat is at temperature T and the other one at zero temperature, the power $\mathcal{P}$ flowing through this system results from the calculation of first-order moment associated with the photonic equilibrium distribution function $f = n(\omega, T)$ (Dye-Zone, Narayanaswamy, and Chen, 2005; Ben-Abdallah *et al.*, 2008),

$$\mathcal{P} = \sum_{\ell=1}^{\infty} \int_0^{\infty} \frac{dk}{2\pi} \hbar\omega_\ell(k) v_{g,\ell}(k) n(\omega_\ell(k), T), \tag{89}$$

where $\omega_\ell(k)$ is the dispersion relation of resonant multipole modes ℓ supported by the structure. The conductance is then defined as $G = \partial\mathcal{P}/\partial T$. Note that only the eigenstates of the system are assumed to play a role in the heat transport process. Since these preliminary studies, more complex systems like chains of ellipsoidal polaritonic particles (Ordonez-Miranda *et al.*, 2015), nanoparticle crystals (Ordonez-Miranda *et al.*, 2016; Tervo *et al.*, 2016), nanoresonator inclusions (Tervo, Gustafson *et al.*, 2019), and chains of graphene disks (Ramirez and McGaughey, 2017) have been investigated using this kinetic approach (see Fig. 23), as have multilayer photonic crystals (Lau *et al.*, 2008; Lau, Shen, and Fan, 2009). But, as shown recently within a full FE calculation based on the N-body theory introduced in Sec. III.A.2, the kinetic approach fails in describing heat exchanges in systems where heat is also carried by nonresonant modes over a broad spectral band (Kathmann *et al.*, 2018). This result was recently confirmed (Tervo, Cola, and Zhang, 2020). Further studies of conductance within two- and three-dimensional dipolar systems based on the fluctational electrodynamic calculations were recently published (Tervo, Francoeur *et al.*, 2019), which opens the possibility of testing the validity of the kinetic approach in systems such as those studied by Ordonez-Miranda *et al.* (2016) and Tervo *et al.* (2016). A discussion of the conductance within multilayer photonic crystals within the FE approach on the role of surface phonon polaritons was conducted by Narayanaswamy and Chen (2005) and Tschikin, Ben-Abdallah, and Biehs (2012).

2. Heat transfer in complex networks

Based on the FE approach we now address the heat flux in arbitrary systems. The thermal behavior of fractal structures and the heat exchanges between fractal clusters of nanoparticles has also been theoretically investigated. These studies have revealed (Dong, Zhao, and Liu, 2017b; Nikbakht, 2017) that the (self-)conductance increases as R^{D_f}, where R is the gyration radius of the structure and D_f is its fractal dimension; see Fig. 24(a). When two of these structures interact in near field the thermal conductance of the heat exchange between metallic clusters increases with the fractal dimension, as can be seen in Fig. 24(b). Moreover, in contrast to ordered media, the localization of plasmons or phonon-polaritons in fractal structures could be responsible for a significant reduction of the self-conductance in fractal structures, although no clear evidence about this claim has been presented thus far. However, a recent study (Luo *et al.*, 2019) revealed that the heat transfer between fractal structures does not depend on their fractality at a separation distance larger than the localization lengths, which tends to confirm this statement.

In addition to their original thermal properties several physical effect inherent to many-body systems have been highlighted in complex plasmonic structures. Among these

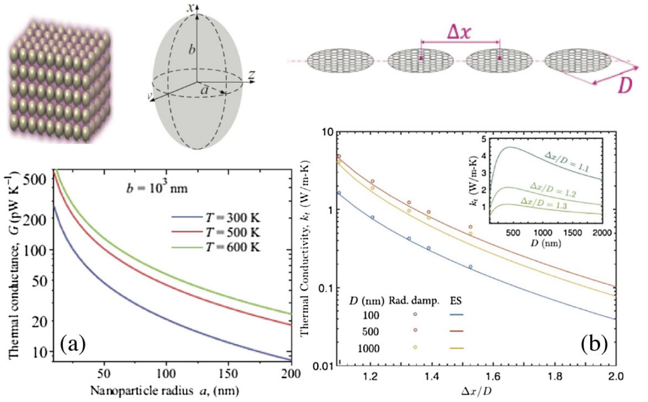

FIG. 23. (a) Thermal conductance of colloidal crystals made up of spheroidal SiC nanoparticles as a function of their horizontal radius. (b) Thermal conductivity of coplanar disk arrays for different diameters and separations at temperature $T = 300$ K. From Ordonez-Miranda *et al.*, 2016, and Ramirez and McGaughey, 2017.

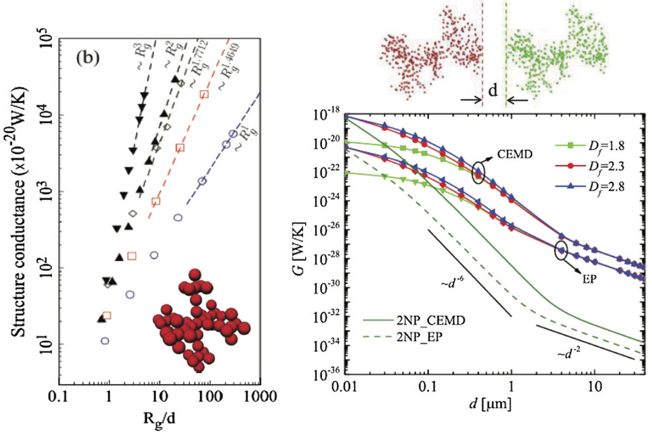

(a) (b)

FIG. 24. (a) Thermal conductance of Vicsek fractal structures as a function of the normalized gyration radius. From Nikbakht, 2017. (b) Thermal conductance between two Ag nanoparticle clusters at various fractal dimensions. From Luo *et al.*, 2019.

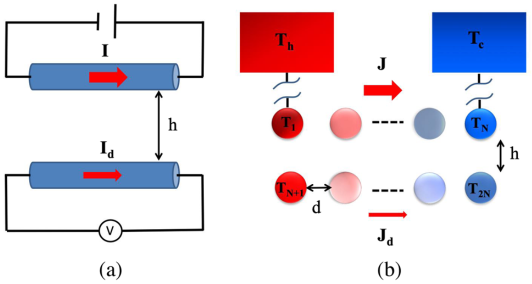

FIG. 25. (a) Illustration of the classical Coulomb drag effect. A drag electric current I_d in a passive conducting wire is induced by a primary current I flowing in a driving conductor placed close by. (b) Radiative drag effect in a many-body system: a drag heat flux J_d carried by thermal photons between two particles is induced by a heat flux J exchanged between two thermostatic objects in a many-body system. From Ben-Abdallah, 2019a.

effects, a thermal analog of the Coulomb drag effect in nanoparticle networks was recently predicted theoretically (Ben-Abdallah, 2019a). The configuration is sketched in Fig. 25. As in its electric counterpart, where interactions at close separation distances (compared to the range of Coulombic interactions) of free charge carriers between two electric conductors give rise to a drag current in a passive conductor when a bias voltage is applied along the so-called drive conductor, a radiative heat flux in a many-body systems can be induced in a given region by a primary flux generated by a temperature gradient in another region of the system. In the case of two parallel chains of nanoparticles as sketched in Fig. 25(b), where the extremities of the first chain are held at fixed temperature with two external thermostats while all other particles can relax to their own local equilibrium temperature, the magnitude and the direction of drag flux can be calculated using the following procedure.

In the steady state the net power received by each particle vanishes, which allows one to determine unknown temperatures $(T_2, \dots, T_{N-1}, T_{N+1}, \dots, T_{2N})$ (T_1 and T_N are fixed by the thermostats) and the power $\mathcal{P}_1$ and $\mathcal{P}_N$ coming from the external thermostats in order to keep the temperatures of particle 1 and N fixed. Then the heat current in the upper chain in Fig. 25(b)

$$J = \mathcal{P}_N - \mathcal{P}_1 \tag{90}$$

as well as the induced heat current in the lower chain in Fig. 25(b)

$$J_D = \mathcal{P}_{2N} - \mathcal{P}_{N+1} \tag{91}$$

can be determined. Finally, the thermal drag resistance

$$R_D = \frac{T_{N+1} - T_{2N}}{J} \tag{92}$$

quantifies the frictional effect induced by the electromagnetic interactions between the different regions inside the system. In hybrid polar-metal systems this friction can be negative (Ben-Abdallah, 2019a), proving the existence of regions within these systems where heat can locally flow in the opposite direction of the applied temperature difference.

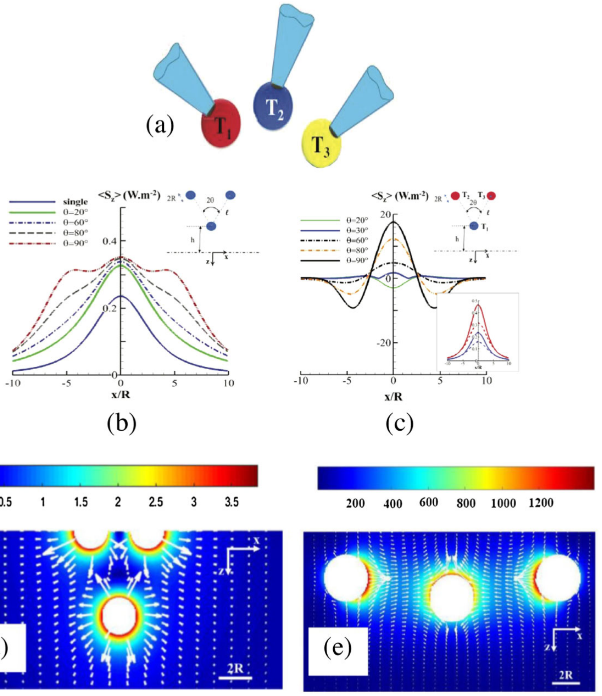

FIG. 26. (a) Schematic of a multitip SThM platform with three tips. Nanospheres (thermal emitters) are grafted on single scanning probe tips and held close to a substrate. Their temperatures and positions are individually controlled. (b) Normal component $\langle S_z \rangle$ of the Poynting vector radiated through the substrate surface at $z = 0$ by a three-tip SThM setup with glass nanoemitters at $T = 300$ K. (c) Similar to (b) but with $T_2 = T_3 = 350$ K (red curve) and $T_1 = 300$ K (blue curve). Inset: flux at $z = 0$ for a single particle at $T = 300$ K. (d),(e) Magnitude of Poynting vector field in the (x, z) plane radiated by a multitip setup in (d) for an angular opening of $\theta = 20°$ and in (e) for an angular opening $\theta = 80°$. From Ben-Abdallah, 2019b.

In addition to this generation of heat flux by the frictional effect in many-body systems, the temperature of the particles in particle networks can be individually addressed with a subwavelength accuracy (Yannopapas and Vitanov, 2013) by using external excitations such as chirped pulses and can be controlled using adaptive optimization techniques at the timescale of thermal relaxation processes. The interplay between nano-objects can also be used to focus and even pump heat (Ben-Abdallah, 2019b) outside of the system itself. The heat flux radiated through an oriented surface by a collection of emitters held at different temperatures T_i $(i = 1, \dots, N)$ can be calculated from Eq. (59). By tuning the temperature of three thermal emitters in the vicinity of a substrate as shown in Fig. 26, the heat flux can be locally focused and even amplified in small regions that are much smaller than the diffraction limit and even smaller than the regions heated with a single emitter (Ben-Abdallah, 2019b). This control of flux lines by a collection of nanosources can be used to tailor the heat flux at the nanoscale or to analyze and change the local temperature of solid surfaces at this scale.

3. Long-range heat transport and amplification of heat flux

Instead of enhancing the heat flux between two nanoparticles or two slabs by introducing an intermediate nanoparticle or slab as discussed in Secs. III.A.3 and III.B.2, it is possible to guide the radiative heat flux over a long distance by exploiting the properties of specific modes such as surface or hyperbolic modes supported by some structures. This guiding can be done by bringing two nanoparticles close to a planar interface as sketched in Fig. 27(a), which supports a surface polariton in the infrared. Then the hot nanoparticle can directly couple to this surface mode and subsequently transfer its heat to the second (cold) particle over relatively long distances.

Such a transport was first investigated by Sääskilahti, Oksanen, and Tulkki (2014) between polar nanoparticles above single polaritonic surfaces and inside cavities formed of two mirrors or made with slabs supporting surface modes. This and more recent studies (Asheichyk and Krüger, 2018; Dong, Zhao, and Liu, 2018; Messina, Biehs, and Ben-Abdallah, 2018) showed that the heat current between dipoles placed in a cavity can be enhanced by several orders of magnitude relative to the free-space heat current with a similar interparticle distance. In particular, Messina, Biehs, and Ben-Abdallah (2018) showed that a similar enhancement and long-range heat transport can be also observed between metallic particles when a graphene sheet covers a SiC interface. In this case the heat flux can be enhanced by several orders of magnitude at an interparticle distance of about 1–10 μm, as shown in Fig. 27(b), suggesting that the near-field enhanced thermal radiation can be brought to distances comparable to the thermal wavelength. Similar enhancement effects were reported for the heat flux along chains of nanoparticles close to a phonon-polaritonic interface (Dong, Zhao, and Liu, 2018), between two nanoparticles mediated by an intermediate macroscopic phonon-polaritonic sphere (Asheichyk, Müller, and Krüger, 2017), using an anisotropic metasurface made of graphene stripes (Zhang, Antezza *et al.*, 2019) or a stack of graphene sheets (He, Qi, Ren *et al.*, 2019). As shown by Ott and Biehs (2020) the distance at which the maximum heat-flux enhancement occurs is connected to the propagation length of the surface modes (Ott and Biehs, 2020). Hence, the enhancement mechanism for the heat flux is reminiscent of the enhancement of Förster resonance energy transfer between atoms, molecules, or quantum dots that are brought into close vicinity to a plasmonic interface where a maximal enhancement is also found at distances coinciding with the propagation length of the surface modes involved in the energy transport (Velizhanin and Shahbazyan, 2012; Biehs and Agarwal, 2013b; Bouchet *et al.*, 2016; Poudel, Chen, and Ratner, 2016), allowing for a long-range energy transfer.

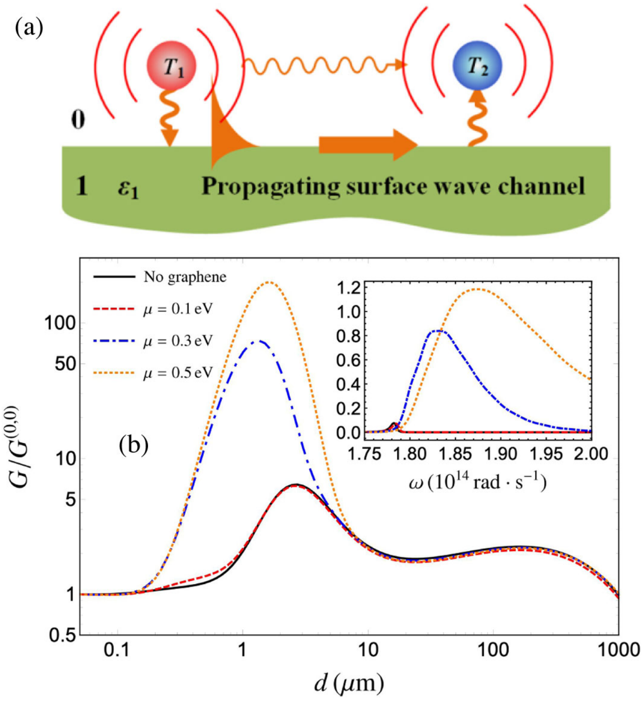

FIG. 27. (a) Heat flux between two nanoparticles at interparticle distance d using coupling via the surface modes of an interface. From Dong, Zhao, and Liu, 2018. (b) Conductance ratio $G/G^{(0,0)}$ (G conductance with interface and $G^{(0,0)}$ without interface) as a function of d between two Au nanoparticles placed at distance $z = 150$ nm from a SiC substrate. The four lines correspond to the absence of graphene (black solid line), and to configurations with graphene having $\mu = 0.1$ eV (red dashed line), 0.3 eV (blue dot-dashed line), and 0.5 eV (orange dotted line). Inset: spectral conductance associated with the four same configurations. From Messina, Biehs, and Ben-Abdallah, 2018.

Motivated by the promising properties of hyperbolic metamaterials for long-range Förster energy transfer (Biehs, Menon, and Agarwal, 2016; Deshmukh *et al.*, 2018; Newman *et al.*, 2018), another strategy has been explored to transport the near-field heat flux over long distances using such hyperbolic guides. Hence, it has been shown that the large wave vector surface waves supported by polaritonic materials can be converted into propagating hyperbolic modes inside such media, such that the usual ultrasmall penetration depth of near-field heat flux (Basu and Zhang, 2009) can become large (tens to hundreds of nanometers) (Lang *et al.*, 2014; Tschikin *et al.*, 2015; Biehs and Ben-Abdallah, 2017), as does the net amount of heat they can transport (Biehs *et al.*, 2015; Liu and Narimanov, 2015). Since the hyperbolic media can support hyperbolic modes over a broad spectral band, the flux that they can transport can be high. It even seems possible to achieve with hyperbolic metamaterials a radiative thermal conductivity that can in principle be comparable to the phononic conductivity (Biehs *et al.*, 2015; Liu and Narimanov, 2015). Recently first experimental steps were made to verify this claim (Salihoglu *et al.*, 2019), but the experimental results are not yet convincing, because the measurement is not clearly demonstrating the impact of the radiative part. In a more detailed study it could be demonstrated that the near-field heat flux between two slabs can be guided through a hyperbolic waveguide over distances larger than the thermal wavelength so that larger heat fluxes than the blackbody value are achievable for far-field distances (Messina *et al.*, 2016). On the other hand, it could also be shown that the guiding performance greatly depends on the dissipative properties of the waveguide material and also that for long-distance guiding low-loss infrared materials like Ge would already have good long-range guiding properties (Messina *et al.*, 2016). The long-range guiding effect has

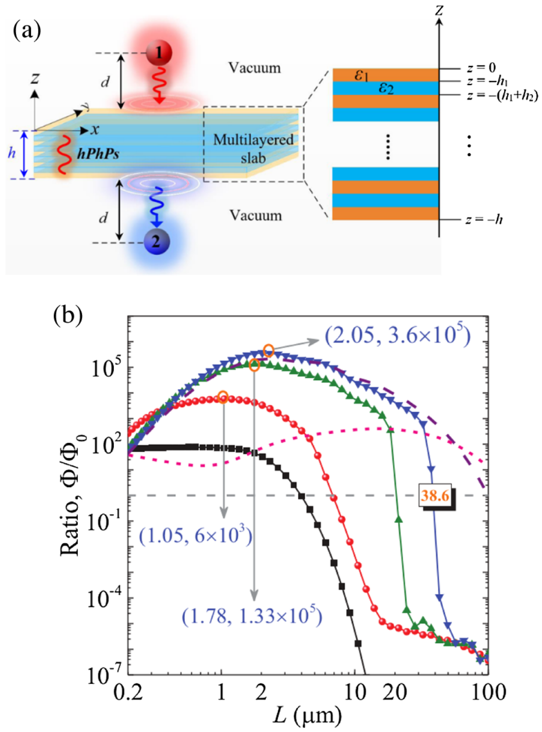

FIG. 28. (a) Sketch of heat flux between two nanoparticles through a hyperbolic multilayer metamaterial. (b) Exchanged power Φ as a function of interparticle distance L normalized to the exchanged power Φ_0, where the hyperbolic multilayer metamaterial has been replaced by vacuum. The numbers in the brackets give the distance L (in μm) and the amplification factor Φ/Φ_0 at the maximum. From Zhang, Yi *et al.*, 2019.

also been predicted for the heat flux between two nanoparticles through hyperbolic multilayer structures (Zhang, Yi *et al.*, 2019), as shown in Fig. 28.

Even though the enhancement of the heat flux due to coupling to the surface modes of the phonon-polaritonic or plasmonic structures can be several orders of magnitude, it has to be kept in mind that the aforementioned studies consider the steady-state heat flux between the nanoparticles and that the enhancement is relative to the case where the interface is removed. Hence, even by increasing the heat flux by several orders of magnitude at a distance of 1 μm the absolute value of the heat flux is still small because the heat flux between the nanoparticles follows the $1/d^6$ law in the near-field regime (Volokitin and Persson, 2001). Furthermore, it should be kept in mind that by bringing the nanoparticles into close vicinity of an interface not only the heat flux between the particles but also the thermal emission of the hot particle increases into the substrate so that the hot particle will tend to cool by thermal emission into the substrate rather than by heating the cooler nanoparticle. However, the first thermal relaxation study showed (Ott and Biehs, 2020) that, by wisely choosing the distances between the nanoparticles and between the nanoparticles and the interface, a substantial heating of the cold nanoparticle can be observed. Similar considerations also hold for the heat flux though a structure. Hence, it will be useful to focus in future studies on heat fluxes and the thermal relaxation or actual heating or cooling performance as well.

4. Relaxation dynamics

The temporal dynamics of any many-body system in interaction with an external environment or with local thermostats is simply driven by the competition between its thermal inertia and the strength of the thermal link with the external environment and these thermostats. Close to the thermal equilibrium, the time evolution of temperatures $\mathbf{T} = (T_1, \ldots, T_N)$ in Eq. (83) is driven by the linear dynamical system

$$\mathbb{I}\frac{d\mathbf{T}}{dt} = -\mathbb{C}\mathbf{T}(t) + \mathbb{C}_b\mathbf{T}_b, \tag{93}$$

where $\mathbb{I} = \mathrm{diag}(I_1, \ldots, I_N)$ is the diagonal inertia matrix that depends on the mass density, heat capacity, and size of each element, $\mathbf{T}_b = (T_{b1}, \ldots, T_{bN})$ is the temperature of the external bath and reservoirs with which each element interacts, $\mathbb{C}_b = \mathrm{diag}(G_{1b}, \ldots, G_{Nb})$, with G_{ib} the thermal conductance between element i and the bath or a thermostat, while $\mathbb{C}$ is the general conductance matrix with components

$$\mathbb{C}_{ij} = \left(\sum_{k\neq i} G_{ik} + G_{ib}\right)\delta_{ij} - (1-\delta_{ij})G_{ij}, \tag{94}$$

with G_{ij} the conductance between element i and j defined as follows:

$$G_{ij} = 3\int_0^\infty \frac{d\omega}{2\pi}\hbar\omega\left.\frac{\partial n}{\partial T}\right|_{T=T_j}\mathcal{T}_{ij}(\omega). \tag{95}$$

A corresponding definition can be used for slabs. Note that this definition is valid only in the absence of temperature dependence for optical properties of the materials involved. When the conductance matrix is independent of time the thermal state of the system reads

$$\mathbf{T}(t) = \exp[-\mathbb{I}^{-1}\mathbb{C}t]\mathbf{T}(0) + \int_0^t \exp[-\mathbb{I}^{-1}\mathbb{C}(t-\tau)]\mathbb{I}^{-1}\mathbb{C}_b\mathbf{T}_b(\tau)d\tau, \tag{96}$$

with $\mathbf{T}(0)$ the initial state. Hence, the relaxation dynamic is driven by the set $\{\Gamma_i\}$ of eigenvalues of the matrix $\mathbb{I}^{-1}\mathbb{C}$, and the dominant relaxation time is given by $\tau = 1/\min(\Gamma_i)$ ($\mathbb{C}$ is a strictly diagonally dominant matrix with positive diagonal elements).

Generally speaking the relaxation process takes place at different scales (Messina, Tschikin *et al.*, 2013). When the separation distance between the different elements is subwavelength they are first thermalized in the near-field regime at the same temperature. This generally happens in a few milliseconds (Wang and Wu, 2016) for objects of nanometric size (Fig. 29) and even in hundreds of microseconds for two-dimensional nanosystems (Zundel and Manjavacas, 2020). In the second step each element and therefore the entire system thermalizes in far field toward the bath temperature.

This difference in the timescales for the relaxation dynamics can also be studied in a simpler system when considering a single nanoparticle at temperature T_1 close to a sample with a

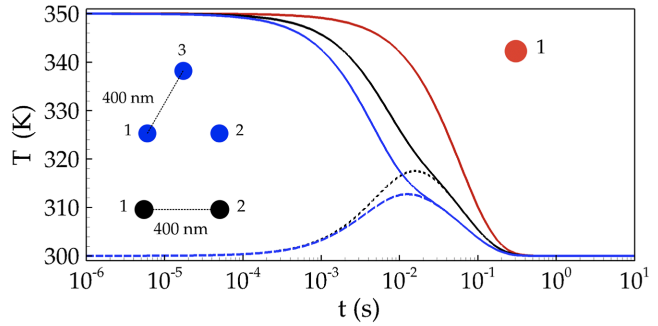

FIG. 29. Time evolution of thermal state in a single-body (red curve), a two-body (black curve), and a three-body system (blue curve) of SiC nanoparticles with radii of 50 nm in a bath at temperature $T = 300$ K. The distance between particles 1 and 2 is 400 nm, while the distances (solid line for dipole 1, dashed line for dipole 2, and dot-dashed line for dipole 3). From Messina, Tschikin *et al.*, 2013.

fixed background temperature T_b. Equation (93) then reduces to

$$\frac{dT_1}{dt} = \frac{G_{1b}}{I_1}(T_b - T_1) \tag{97}$$

or, equivalently,

$$\frac{d\Delta T}{dt} = -\Gamma \Delta T, \tag{98}$$

where $I_1 = \rho C_\mathrm{p} V$ is the thermal inertia of the nanoparticle and $\Delta T = T_1 - T_b$ and the relaxation rate $\Gamma = G_{1b}/I_1$. The solution to this differential equation is simply $\Delta T(t) = \Delta T(0)\exp(-\Gamma t)$ or $T_1(t) = [T_1(0) - T_b]\exp(-\Gamma t) + T_b$. Hence, the relaxation time in this case is the inverse of the relaxation rate $\tau = \Gamma^{-1}$, which is itself determined by the thermal inertia and the heat conductance between the nanoparticle and the sample.

The heat conductance for this configuration has been studied for spherical dielectric and metallic nanoparticles close to a sample with a flat surface (Dorofeyev, 1998; Mulet *et al.*, 2001; Volokitin and Persson, 2002; Dedkov and Kyasov, 2007; Chapuis, Laroche *et al.*, 2008b), between a spherical dielectric nanoparticle and a structured or rough surface (Biehs, Huth, and Rüting, 2008; Kittel *et al.*, 2008; Biehs and Greffet, 2010c; Rüting *et al.*, 2010), and between dielectric and metallic ellipsoidal particles and a flat or structured surface (Biehs *et al.*, 2010; Huth *et al.*, 2010). Here we focus on a spherical nanoparticle with radius R in a distance d over a planar interface. For $d \gg R$ it can be shown (Dorofeyev, 1998; Mulet *et al.*, 2001; Volokitin and Persson, 2002; Dedkov and Kyasov, 2007; Chapuis, Laroche *et al.*, 2008b) that G_{1b} is proportional to the electric (magnetic) photonic local density of states $D^\mathrm{E}(\omega, d)$ (D^H), as defined by Agarwal (1975b) and Eckhardt (1982) for dielectric (magnetic) nanoparticles above a dielectric (magnetic) substrate. Hence, when disregarding mixed cases such as those considered by Manjavacas and de Abajo (2012) and Dong, Zhao, and Liu (2017a), the relaxation rate can be written as (Tschikin *et al.*, 2012)

$$\Gamma = \frac{1}{I_1}\sum_{i=E,H}\int_0^\infty d\omega\, 2\hbar\omega^2 \mathrm{Im}(\alpha^i) D^i(\omega, d)\frac{dn}{dT}\bigg|_{T_b}, \tag{99}$$

where α^E is its electric and α^H is its magnetic polarizability. The latter takes into account the magnetic moments due to eddy currents, which play an important role for thermal emission of metallic nanoparticles (Martynenko and Ognev, 2005; Tomchuk and Grigorchuk, 2006; Dedkov and Kyasov, 2007; Chapuis, Laroche *et al.*, 2008b). Hence, we find that in comparison to the spontaneous emission of an atom or molecule above a substrate (Novotny and Hecht, 2006), where the emission rate is proportional to the local density of states for the transition frequency, the thermal emission rate is given by a spectral average of the local density of states with respect to $\hbar\omega dn/dT$. Hence, the thermal relaxation rate reassembles the spontaneous emission rate if the nanoparticles have a narrow band emission spectrum.

In Fig. 30 it can be seen that the thermal relaxation time changes by orders of magnitude when going from the far-field into the near-field regime, which is due to the strong increase

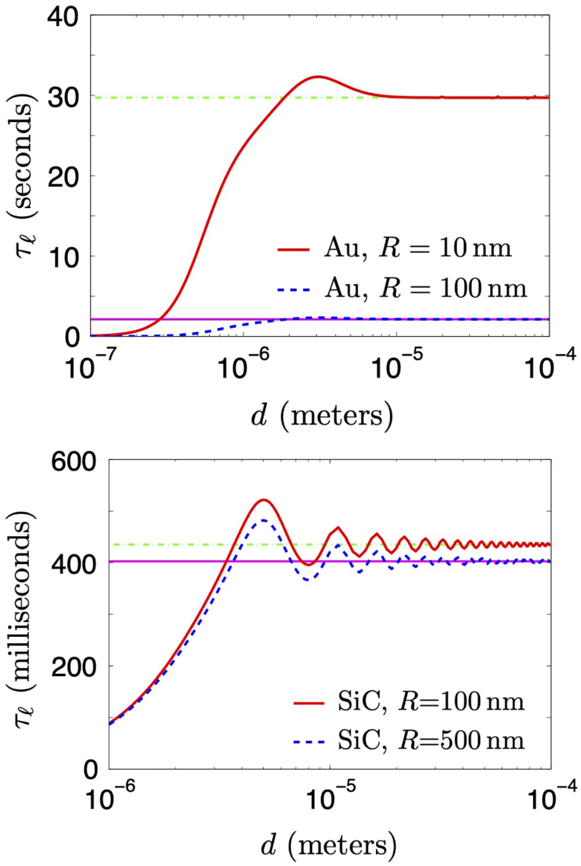

FIG. 30. Distance dependence of the relaxation time $\tau = \Gamma^{-1}$ of a nanoparticle above a substrate with temperature $T_b = 300$ K (top panel) for a gold nanoparticle above a gold surface, and (bottom panel) for a SiC nanoparticle above a SiC surface. We use $\rho^\mathrm{Au} C_\mathrm{p}^\mathrm{Au} = 2.404 \times 10^6\ \mathrm{J\,m^{-3}\,K^{-1}}$ and $\rho^\mathrm{SiC} C_\mathrm{p}^\mathrm{SiC} = 2.212 \times 10^6\ \mathrm{J\,m^{-3}\,K^{-1}}$. From Tschikin *et al.*, 2012.

in G_{1b}, i.e., the local density of states, in the near-field regime (Joulain *et al.*, 2003; Dorofeyev and Vinogradov, 2011). There is also a large difference for metallic and dielectric nanoparticles due to the fact that thermal radiation is more efficient for dielectrics than for metals. Furthermore, it can be seen that for SiC oscillations in the transition region between the near-field and far-field regimes, which can be interpreted as the photonic counterpart of the Friedel oscillations (Joulain *et al.*, 2003). These oscillations are due to the oscillations in the local density of states, which average out for the gold nanoparticle (broadband thermal emission spectrum) but remain for the SiC nanoparticle (narrow band thermal emission spectrum). A detailed discussion was given by Tschikin *et al.* (2012).

5. Dynamical control

A control of the magnitude of heat flux was highlighted in layered many-body systems (He, Qi, Li *et al.*, 2019) coated by graphene sheets simply by tuning the doping level of graphene. Beyond this control several principles have been introduced during the last decade to dynamically control both the magnitude and the direction of heat flux at nanoscale with many-body systems. For example, by changing the shape and orientation of elements (Nikbakht, 2014) the heat flux can be modulated by several orders of magnitude with anisotropic particles, as shown in Fig. 31(a). Another example for a dynamical modulation that can by realized by electrical gating is the heat-flux splitter sketched in Fig. 31(b). It enables one to control the direction of the heat flux in the near-field regime. The design is based on a network of tunable graphene pallets (Ben-Abdallah *et al.*, 2015) that allow us to spatially control the near-field interactions and therewith the direction of heat flux by dynamically tuning the graphene plasmons. A similar control was also performed with polar particles covered by graphene (Song *et al.*, 2019).

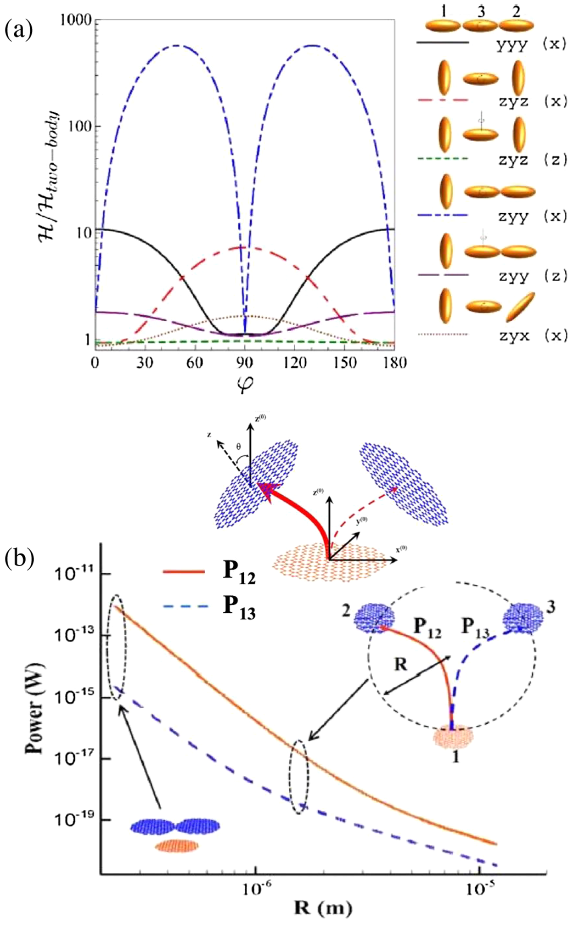

FIG. 31. (a) Normalized heat flux between two spheroidal nanoparticles with respect to the orientation of a third particle placed in between. From Nikbakht, 2014. (b) Graphene-based heat-flux splitter. Three graphene disks with different Fermi levels controlled by external gating exchange thermal energy in the near-field through many-body interactions. The magnitude of heat flow from 1 to 2 and 1 to 3 can be controlled by an appropriate tuning of the Fermi level of the graphene disks 2 and 3. The thermal power exchanged in the near-field between graphene disks of 100 nm radius vs the separation distance in a three-body system. From Ben-Abdallah *et al.*, 2015.

By 2014 it could already be demonstrated that the flux exchanged between two solids can even be amplified through a transistor effect (Ben-Abdallah and Biehs, 2014) by using a phase-change material like VO_2 for an intermediate relay also called the gate between two SiO_2 slabs functioning as source and drain at temperatures $T_S = 360$ K and $T_D = 300$ K, as illustrated in Fig. 32. Since this configuration corresponds to two oppositely connected heat radiation diodes (Ben-Abdallah and Biehs, 2013; Yang, Basu, and Wang, 2013; Ito *et al.*, 2014; Gu, Tang, and Tao, 2015; Fiorino *et al.*, 2018),

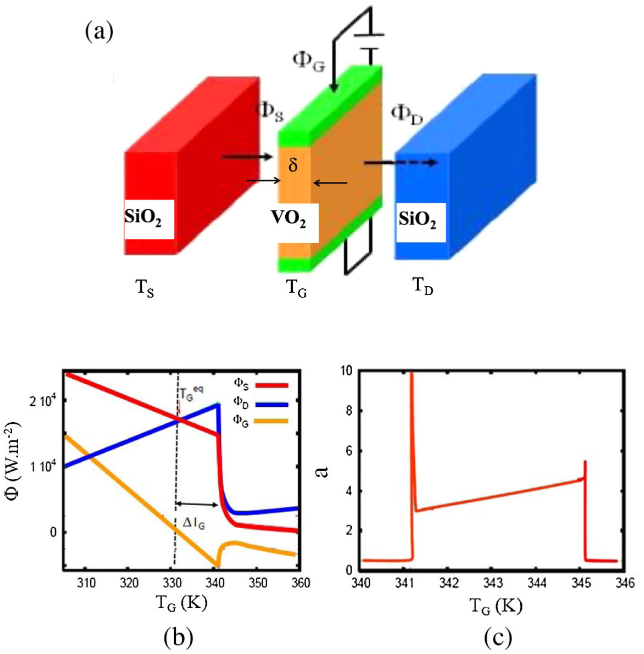

FIG. 32. (a) Radiative thermal transistor made of a three-terminal system composed of a SiO_2 source, a VO_2 gate, and a SiO_2 drain. The gate is a layer based on a phase-change material and its temperature can be actively controlled around its local equilibrium value T_G^{eq} by an external thermostat, while the temperatures $T_S = 360$ K and $T_D = 300$ K of source and drain are fixed so that $T_S > T_D$. (b) Radiative fluxes Φ_S, Φ_D, and Φ_G exchanged between the different parts inside the transistor. (c) Amplification factor with respect to the gate temperature. From Ben-Abdallah and Biehs, 2014.

this transistor corresponds to a bipolar transistor so that the terminology emitter, base, and collector would be more appropriate, but this has no impact on the physics involved. In the region of the phase transition around its critical temperature $T_c \approx 340$ K, even though the temperature difference between the gate and the drain is increased a drastic reduction of flux Φ_D received by the drain takes place. This arises due to the strong change in the optical properties of the $\mathrm{VO_2}$ gate from a dielectric to a metallic response shielding the heat flux from the source toward the drain, as can be seen in Fig. 32(b). This variation corresponds to the presence of a negative differential thermal conductance or resistance (Li, Wang, and Casati, 2006) $R_D = (\partial\Phi_D/\partial T_G)^{-1}$ induced by the phase transition. In the transition region, the amplification factor

$$a = \left|\frac{\partial\Phi_D}{\partial\Phi_G}\right| \tag{100}$$

of the flux received by the drain Φ_D compared to the heat flux Φ_G removed or added to the gate can be defined. It can also be recast in terms of the thermal resistances of the source and the drain as

$$a = \left|\frac{R_S}{R_S + R_D}\right|, \tag{101}$$

with the positive resistance $R_S = -(\partial\Phi_S/\partial T_G)^{-1}$. This expression shows that the amplification factor can become larger than 1 only if R_D is negative, so a negative thermal resistance is a necessary condition for obtaining an amplification. For the thermal transistor the amplification factor is larger than 1 in the phase-change temperature region, as can be seen Fig. 32(c). Note that the peaks at the edges of the phase transition are an artifact of the effective medium model used to model the transition of the optical properties of $\mathrm{VO_2}$ at the edges of the transition region, which was due to a lack of experimental data at these edges. Investigations of the same effect in the far-field regime as impacts the hysteresis of the transistor were conducted by Joulain *et al.* (2015) and Prodhomme *et al.* (2016, 2018), while the dynamical response of transistors was addressed by Latella *et al.* (2019).

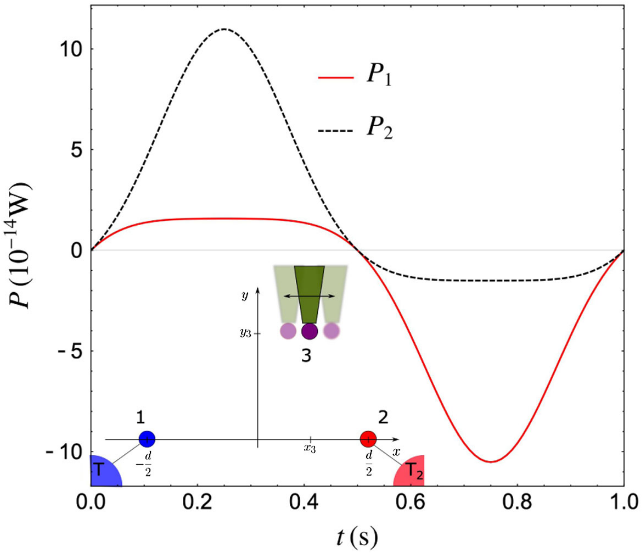

FIG. 33. Radiative heat pumping by modulation of control parameters in a three-particle system that is sketched in the inset. The three particles are made of SiC. In this case, particles 1 and 2 are thermostated at temperature $T_1 = T_2$, while the temperature T_3 and the x_3 coordinate of particle 3 can be modulated with respect to time. Powers $\mathcal{P}_1$ and $\mathcal{P}_2$ absorbed by particles 1 (solid red line) and 2 (dashed black line) as a function of time for the a periodic variation of the coordinate and temperature of particle 3 of frequency $\omega = 2\pi\ \mathrm{s}^{-1}$ and amplitudes $\Delta x = 100$ nm and $\Delta T = 5$ K around $x_3 = 0$ and $T_3 = 300$ K. We have $d = 600$ nm and $y_3 = 300$ nm, and the radius of the particle is $R = 50$ nm. Inset: geometrical configuration of a three-particle system where the position of particle 3 is periodically modulated. From Messina and Ben-Abdallah, 2020.

The principle of negative thermal resistance further plays an important role in so-called radiative heat shuttling, which was recently proposed (Latella, Messina *et al.*, 2018). In a system consisting of only two parallel slabs, it was shown that the periodic modulation of the temperature and/or chemical potential of the two bodies can be exploited to control the heat flux between them. More specifically, it was proven that in order to thermally insulate them a negative thermal differential resistance is required. A further step in this direction was taken by Messina and Ben-Abdallah (2020), who tailored the heat flux between two particles by periodically modulating the temperature T_3 and the position x_3 of a third particle in a three-particle system, as sketched in the inset of Fig. 33. This many-body configuration allows for controlling the direction and amplitude of the heat exchanged between the two particles 1 and 2, even when they are kept at the same temperature and (unlike the previously mentioned shuttling effect) in the absence of a negative thermal differential resistance (Messina and Ben-Abdallah, 2020). This possibility can be anticipated by performing a Taylor expansion up to second order, around the middle position $x_3 = 0$ and the equilibrium temperature $T_3 = T_{3,\mathrm{eq}}$ of particle 3. This gives

$$\begin{aligned}\mathcal{P}_1 \simeq{}& \mathcal{P}_1(0, T_{3,\mathrm{eq}}) + \frac{\partial\mathcal{P}_1}{\partial x_3}x_3 + \frac{\partial\mathcal{P}_1}{\partial T_3}(T_3 - T_{3,\mathrm{eq}})\\ &+ \frac{1}{2}\frac{\partial^2\mathcal{P}_1}{\partial x_3^2}x_3^2 + \frac{1}{2}\frac{\partial^2\mathcal{P}_1}{\partial T_3^2}(T_3 - T_{3,\mathrm{eq}})^2\\ &+ \frac{\partial^2\mathcal{P}_1}{\partial x_3\partial T_3}x_3(T_3 - T_{3,\mathrm{eq}}).\end{aligned} \tag{102}$$

For a time variation of the form $T_3(t) = T_{3,\mathrm{eq}} + \Delta T\sin(\omega t)$ and $x_3(t) = \Delta x\sin(\omega t + \phi)$ and in the specific case $T_1 = T_2 = T_{3,\mathrm{eq}}$, the time average over a period reads

$$\langle\mathcal{P}_1\rangle_t \simeq \frac{\Delta T}{2}\left(\Delta x\frac{\partial^2\mathcal{P}_1}{\partial x_3\partial T_3}\cos\phi + \frac{\Delta T}{2}\frac{\partial^2\mathcal{P}_1}{\partial T_3^2}\right). \tag{103}$$

Equation (103) shows that magnitude of the first term can be easily modulated simply by changing the dephasing ϕ between x_3 and T_3, paving the way to an active heat pumping mechanism. The sign can be changed as well so that the heat can flow from cooler to warmer regions. A numerical example of this modulation for a vanishing dephasing $\phi = 0$ is shown in Fig. 33, where the averages over a period of the powers P_1 and P_2 absorbed by particles 1 and 2 (having temperatures $T_1 = T_2 = 300$ K) are positive and negative, respectively.

6. Heat transport regimes

It is commonly admitted that heat conduction inside a bulk solid is governed by a normal diffusion process. Heat carriers that are electrons or phonons move through the atomic lattice following a usual random walk that is driven by a Gaussian distribution function as in Fig. 34(a). In this section we discuss how heat carried by thermal photons is transported in many-body systems. We demonstrate the existence of anomalous regimes of transport as in Fig. 34(b). In dilute systems we show that heat can spread out following a superdiffusive process (Lévy, 1937; Shlesinger, Zaslavsky, and Frisch, 1995), while in dense systems it can be ballistically transported.

To start this analysis, we consider a network of small objects at temperature T_i that are distributed inside a background or environment at temperature T_b. When the separation distance between two arbitrary objects in this network is much larger than their characteristic size and that their size is small enough relative to the thermal wavelengths $\lambda_{T_i} = c\hbar/(k_B T_i)$, this network can be modeled as a set of simple dipoles located at positions $\mathbf{r}_i$ in mutual interaction and in interaction with the surrounding bath. In the near-field regime the power exchanged with the bath is negligible, as discussed in Sec. III.C.4, compared to the internal exchanges. Then the time evolution of objects temperature is governed by Eq. (93) while neglecting the heat exchange with the background yielding

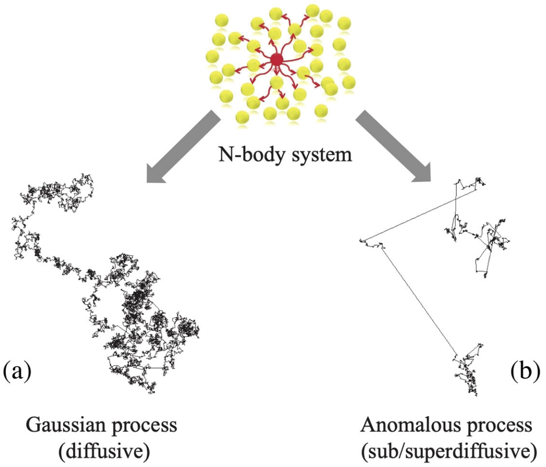

FIG. 34. Types of heat transport regimes in an N-body system. When an element (red) is heated up its heat spreads through the system by either (a) a classical Gaussian diffusion process or (b) an anomalous process. The trajectories correspond to random walks with a Gaussian and a non-Gaussian probability distribution function, respectively. Here the non-Gaussian process is a Levy flight with an algebraic PDF.

$$I_i \frac{dT_i}{dt} = \sum_{j\neq i} G_{ij}(T_j - T_i), \tag{104}$$

where I_i represents the thermal inertia of object i while G_{ij} stands for the thermal conductance between dipole j and i as defined in Eq. (95), which depends only on the distance between the dipoles

$$G_{ij} \equiv G(|\mathbf{r}_i - \mathbf{r}_j|). \tag{105}$$

In the continuous limit the energy balance equation (104) can be recast as (Ben-Abdallah *et al.*, 2013)

$$\frac{\partial T_i}{\partial t} = \int_{R^d} d\mathbf{r}\, p(\mathbf{r}_i, \mathbf{r}) \frac{T(\mathbf{r}, t)}{\tau(\mathbf{r})} - \frac{T(\mathbf{r}_i, t)}{\tau(\mathbf{r_i})}, \tag{106}$$

where the integration is done over the entire space of dimension d. Equation (106) is formally an analog to a Chapman-Kolmogorov master equation that drives a generalized Markov process. The temperature field $T(\mathbf{r}, t)$ is a passive scalar that evolves by following a generalized random walk of probability distribution function (PDF)

$$p(\mathbf{r}, \mathbf{r}') = \frac{G(|\mathbf{r} - \mathbf{r}'|)}{\int_{R^d} d\mathbf{r}' G(|\mathbf{r} - \mathbf{r}'|)} \tag{107}$$

and the rate of jumps between two collision events

$$\tau(\mathbf{r}) = \left(\int_{R^d} d\mathbf{r}' G(|\mathbf{r} - \mathbf{r}'|)\right)^{-1}. \tag{108}$$

Hence, by analyzing the spatial variation of the PDF and therefore of the conductance as well between two points inside the system, we can identify the regime of heat transport. If the asymptotic behavior of the PDF $p(x)$ (where we set $x = |\mathbf{r} - \mathbf{r}'|$) is Gaussian, all its moments $M^{(n)} = \int x^n p(x) dx$ are finite, so the regime of transport is diffusive. On the other hand, if it decays algebraically, i.e., $p(x) = O(1/x^\gamma)$ and hence $G(x) = O(1/x^\gamma)$, then there is a given order $\tilde{n}$ beyond which $M^{(n)}$ diverges for any $n > \tilde{n}$. In this case, the heat transport regime becomes superdiffusive; see the right trajectory in Fig. 34. In this case the continuous energy balance equation takes the form (Ben-Abdallah *et al.*, 2013)

$$I \frac{\partial T}{\partial t} = -\kappa(-\Delta)^{(\gamma-d)/2} T(\mathbf{r}), \tag{109}$$

where κ is a parameter that depends on the dimension d and $(-\Delta)^{\alpha/2}$ denotes the fractional Laplacian (Shlesinger, Zaslavsky, and Frisch, 1995)

$$(-\Delta)^{\alpha/2} T(\mathbf{r}) = c_{d;\alpha} \mathrm{PV} \int_{R^d} d\mathbf{r}' \frac{T(\mathbf{r}) - T(\mathbf{r}')}{|\mathbf{r} - \mathbf{r}'|^{d+\alpha}}, \tag{110}$$

with

$$c_{d;\alpha} = \frac{2^{-\alpha} \pi^{1+d/2}}{\Gamma(1+\alpha/2)\Gamma[(d+\alpha)/2] \sin(\alpha\pi/2)}. \tag{111}$$

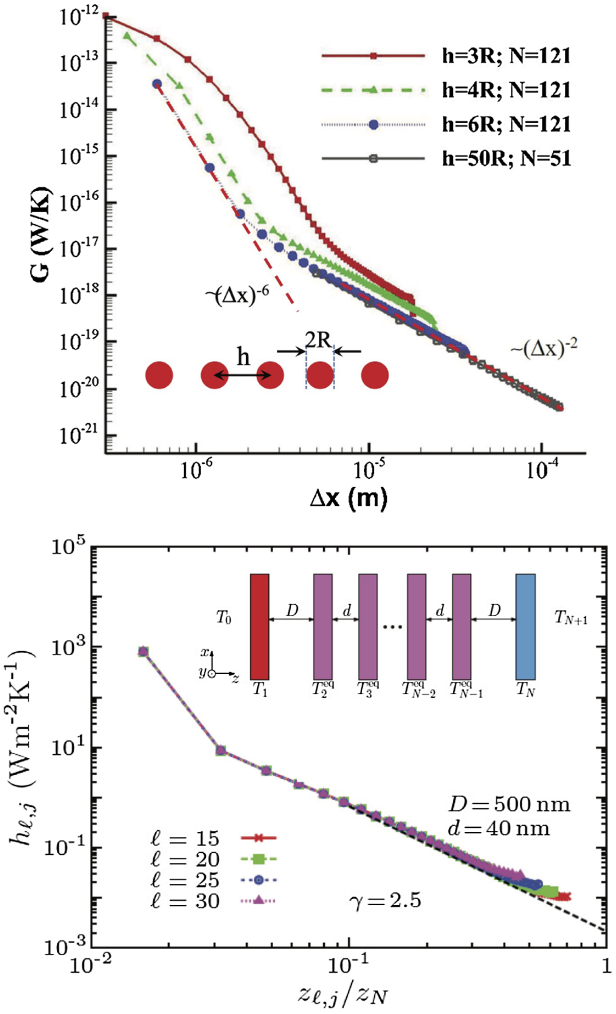

FIG. 35. Top panel: thermal conductance G in log-log scale along a chain of SiC spherical particles of 100 nm radius with different interparticle distances h and different particle numbers N as a function of the separation distance $\Delta x = |\mathbf{r} - \mathbf{r}'|$ at temperature $T = 300$ K. From Ben-Abdallah *et al.*, 2013. Bottom panel: heat-transfer coefficients $h_{\ell,j}$ with respect to the normalized separation $z_{\ell,j}/z_N$ in a dilute multilayer system made with 200 nm thick SiC layers separated by a distance $d = 40$ nm at $T = 300$ K. From Latella, Biehs *et al.*, 2018.

PV stands for the principal value. Note that Eq. (109) is general and can be applied to describing the energy balance in arbitrary dipolar or macroscopic systems. When $\gamma \to d+2$ the fractional Laplacian degenerates into its classical form, i.e., $(-\Delta)^{\alpha/2} = (-\Delta)$, and the transport regime is diffusive. On the other hand, when $\gamma \to d$ the fractional Laplacian approaches the identity operator and the transport becomes ballistic. Finally, when $d < \gamma < d+2$ the regime is superdiffusive.

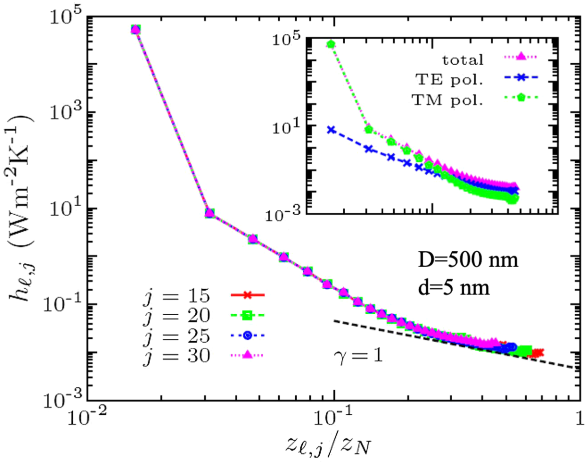

FIG. 36. Heat-transfer coefficient $h_{\ell,j}$ with respect to the normalized separation $z_{l,j}/z_N$ in a dense multilayer system made with 200 nm thick SiC layers separated by a distance $d = 5$ nm at $T = 300$ K. Inset: $h_{\ell,j}$ decomposed into TE and TM polarization contributions. From Latella, Biehs *et al.*, 2018.

In Figs. 35 and 36 we show the existence of those regimes in two simple many-body systems: (1) linear chains of nanoparticles periodically dispersed in vacuum and (2) multilayer periodic systems. In the first system [see Fig. 35(a)], the thermal conductance $G(\Delta x)$ between a central particle and another particle at a distance Δx is calculated for different filling factors $2R/h$. For any filling factor, we see that G decays asymptotically at long separation distance as $1/\Delta x^2$, i.e., $\gamma = 2$, showing (according to our previous discussion) that the regime of heat transport is superdiffusive. In the example plotted in Fig. 35(a) the long-range interactions that give rise to this anomalous regime come from the presence of collective electromagnetic modes supported by the entire structure. In the case of a chain made with SiC particles, these modes result from the coupling of surface phonon polaritons localized on each particle (Ben-Abdallah *et al.*, 2013; Ordonez-Miranda *et al.*, 2015; Kathmann *et al.*, 2018; Tervo, Cola, and Zhang, 2020).

A similar superdiffusive regime is observed in dilute multilayer systems [see Fig. 35(b)] where the heat-transfer coefficient $h_{l,j}$ between layers l and j decays algebraically and scales as $1/z_{l,j}^{2.5}$, where $z_{l,j}$ is the distance between layers l and j so that $\gamma = 2.5$. On the other hand, in a dense multilayer system such as the one considered in Fig. 35(b) a transition occurs between this superdiffusive regime and a ballistic regime (Latella, Biehs *et al.*, 2018; He, Qi, Wang *et al.*, 2019). In this case we see that $h_{l,j}$ scales as $1/z_{l,j}$, meaning that the transport becomes ballistic and the temperature profile inside the structure submitted to a temperature difference is constant, as can be seen in Fig. 37, having a value T^* that is close to the Casimir temperature $T_C = (T_1 + T_N)/2$. This regime of heat transport seems to be inconsistent with the previous arguments about the collective modes supported by the structure, but it occurs due to the fact that the coupling of the inner dense multilayers is much stronger than the coupling to the two outer baths when $d \ll D$. For $D = d$, on the other hand, the temperature profile in Fig. 37 is reminiscent of a quasiballistic temperature distribution. Although the transition mechanism remains partially elusive today, it was shown by Latella, Biehs *et al.* (2018) that the mechanism is related to a change of channel for heat exchanges in dense systems from TM-dominated to TE-dominated heat transfer; see the inset of Fig. 36. For this TE polarization state the slabs no longer support surface waves.

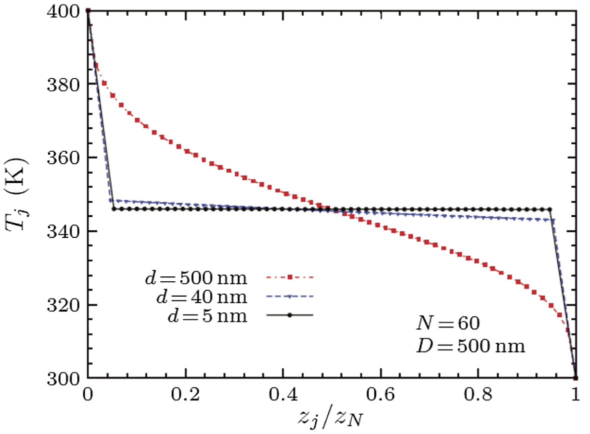

FIG. 37. Temperature profile as a function of the normalized position z_j/z_N along a multilayer made with 200 nm thick $N = 60$ SiC layers for different separation distances d and at a fixed distance $D = 500$ nm from the thermostats. From Latella, Biehs *et al.*, 2018.

D. Nonreciprocal systems

In electromagnetics, a nonreciprocal system is defined as a system that exhibits different received-transmitted field ratios when a source and a detector are interchanged. This concept is also closely related to a time reversal symmetry breaking of Maxwell's equation. In this case the classical Lorentz's reciprocity is violated (Caloz *et al.*, 2018). Here we discuss first the general formulation of radiative power exchange between nonreciprocal objects and then show how RHT is taking place in nonreciprocal many-body systems made for sets of simple nonreciprocal nanoparticles.

1. General discussion

As a first step, we consider only two objects 1 and 2 having temperatures T_1 and T_2, respectively, which are immersed into a background or environment having another temperature T_b. Under the assumption that the objects and the environment can be considered to be in local thermal equilibrium, the power absorbed by object 1 can be determined with the conventional FE approach analogous to Eq. (54) as (Latella and Ben-Abdallah, 2017; Herz and Biehs, 2019)

$$\mathcal{P}_1 = 3\int_0^\infty \frac{d\omega}{2\pi}\hbar\omega[(n_1 - n_b)\mathcal{T}_{11} + (n_2 - n_b)\mathcal{T}_{12}], \qquad (112)$$

where $n_{1/2} = n(T_{1/2})$ and $n_b = n(T_b)$. The transmission coefficients $\mathcal{T}_{11/12}$ were explicitly given in terms of the T operators of the objects by Herz and Biehs (2019), who derived them within the scattering approach (Krüger *et al.*, 2012). Here we give explicitly only the expression for $\mathcal{T}_{21}$, which is given by (Herz and Biehs, 2019)

$$\mathcal{T}_{12} = \tfrac{4}{3}\mathrm{Tr}[\mathbb{D}^{-1}\mathbb{G}\chi_2(\mathbb{D}^{-1}\mathbb{G})^\dagger\tilde{\chi}_1], \qquad (113)$$

where Tr is the operator trace, $\mathbb{G}$ is the operator for the Green's function $\mathbb{D} = (\mathbb{1} - \mathbb{G}\mathbb{T}_2\mathbb{G}\mathbb{T}_1)$ written in terms of the T operators $\mathbb{T}_{1/2}$ of both objects, and the generalized susceptibilities are defined as

$$\chi_2 = \frac{\mathbb{T}_2 - \mathbb{T}_2^\dagger}{2i} - \mathbb{T}_2\frac{\mathbb{G} - \mathbb{G}^\dagger}{2i}\mathbb{T}_2^\dagger, \qquad (114)$$

$$\tilde{\chi}_1 = \frac{\mathbb{T}_1 - \mathbb{T}_1^\dagger}{2i} - \mathbb{T}_1^\dagger\frac{\mathbb{G} - \mathbb{G}^\dagger}{2i}\mathbb{T}_1. \qquad (115)$$

Note that Eqs. (114) and (115) are formally equivalent to Eqs. (64) and (74). Analogous expressions were also given by Zhu, Guo, and Fan (2018) and more explicitly for spherical nanoparticles by Ott and Biehs (2020). The corresponding expression for the absorbed power $\mathcal{P}_2$ in object 2 can be obtained by exchanging $1 \leftrightarrow 2$ in Eqs. (112) and (113). First, it can now be seen in Eq. (112) that in global thermal equilibrium the overall absorbed power is zero. Second, when setting $T_1 = T_b$, Eq. (112) can describe only the absorbed power in object 1 due to the heat flow coming from or going toward object 2. Thus, $\mathcal{T}_{12}$ can be identified as the transmission coefficient describing the heat flow from object 2 to 1. Third, when assuming that $T_2 = T_b$ Eq. (112) describes the heat flow from object 1 to the environment and to object 2, or vice versa. Therefore, we can identify $\mathcal{T}_{11}$ as the transmission coefficient standing for the so-called self-emission of object 1 (Krüger *et al.*, 2012). Finally, when one takes $T_1 = T_2$ Eq. (112) describes the power flowing from the environment toward object 1 either directly or via object 2. Therefore, $\mathcal{T}_{11} + \mathcal{T}_{12}$ equals the transmission coefficient $\mathcal{T}_{1b}$, as we also discussed for N dipolar objects when deriving Eq. (56). These observations allow us to rewrite Eq. (112) as

$$\begin{aligned}\mathcal{P}_1 &= 3\int_0^\infty \frac{d\omega}{2\pi}\hbar\omega[n_1\mathcal{T}_{11} + n_2\mathcal{T}_{12} - n_b\mathcal{T}_{1b}]\\ &\equiv \mathcal{P}_{1\to1}(T_1) + \mathcal{P}_{2\to1}(T_2) + \mathcal{P}_{b\to1}(T_b)\end{aligned} \qquad (116)$$

while introducing

$$\mathcal{P}_{1\to1}(T_1) = +3\int_0^\infty \frac{d\omega}{2\pi}\hbar\omega n_1\mathcal{T}_{11}, \qquad (117)$$

$$\mathcal{P}_{2\to1}(T_2) = +3\int_0^\infty \frac{d\omega}{2\pi}\hbar\omega n_2\mathcal{T}_{12}, \qquad (118)$$

$$\mathcal{P}_{b\to1}(T_b) = -3\int_0^\infty \frac{d\omega}{2\pi}\hbar\omega n_b\mathcal{T}_{1b}, \qquad (119)$$

where the first term stands for the self-emission of body 1, the second term is the emission toward body 2, and the last term is the power coming from the bath. Notice that when the two bodies are set at the same temperature we can make a connection between the transmission coefficient $\mathcal{T}_{b\to1}$ and the thermal emissivity $\epsilon = \sigma_{\mathrm{abs}}/S$ (Biehs and Ben-Abdallah, 2016). More specifically, $\mathcal{T}_{b\to1}$ can be expressed as a function of its absorption cross section (30), its geometrical cross section S, and the absorbed power as follows:

$$\mathcal{T}_{b\to 1}(\omega) = \frac{A}{6\pi}\epsilon(\omega)\frac{\omega^2}{c^2} = \frac{A}{6\pi}\frac{\sigma_{\rm abs}(\omega)}{S}\frac{\omega^2}{c^2}, \qquad (120)$$

where A is the surface of the object (assumed convex).

The self-emission term $\mathcal{P}_{1\to 1}$ appearing in Eq. (117) must balance the energy flow from the other object 2 and the environment described by $\mathcal{P}_{2\to 1}$ and $\mathcal{P}_{\rm b\to 1}$ to establish global equilibrium so that this term describes the power needed to keep the temperature of object 1 constant in thermal equilibrium. Hence, when taking $T_1 = T_2 = T_b$ we have $\mathcal{P}_1 = 0$ and therefore

$$\mathcal{P}_{1\to 1}(T_b) = -\mathcal{P}_{2\to 1}(T_b) - \mathcal{P}_{b\to 1}(T_b). \qquad (121)$$

This equation relates $\mathcal{P}_{1\to 1}$ to $\mathcal{P}_{2\to 1}$ and $\mathcal{P}_{b\to 1}$ and therefore allows us to eliminate the background term $\mathcal{P}_{b\to 1}(T_b)$ from the expression for the overall absorbed power giving (Krüger *et al.*, 2012)

$$\begin{aligned}\mathcal{P}_1 = \mathcal{P}_{1\to 1}(T_1) - \mathcal{P}_{1\to 1}(T_b) \\ + \mathcal{P}_{2\to 1}(T_2) - \mathcal{P}_{2\to 1}(T_b).\end{aligned} \qquad (122)$$

This elimination of the background term is clear from the previous definitions, showing that $\mathcal{T}_{1\to b}$ can also be expressed by $\mathcal{T}_{1\to 1}$ and $\mathcal{T}_{2\to 1}$, and the implementation of the equilibrium condition brings us back to Eq. (112). As described by Krüger *et al.* (2012) this expression for $\mathcal{P}_1$ can now be generalized to the case of N objects in a given environment. In this case $(i = 1, \ldots, N)$

$$\mathcal{P}_i = \sum_{j=1}^{N}[\mathcal{P}_{j\to i}(T_j) - \mathcal{P}_{j\to i}(T_b)]. \qquad (123)$$

This is the general N-body formula for the power absorbed by object i, of which Eq. (54) can be considered a special case for dipolar objects. For an explicit calculation of the absorbed power it is necessary to determine the transmission coefficients for the studied configuration. Before focusing on the heat flow in some specific cases, we want to discuss in Sec. III.D.2 the impact of the nonreciprocity in a similarly general way.

2. General impact of nonreciprocity

For Lorentz-reciprocal objects and their environment the corresponding response functions, i.e., the permittivity tensor, polarizability tensor, T operator, Green's function, etc., are symmetric (Caloz *et al.*, 2018). Consequently, in this case we have symmetric transmission coefficients $\mathcal{T}_{12} = \mathcal{T}_{21}$ or more generally for N objects $\mathcal{T}_{ij} = \mathcal{T}_{ji}$ $(i \neq j)$. This means that we have detailed balance for the heat flux between any two objects (Krüger *et al.*, 2012). In contrast, for configurations where the objects or the environment do not fulfill the conditions for Lorentz reciprocity it was explicitly proven by Herz and Biehs (2019) that in general $\mathcal{T}_{12} \neq \mathcal{T}_{21}$. More precisely, $\mathcal{T}_{12} = \mathcal{T}_{21}$ if and only if the objects and their environment are both reciprocal. Therefore nonreciprocity introduces in general a directionality for the heat flow.

One of the astonishing consequences is that in nonreciprocal systems one has $\mathcal{P}_{12} \neq \mathcal{P}_{21}$ in general so that the heat-flux-related expressions for the reciprocal case fulfilling detailed balance need to be generalized to nonreciprocal cases where detailed balance is broken (Zhu and Fan, 2014) like the Green-Kubo relation for heat radiation (Golyk, Krüger, and Kardar, 2013; Herz and Biehs, 2019). This asymmetry in the heat flow from object 1 to object 2 and from 2 to 1 exists even in global thermal equilibrium, suggesting that there might be a net heat flow even though there is no temperature difference. However, by looking at Eq. (112) one sees that although the heat flux from object 1 toward object 2 is different than the heat flux from object 2 to 1 there is no net heat flow in global equilibrium because $\mathcal{P}_1 = \mathcal{P}_2 = 0$ in that case. The same is also true for N objects, where due to nonreciprocity one has in general $\mathcal{P}_{i\to j} \neq \mathcal{P}_{j\to i}$ $(i \neq j)$. As we later discuss in more detail, this can result in a so-called persistent heat current in an N-body configuration in global thermal equilibrium (Zhu and Fan, 2016; Zhu, Guo, and Fan, 2018; Ott *et al.*, 2019a).

In many works on the radiative heat exchange between two objects the contribution of the environmental field is neglected. In that case, as pointed out by Latella and Ben-Abdallah (2017), the global equilibrium can be achieved only if the transmission coefficients fulfill the condition

$$\sum_{j\neq i}[\mathcal{T}_{ij} - \mathcal{T}_{ji}] = 0. \qquad (124)$$

In particular, this implies that when having only two objects $\mathcal{T}_{12} = \mathcal{T}_{21}$. Hence, for two isolated objects the nonreciprocity has no impact and therefore at least three objects are necessary to observe a broken detailed balance. From this general finding it can be understood that Zhu and Fan (2014) had to consider three nonreciprocal thermal emitters to show that detailed balance can be broken for thermal radiation and that Zhu and Fan (2016) had to consider three nonreciprocal nanoparticles to observe the persistent heat current. On the other hand, the heat exchange between two nonreciprocal half-spaces will not show any rectification effect (Moncada-Villa *et al.*, 2015; Fan *et al.*, 2020). Note that the symmetry relation $\mathcal{T}_{12}(\boldsymbol{\kappa},\omega) = \mathcal{T}_{21}(-\boldsymbol{\kappa},\omega)$ for the transmission coefficient of the heat flux between two planar reciprocal media will be violated if at least one medium is nonreciprocal, which allows one to distinguish the reciprocal from the nonreciprocal case (Fan *et al.*, 2020). Finally, when considering two objects with an environment, the environment can be regarded as a third object. This explains why in general for only two objects in a given environment the transmission coefficients can be asymmetric $(\mathcal{T}_{1\to 2} \neq \mathcal{T}_{2\to 1})$ so that we have here no contradiction of the previous discussion.

3. Magneto-optical nanoparticles

In the following we review the results obtained for the RHT in many-body systems consisting of subwavelength nanoparticles. Most of the works neglected the coupling to the background, which can be justified in steady-state situations when the distance between the objects is much smaller than the thermal wavelength so that the near-field coupling dominates over the coupling to the environment (Messina, Tschikin *et al.*, 2013). Therefore, we work here with Eq. (58) together with the transmission coefficients $\mathcal{T}_{ij}$ defined in Eq. (55). Neglecting the radiation correction it can also be written as

$$\mathcal{T}_{ij}(\omega) = \frac{4}{3}\mathrm{Tr}\left[\underline{\underline{\alpha}}^{-1}\boldsymbol{T}_{ij}^{-1}\frac{\underline{\underline{\alpha}} - \underline{\underline{\alpha}}^{\dagger}}{2i}(\underline{\underline{\alpha}}^{-1}\boldsymbol{T}_{ij}^{-1})^{\dagger}\frac{\underline{\underline{\alpha}} - \underline{\underline{\alpha}}^{\dagger}}{2i}\right], \qquad (125)$$

assuming that all particles have the same polarizability $\underline{\underline{\alpha}}$ defined for spherical nanoparticles by means of the permittivity in Eq. (68) with the volume $V = 4\pi R^3/3$ (Lakhtakia, Varadan, and Varadan, 1991)

$$\underline{\underline{\alpha}} = 4\pi R^3(\underline{\underline{\epsilon}} - \mathbb{1})(\underline{\underline{\epsilon}} + 2\mathbb{1})^{-1}. \qquad (126)$$

The transmission coefficients in Eq. (125) are equal to the expressions given by Ben-Abdallah, Biehs, and Joulain (2011) and Ekeroth, García-Martín, and Cuevas (2017) for spherical nanoparticles within the so-called weak-coupled dipole limit (Lakhtakia, 1992), where the radiation correction can be neglected (Albaladejo *et al.*, 2010). They can also be derived from the general T-operator expressions obtained within the scattering approach for the reciprocal (Krüger *et al.*, 2012) and the nonreciprocal case (Zhu, Guo, and Fan, 2018; Herz and Biehs, 2019).

As already done in Sec. II.C we consider InSb as magneto-optical material for which the permittivity tensor becomes asymmetric ($\underline{\underline{\epsilon}}^t \neq \underline{\underline{\epsilon}}$); i.e., the material properties are nonreciprocal when a magnetic field is applied. As a consequence, the polarizability tensor then has the same asymmetry $\underline{\underline{\alpha}} \neq \underline{\underline{\alpha}}^t$. Furthermore, owing to the applied field the threefold degeneracy of the dipolar localized plasmon resonances, the solution of the transcendental equation $\det(\underline{\underline{\epsilon}} + 2\mathbb{1}) = 0$ with magnetic quantum number $m = -1, 0, +1$ is lifted (Weick and Weinmann, 2011; Pineider *et al.*, 2013). In particular, there is a redshift of the resonance with $m = +1$ and a blueshift of the resonance with $m = -1$. The size of the splitting is proportional to the cyclotron frequency $\omega_c = eB/m^*$, with m^* the effective mass of electrons (Weick and Weinmann, 2011; Pineider *et al.*, 2013). To be more precise, in the regime where the dissipation can be neglected we find the resonances (Ott, Ben-Abdallah, and Biehs, 2018)

$$\omega_{m=\mp 1} = \sqrt{\left(\frac{\epsilon_\infty \omega_p^2}{\epsilon_\infty + 2} + \frac{\omega_c^2}{4}\right)} \pm \frac{\omega_c}{2},$$
$$\omega_{m=0} = \sqrt{\frac{\epsilon_\infty \omega_p^2}{\epsilon_\infty + 2}}, \qquad (127)$$

which are determined by the poles of the polarizability tensor. Therefore, for small magnetic fields the two circular resonances with $m = \pm 1$ are shifted by $\mp\, \omega_c/2$ with respect to the unaffected resonance for $m = 0$.

4. Giant magnetoresistance

Because of the strong dependence of dipolar resonances of particles on the magnetic field, the heat flux emitted by a magneto-optical particle can drastically change by tuning this field (Latella and Ben-Abdallah, 2017; Ekeroth *et al.*, 2018). It turns out that the thermal magnetoresistance

$$R_{ij}(\mathbf{B}) = \left(3\int_0^\infty \frac{d\omega}{2\pi}\hbar\omega \frac{\partial n}{\partial T}\mathcal{T}_{ij}(\omega, \mathbf{B})\right)^{-1} \qquad (128)$$

between two particles in a many-body system is strongly dependent on the magnitude of the applied magnetic field, as can be seen in Fig. 38(a). Variations of about 50% along nanoparticle chains have been highlighted with magnetic fields of a magnitude of about 500 mT (Latella and Ben-Abdallah, 2017). This sensitivity to the magnetic field is of the same order of magnitude as the giant electric magnetoresistance reported in ferromagnetic–normal metal multilayers (Baibich *et al.*, 1988). This resistance can also be tuned by changing the direction of the applied magnetic field (Ekeroth *et al.*, 2018). In this case we speak of an anisotropic magnetoresistance. As shown in Fig. 38(b), for certain orientations of the magnetic field the heat flux can drop by more than 90%. These effects open up the opportunity to control or modulate the amplitude of the heat flux between nanoparticles by external means. More detailed discussions were given by Latella and Ben-Abdallah (2017), Ekeroth *et al.* (2018), and Ott *et al.* (2019a).

5. Persistent heat flux, angular momentum, spin, and heat current

As shown by Ott, Ben-Abdallah, and Biehs (2018), the circular plasmonic resonances for $m = \pm 1$ of a single particle

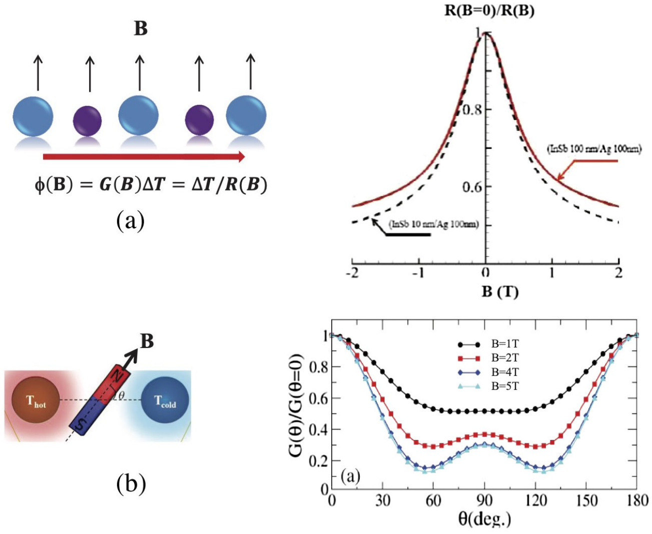

FIG. 38. (a) Giant thermal magnetoresistance along linear chains of InSb and InSb/Ag nanoparticles at $T = 300$ K as a function of the strength of an external magnetic field B applied in the direction orthogonal to the chain axis. From Latella and Ben-Abdallah, 2017. (b) Anisotropic magnetoresistance between two InSb nanoparticles with respect to the orientation of the magnetic field. From Ekeroth *et al.*, 2018.

responsible for magnetic circular dichroism (Pineider *et al.*, 2013) and the "inverse Faraday effect" (Gu and Kornev, 2010) are connected with a circular mean heat flux

$$\langle \mathbf{S} \rangle = \langle \mathbf{E} \times \mathbf{H} \rangle \tag{129}$$

emitted by the nanoparticle in planes perpendicular to the applied magnetic field. This results in a certain spectral angular momentum density $\langle \mathbf{J}_\omega \rangle = \langle \mathbf{L} \rangle_\omega + \langle \mathbf{S}_d \rangle_\omega$, which can be divided into an orbital angular momentum density $\langle \mathbf{L} \rangle_\omega$ and a spin angular momentum density $\langle \mathbf{S}_d \rangle_\omega$ defined as (Bliokh and Nori, 2015)

$$\langle \mathbf{L} \rangle_\omega = \mathbf{r} \times \langle \mathbf{P} \rangle_\omega, \tag{130}$$

$$\langle \mathbf{S}_d \rangle_\omega = \frac{g}{2} \mathrm{Im}\left(\langle \mathbf{E}^* \times \mathbf{E} \rangle + \frac{\mu_0}{\epsilon_0} \langle \mathbf{H}^* \times \mathbf{H} \rangle \right), \tag{131}$$

with $g = \epsilon_0/\omega$ and the canonical spectral momentum density given by

$$\langle \mathbf{P} \rangle_\omega = \frac{g}{2} \mathrm{Im}\left[\langle \mathbf{E}^* (\nabla) \mathbf{E} \rangle + \frac{\mu_0}{\epsilon_0} \langle \mathbf{H}^* (\nabla) \mathbf{H} \rangle \right], \tag{132}$$

adopting the notation of Bliokh and Nori (2015) that $\vec{X}(\vec{Y})\vec{Z} = \sum_i X_i \vec{Y} Z_i$. Using these definitions together with FE the persistent angular momentum close to the walls of a cavity was first evaluated and discussed by Silveirinha (2017) and the angular momentum and spin for a thermally emitting nanoparticle by Ott, Ben-Abdallah, and Biehs (2018). A more detailed study of the angular momentum and spin close to a planar interface was published recently (Khandekar and Jacob, 2019a).

That there is a finite angular momentum and spin of the thermally emitted radiation is not surprising, because the Lorentz force constrains the electrons in the nanoparticles on a circular orbit so that the dipolar resonance is rotating in the plane perpendicular to the magnetic field that is the microscopic origin of the circular heat flux (Fig. 39) and the total angular momentum. The right-hand rule determines the direction of the circular heat flux in the near-field regime (Ott, Ben-Abdallah, and Biehs, 2018). Note that the angular momentum of the $m = +1$ ($m = -1$) resonance is oriented in the same (opposite) direction of the magnetic field, as one would expect, whereas the spin of the $m = -1$ ($m = +1$) is oriented in the same (opposite) direction of the magnetic field in the near-field regime. From this perspective the splitting of the $m = \pm 1$ resonances can also be understood as a Zeeman splitting, where $m = -1$ ($m = +1$) is blueshifted (redshifted) because the near-field direction of the spin is in the same (opposite) direction as the magnetic field, but the correct quantity determining the Zeeman splitting is the magnetic momentum of the dipolar resonance itself (Gu and Kornev, 2010). The presence of a finite spin means that the thermal emission of the nonreciprocal nanoparticle will be circularly polarized in general, as is well known for solid matter within a magnetic field like semiconductors (Kollyukh *et al.*, 2005), but also white dwarfs (Kemp, 1970; Kemp *et al.*, 1970). More recently, circularly polarized thermal emitters based on chiral metasurfaces (Dyakov *et al.*, 2018) and nanoantennas (Khandekar and Jacob, 2019b) were proposed.

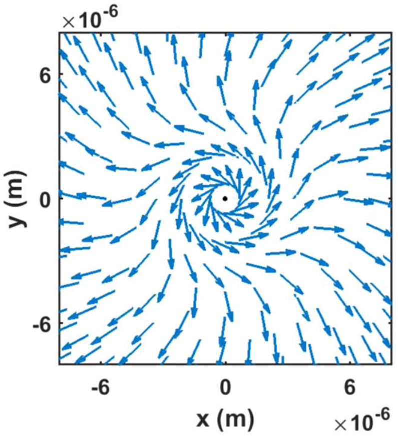

FIG. 39. Normalized mean Poynting vector $\langle \mathbf{S} \rangle$ of thermal radiation emitted by an InSb nanoparticle at the origin of the coordinate system with radius of 300 nm at a temperature of 300 K into a cold environment (vacuum) at $T_b = 0$ K when a magnetic field is applied in z direction. This circular heat flux persists in global thermal equilibrium. From Ott, Ben-Abdallah, and Biehs, 2018.

It turns out that these three quantities (mean heat flux, orbital angular momentum, and spin) persist in global equilibrium if $\underline{\underline{\alpha}} \neq \underline{\underline{\alpha}}^t$ and therefore are a direct consequence of the nonreciprocity of the permittivity or polarizability. Even though it might seem strange to have a nonzero mean heat flux in global equilibrium circulating around the nanoparticle, this does not pose any problem from the thermodynamical point of view, since it can be shown that $\nabla \cdot \langle \mathbf{S}_{\mathrm{pers}} \rangle = 0$, which means that there is no heat flux through any closed surface including the nanoparticle (Ott, Ben-Abdallah, and Biehs, 2018). In other words, no heat is finally emitted. Similar conclusions have been made for the thermal-radiation field of the nonreciprocal surface modes on planar interfaces (Silveirinha, 2017; Khandekar and Jacob, 2019a).

Instead of a persistent heat flux, i.e., a nonzero heat flux in global thermal equilibrium, as observed from the mean Poynting vector around a nonreciprocal nanoparticle or in the vicinity of a planar interface of a nonreciprocal sample, there can be a persistent heat current, as first discussed by Zhu and Fan (2016) for the thermal radiation exchanged by three nanoparticles, but it exists also for more than three particles (Zhu, Guo, and Fan, 2018). We know from the previous discussion that, when neglecting the contribution of the environment of the nanoparticles, it follows from the constraint in Eq. (124) that for only two nanoparticles $\mathcal{T}_{12} = \mathcal{T}_{21}$, and consequently $\mathcal{P}_{1\to 2} = \mathcal{P}_{2\to 1}$ if $T_1 = T_2$. Therefore, it is necessary to have at least three nanoparticles to have $\mathcal{T}_{12} \neq \mathcal{T}_{21}$. For three particles as in Fig. 40 the constraint in Eq. (124) demands that $\mathcal{T}_{12} = \mathcal{T}_{23} = \mathcal{T}_{31}$ and $\mathcal{T}_{13} = \mathcal{T}_{32} = \mathcal{T}_{21}$ due to the C_3 symmetry. If the three nanoparticles are now nonreciprocal, then it can be shown from the definition of the transmission coefficient in Eq. (125) that $\mathcal{T}_{12} \neq \mathcal{T}_{21}$, and hence

$$\mathcal{P}_{1\to 2} = \mathcal{P}_{2\to 3} = \mathcal{P}_{3\to 1} \neq \mathcal{P}_{1\to 3} = \mathcal{P}_{3\to 2} = \mathcal{P}_{2\to 1}. \tag{133}$$

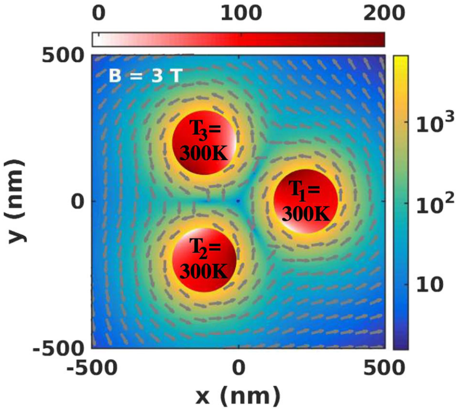

FIG. 40. Normalized mean Poynting vector $\langle \mathbf{S} \rangle$ and its magnitude ($\mathrm{W\,m^{-2}}$ in color scale) of thermal radiation emitted by three InSb nanoparticles with a radius of 300 nm having the same temperatures $T_1 = T_2 = T_3 = 300$ K when a magnetic field is applied in the z direction. From Ott *et al.*, 2019a.

This means there is a clockwise heat flow exchanged by the nanoparticles that is different from the heat flow in the counterclockwise direction even if $T_1 = T_2 = T_3$, and therefore there is a persistent heat current in either the clockwise or the counterclockwise direction, depending on which of the two heat flows is larger. This persistent heat flow or better heat current (Zhu and Fan, 2016) is the many-body analog of the persistent heat flux, which also exists in the three-body configuration. Note from Eq. (124) that, in a nonreciprocal system at temperature T, the bodies i and j still exchange a power (Latella and Ben-Abdallah, 2017)

$$\mathcal{P}^{\mathrm{eq}}_{i\leftrightarrow j} = \mathcal{P}^{\mathrm{eq}}_{j\to i} - \mathcal{P}^{\mathrm{eq}}_{i\to j} = \int_0^\infty \frac{d\omega}{2\pi} \hbar\omega\, n(\omega, T)[\mathcal{T}_{ij} - \mathcal{T}_{ji}], \tag{134}$$

although the net power $\mathcal{P}^{\mathrm{eq}}_j = \sum_{i\neq j} \mathcal{P}^{\mathrm{eq}}_{i\leftrightarrow j}$ vanishes so that the persistent heat flux does not lead to any heating or cooling. Hence, the magnitude of asymmetry of transmission coefficient spectra (Fig. 41) and the value of the equilibrium temperature are directly responsible for the value of the persistent current. Today the measurement of this current is still a challenging problem. Recently a setup was proposed by Khandekar and Jacob (2019a) that might be able to access the current in the vicinity of a magneto-optical planar sample.

6. Hall effect for thermal radiation

The asymmetry in the exchanged heat flux in many-body configurations observed in global equilibrium, i.e., the persistent heat current, has directly measurable consequences when driving the system out of global equilibrium. A consequence is the Righi-Leduc or Hall effect for thermal radiation (Ben-Abdallah, 2016). Classically, the Righi-Leduc effect (Leduc, 1887; Righi, 1887) is simply the thermal analog of the Hall effect (Hall, 1879). When applying a temperature difference in a metallic sample together with a magnetic field, the heat current by the electrons is deflected due to the Lorentz force acting on the electrons such that a temperature difference perpendicular to the initially applied temperature difference builds up in steady state. Such an effect has also been highlighted for other heat carriers in solids like magnons and spinons (Fujimoto, 2009; Katsura, Nagaosa, and Lee, 2010; Onose *et al.*, 2010), or even phonons (Strohm, Rikken, and Wyder, 2005; Inyushkin and Taldenkov, 2007).

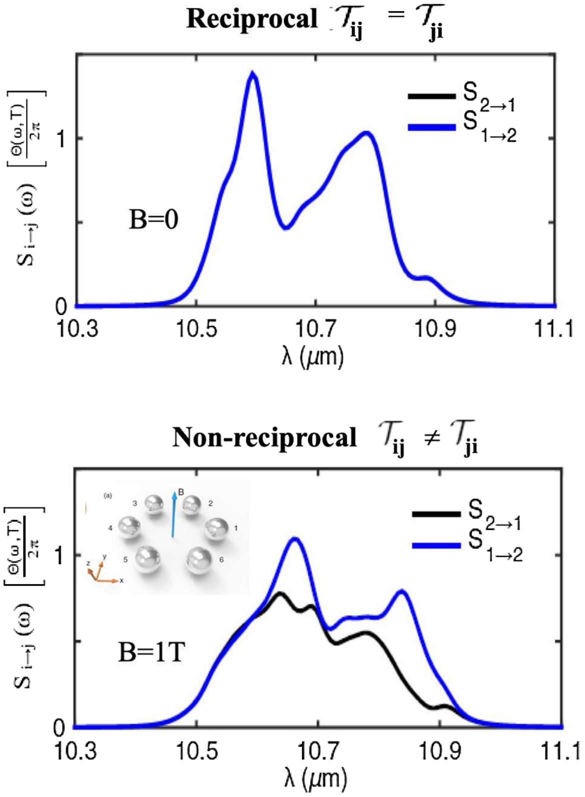

FIG. 41. Heat-transfer spectra in a many-body system consisting of six InSb nanospheres placed at the vertices of a regular hexagon on the x-y plane without (reciprocal) and with (nonreciprocal) an externally applied magnetic field in the z direction. From Zhu and Fan, 2016, and Zhu, Guo, and Fan, 2018.

When considering heat radiation exchanged between four nanoparticles in a C_4 symmetric configuration as in Fig. 42 and applying a temperature difference $\Delta T = T_L - T_R$ between particle L (left) and R (right), in the steady state of the system a temperature difference $T^{\mathrm{st}}_B - T^{\mathrm{st}}_T$ between particle B (bottom) and T (top) can build up when using nonreciprocal InSb nanoparticles and applying a magnetic field perpendicular to the particle plane. Hence, one observes a Righi-Leduc or Hall effect for thermal radiation (Ben-Abdallah, 2016). Again, the effect can be understood as the Lorentz force acting on the electrons in the nanoparticles. However, here the electrons do not serve as heat carriers but introduce a circular heat flux leading to an asymmetric heat flow, and finally to the Righi-Leduc effect. Its magnitude and directionality can be measured by the relative Hall temperature difference or Righi-Leduc-like coefficient

$$R_T = \frac{T^{\mathrm{st}}_B - T^{\mathrm{st}}_T}{T_L - T_R}, \tag{135}$$

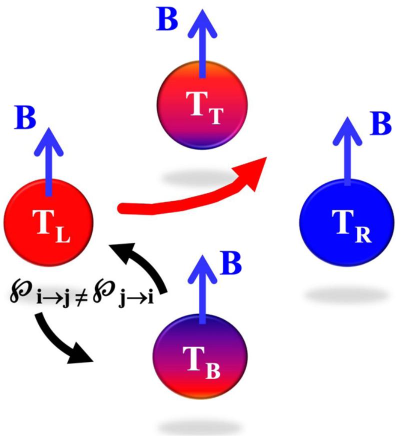

FIG. 42. Photon thermal Hall effect. A four-terminal junction with magneto-optical particles forming a square with C_4 symmetry is submitted to an external magnetic field **B** in the direction orthogonal particle plane. When a temperature gradient $\Delta T = T_L - T_R$ is applied between the particles L and R, a Hall flux transfers heat transversally between particles B and T, thus bending the overall flux (red arrow) toward the top or the bottom. In this case the heat $\mathcal{P}_{i\to j}$ and $\mathcal{P}_{j\to i}$ exchanged between two particles i and j is not symmetric.

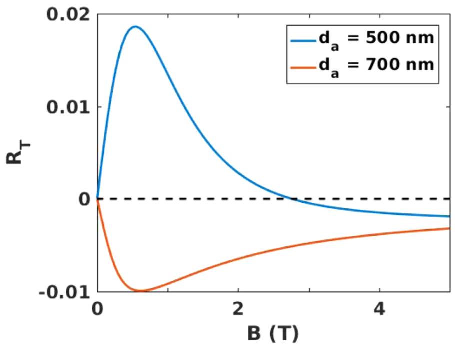

FIG. 43. Magnetic-field strength dependence of the Righi-Leduc-like coefficient defined in Eq. (135) for four spherical InSb nanoparticles with a radius of 100 nm in a C_4-symmetric configuration as depicted in Fig. 42 choosing an interparticle distance of opposite particles of $d_a = 500$ and 700 nm. From Ott *et al.*, 2019a.

which is shown in Fig. 43. Written in terms of thermal conductances, this coefficient reads (Ben-Abdallah, 2016; Ott, Biehs, and Ben-Abdallah, 2020)

$$R_T = \frac{G_{LB} - G_{BL}}{G_{LB} + G_{BL} + 2G_{BT}}. \tag{136}$$

We see that, depending on the magnitude of the magnetic field, the effect will change its directionality and there is a maximum for a magnetic-field amplitude of about 0.5 T for the considered configuration. The effect is not strong and high field amplitudes are needed to have a maximum effect. However, it strongly depends on the configuration and material parameters (Ott *et al.*, 2019b), and therefore its magnitude can be optimized by changing the spatial distribution of the particles or their physical properties. An experimental proof of photon thermal Hall effect remains a challenging problem. However, a direct measurement of the Hall temperature difference with measurements of electrical resistance variations with a high accuracy (St-Gelais *et al.*, 2014) in magneto-optical nanowire networks seems feasible.

Besides the “normal” thermal Hall effect, anomalous effects also called anomalous thermal Hall effects (Ferreiros, Zyuzin, and Bardarson, 2017; Huang, Han, and Stone, 2020), a thermal analog of the anomalous Hall effect (Karplus and Luttinger, 1954; Nagaosa *et al.*, 2010), have also been described for the heat transport with electrons or phonons in ferromagnetic materials and in semimetals. Recently a similar effect in Weyl semimetal nanoparticle networks for thermal photons was predicted (Ott, Biehs, and Ben-Abdallah, 2020). Since Weyl semimetals can exhibit a strong nonreciprocal response in the infrared, this effect allows for a directional control of heat flux by simply locally tuning the magnitude of the temperature field without changing the direction of the temperature gradient.

7. Heat-flux rectification with nonreciprocal surface waves

For most of the nonreciprocal effects discussed thus far the environment does not play a decisive role. Now, instead of using only the intrinsical nonreciprocal properties of the nanoparticles to achieve a directional heat flux, the nonreciprocity of the environment can be exploited as first shown by Ott *et al.* (2019a). As we saw in Sec. III.C.3, the heat flux between two nanoparticles, or more generally between two objects brought into close vicinity to an interface of a sample, can be enhanced by transporting the heat via the surface modes of the interface (Sääskilahti, Oksanen, and Tulkki, 2014; Asheichyk, Müller, and Krüger, 2017; Dong, Zhao, and Liu, 2018; Messina, Biehs, and Ben-Abdallah, 2018; He, Qi, Ren *et al.*, 2019; Zhang, Antezza *et al.*, 2019). If the material properties of the planar sample are nonreciprocal, then the presence of a magnetic field will affect the surface modes (Chiu and Quinn, 1972).

To be more specific, within the Voigt configuration shown in Figs. 44(a) and 44(b) the dispersion relation for the surface modes at the interface of the substrate traveling to the right and left will be different (Chiu and Quinn, 1972). As in the case of the localized mode inside an InSb nanoparticle, the degeneracy of the surface modes for $k_x > 0$ and $k_x < 0$ is lifted and there is a splitting of the surface-mode resonance frequency (Chiu and Quinn, 1972). Since the spin associated with the surface modes (Bliokh and Nori, 2012) shows a spin momentum locking (Van Mechelen and Jacob, 2016), meaning that the waves with $k_x > 0$ and $k_x < 0$ have different spin directions, the splitting can again be understood as a Zeeman splitting (Van Mechelen and Jacob, 2016; Khandekar and Jacob, 2019a).

Now, considering the situation in Figs. 44(a) and 44(b), the thermally excited localized modes of the hot nanoparticle can directly couple to the localized modes of the cold nanoparticle leading to a direct heat transfer between the particles. The thermally excited localized modes of the hot particle can couple to the surface modes of the substrate, travel along the interface of the substrate, and then couple to the localized

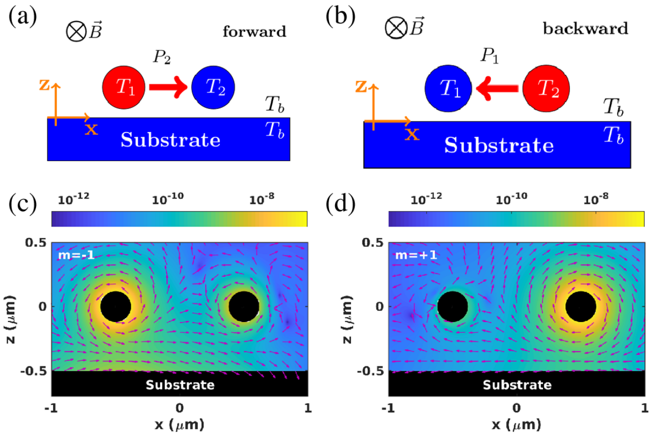

FIG. 44. (a) Sketch of the diode in the forward direction. Two InSb nanoparticles above an InSb substrate. The left particle is heated with respect to the other particle and the environment. (b) Sketch of the diode in the backward direction. (c) Normalized mean spectral in-plane Poynting vector and its amplitude (J m^{-2}; colorbar) for the $m = +1$ particle resonance for the diode in the forward direction. (d) Similar to (c) but for the backward case and the $m = -1$ particle resonance. See also Ott and Biehs (2020).

modes of the cold nanoparticle so that in this case the heat is transferred between the two nanoparticles via the surface modes. Because of the nonreciprocity of the substrate the heat flow $\mathcal{P}_2$ in the forward direction in Fig. 44(a) and the heat flow $\mathcal{P}_1$ in the backward direction in Fig. 44(b) will be different, leading to a rectification effect (Ott *et al.*, 2019a). A detailed analysis showed (Ott and Biehs, 2020) that there is a spin-selective coupling so that the localized modes couple preferably to the surface modes with the spin in the same direction. For example, the $m = -1$ ($m = +1$) resonance couples preferably to the surface modes with $k_x > 0$ ($k_x < 0$), providing the main heat-flux channel in the forward (backward) direction as shown in Fig. 44(c) [Fig. 44(d)]. This can be also understood by a matching of the circularity of the particle resonances and the directionality of the interface resonances. The resulting rectification coefficient

$$\eta = \frac{\mathcal{P}_1 - \mathcal{P}_2}{\mathcal{P}_1} \tag{137}$$

shown in Fig. 45 can be rather high even for relatively small magnetic fields. It should be kept in mind that when bringing the nanoparticles close to a substrate most of the heat will go to the substrate rather than the other nanoparticle. Nonetheless, the rectification effect can result in a measurable heating of the cold nanoparticle (Ott and Biehs, 2020).

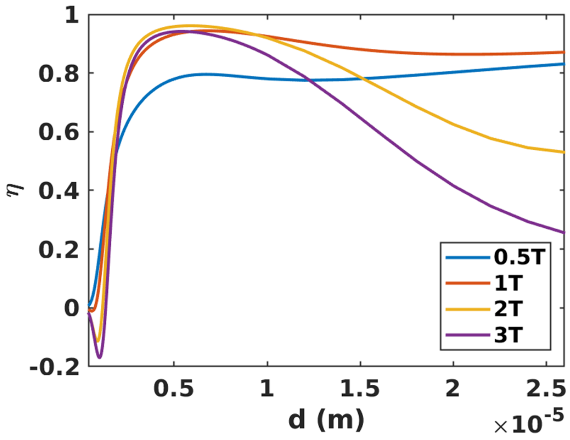

FIG. 45. Rectification coefficient from Eq. (137) for two InSb nanoparticles with a 100 nm radius 500 nm above an InSb substrate, as sketched in Fig. 44, as a function of the interparticle distance d for different magnetic-field amplitudes. See also Ott and Biehs (2020).

IV. OUTLOOK AND OPEN QUESTIONS

While the heat transport mechanisms mediated by thermal photons in 1D and 3D systems have been intensively studied during the last decade, they remain unknown in 2D systems. Can we observe a diverging radiative conductivity with respect to system size as has already been predicted for the phononic conductivity in 2D anharmonic lattices? To answer this question and also identify different heat transport regimes in these systems, we must analyze the scaling laws of radiative thermal conductance. Another fundamental problem is the crossover from 1D to 2D and 3D to 2D systems. The spatial confinement of evanescent photons in these systems should play a key role in those transitions.

To date dense many-body systems and effects like weak and strong localization for thermal radiation remain largely unexplored. In these strongly correlated systems, heat is typically carried through multiple connected channels associated with different heat carriers like electrons, phonons, and photons, which raises the question: under which conditions can one or more of these heat carriers dominate heat transport? As highlighted in the Introduction of this review, progress in unifying various transport mechanisms is beginning to be made, yet a complete theory capable of describing multichannel heat exchange in large many-body systems remains a challenge for understanding possible transport effects associated with coupling across such different channels.

As the number of bodies in an interaction becomes large, the general formalism described in this review becomes numerically prohibitive. This is a serious issue to investigate heat transport in many-body systems in the presence of long-range interactions. A continuous description of heat transport in these systems could make the study of these systems feasible and could at the same time be a powerful tool to study the NFRHT in mesoscopic physics or to make calculations of NFRHT between objects of arbitrary shape. Using the Chapman-Kolmogorov equation for the local temperature field, a Fokker-Planck equation can be derived and written in the hydrodynamic limit as an advection-diffusion equation that depends on directly measurable macroscopic quantities like the effective diffusion coefficient and that could be easily solved with standard numerical methods.

When it comes to recent exploration of the spin and angular momentum of thermally fluctuating fields, nearly all investigations have focused on single particles or semi-infinite materials. However, a corresponding general N-body theory should be straightforwardly derived using the general framework presented in this review. This extension could pave the way to studies of thermal-field spin and angular momentum transport in atomic and molecular systems. Since magneto-optical effects based on the use of magneto-optical materials or Weyl semimetals reported thus far have been relatively small, further studies aimed at enhancing these effects should be considered in the future, for instance, by exploiting ferromagnetic or more strongly magnetic materials.

Non-Hermitian physics has attracted significant interest over the past decade from a variety of fields in classical physics due to its mathematical equivalence with the Schrödinger equation, thus allowing one to mimic non-Hermitian wave physics with classical systems. Bipartite plasmonic and phonon-polaritonic many-body systems provide a natural platform to investigate such physics. Among their many peculiarities, one might point to the existence of original topological states that give rise to Berry-like phases and that may lead to the development of new materials such as topological insulators. These states and their consequences for thermal management (active control of heat flux, heat pumping, and heat-flux focusing) remain largely unexplored in many-body systems.

Out-of-equilibrium thermodynamics of many-body systems and its connections to information theory are also future fields of investigation. In systems with long-range interactions, classical thermodynamic theory fails to describe the evolution of state variables since they cannot be sequenced in small independent parts. Normally, to calculate thermodynamic properties it is necessary to determine the microscopic states of a given system. However, a phenomenological approach analogous to Landau's transition theory may be employed to study the thermodynamic behavior of these systems by considering macroscopic quantities. Hence, mechanisms such as phase transitions in magneto-optical systems could be investigated by analyzing the dependence of quantities like the thermal conductance or the entropy flux with order parameters such as the magnitude or orientation of a magnetic field.

The peculiarities of heat transfer in many-body systems have given rise to numerous developments in the emerging field of thermotronics to manipulate heat flux in analogy with electric currents in electric circuits. This radical change of paradigm opens the way to a new generation of devices for active thermal management, to innovative wireless sensors using heat as their primary source of energy, and to low-electricity technologies capable of information processing. In these devices, infrared emission coming from various systems (people, machines, and electric devices) may be captured by active thermal components to launch a sequence of logical operations in order to control the heat propagation (modulate, amplify, or split), trigger specific actions (opto-thermomechanical coupling with MEMS, thermal energy storage, etc.), or even process information. Hence, the development of thermal logical circuits such as neural networks could open the door to a low-power or even zero-power communication technology for the Internet of things, allowing machine-to-machine communication with heat. The design of thermal metamaterials such as thermal insulators, topological insulators, and superdiffusive solids is also a promising challenge.

Finally, building experimental platforms based on multitip scanning thermal microscopy (SThM) setups, suspended membranes, or even networks of electromechanical systems interacting at the nanometer scale will be one of the most important challenges in the next few years to measure the NFRHT in many-body systems, prove all already predicted effects, and develop operational devices. To be able to access conductance variations of a few nW K^{-1}, highly sensitive heat-flux sensors must be developed. This will require the fabrication of thermometers able to work at the nanoscale and measure temperatures with an accuracy < 10 mK.

ACKNOWLEDGMENTS

We thank all of our colleagues within the nanoscale heat-transfer community who engaged us in many fruitful interactions and spirited discussions. S.-A. B. acknowledges support from the Heisenberg Programme of the Deutsche Forschungsgemeinschaft [(DFG), German Research Foundation] under Project No. 404073166. A. W. R. acknowledges support from the National Science Foundation under Grants No. DMR 1454836, No. DMR 1420541, No. DGE 1148900, and No. EFMA 1640986, the Cornell Center for Materials Research MRSEC (Grant No. DMR1719875), and the Defense Advanced Research Projects Agency (DARPA) under Agreement No. HR00112090011. J. C. C. acknowledges funding from the Spanish Ministry of Economy and Competitiveness (MINECO) (Contract No. FIS2017-84057-P). P. B.-A. acknowledges support from the Natural Sciences and Engineering Research Council of Canada through RGPIN-2017 Program No. 05445, and from the Agence Nationale de la Recherche in France through ComputHeat Project No. ANR-19-MRS1-0009.

REFERENCES

Agarwal, G. S., 1975a, Phys. Rev. A **11**, 230.

Agarwal, G. S., 1975b, Phys. Rev. A **11**, 253.

Albaladejo, S., R. Gómez-Medina, L. S. Froufe-Pérez, H. Marinchio, R. Carminati, J. F. Torrado, G. Armelles, A. García-Martín, and J. J. Sáenz, 2010, Opt. Express **18**, 3556.

Asheichyk, K., and M. Krüger, 2018, Phys. Rev. B **98**, 195401.

Asheichyk, K., B. Müller, and M. Krüger, 2017, Phys. Rev. B **96**, 155402.

Baibich, M. N., J. M. Broto, A. Fert, F. Nguyen Van Dau, F. Petroff, P. Etienne, G. Creuzet, A. Friederich, and J. Chazelas, 1988, Phys. Rev. Lett. **61**, 2472.

Barton, G., 2016, J. Stat. Phys. **165**, 1153.

Basu, S., Y.-B. Chen, and Z. M. Zhang, 2007, Int. J. Environ. Res. **31**, 689.

Basu, S., and M. Francoeur, 2011, Appl. Phys. Lett. **98**, 243120.

Basu, S., and S. Z. M. Zhang, 2009, Appl. Phys. Lett. **95**, 133104.

Basu, S., Z. M. Zhang, and C. J. Fu, 2009, Int. J. Environ. Res. **33**, 1203.

Becerril, D., and C. Noguez, 2019, Phys. Rev. B **99**, 045418.

Ben-Abdallah, P., 2006, Appl. Phys. Lett. **89**, 113117.

Ben-Abdallah, P., 2016, Phys. Rev. Lett. **116**, 084301.

Ben-Abdallah, P., 2019a, Phys. Rev. B **99**, 201406.

Ben-Abdallah, P., 2019b, Phys. Rev. Lett. **123**, 264301.

Ben-Abdallah, P., A. Belarouci, L. Frechette, and S.-A. Biehs, 2015, Appl. Phys. Lett. **107**, 053109.

Ben-Abdallah, P., and S.-A. Biehs, 2014, Phys. Rev. Lett. **112**, 044301.

Ben-Abdallah, P., and S.-A. Biehs, 2015, AIP Adv. **5**, 053502.

Ben-Abdallah, P., and S.-A. Biehs, 2016, Phys. Rev. B **94**, 241401 (R).

Ben-Abdallah, P., and S.-A. Biehs, 2017, Z. Naturforsch. A **72**, 151.

Ben-Abdallah, P., and S.-A. Biehs, 2019, Z. Naturforsch. A **74**, 689.

Ben-Abdallah, P., S.-A. Biehs, and K. Joulain, 2011, Phys. Rev. Lett. **107**, 114301.

Ben-Abdallah, P., and S.-A Biehs, 2013, Appl. Phys. Lett. **103**, 191907.

Ben-Abdallah, P., and K. Joulain, 2010, Phys. Rev. B **82**, 121419(R).

Ben-Abdallah, P., K. Joulain, J. Drevillon, and G. Domingues, 2009a, J. Appl. Phys. **106**, 044306.

Ben-Abdallah, P., K. Joulain, J. Drevillon, and G. Domingues, 2009b, Appl. Phys. Lett. **94**, 153117.

Ben-Abdallah, P., K. Joulain, J. Drevillon, and C. Le Goff, 2008, Phys. Rev. B **77**, 075417.

Ben-Abdallah, P., K. Joulain, and A. Pryamikov, 2010, Appl. Phys. Lett. **96**, 143117.

Ben-Abdallah, P., R. Messina, S.-A. Biehs, M. Tschikin, K. Joulain, and C. Henkel, 2013, Phys. Rev. Lett. **111**, 174301.

Bergman, T. L., F. P. Incropera, D. P. DeWitt, and A. S. Lavine, 2011, *Fundamentals of Heat and Mass Transfer* (John Wiley & Sons, New York).

Bernardi, M. P., D. Milovich, and M. Francoeur, 2016, Nat. Commun. **7**, 12900.

Biehs, S.-A., 2007, Eur. Phys. J. B **58**, 423.

Biehs, S.-A., and G. S. Agarwal, 2013a, J. Opt. Soc. Am. B **30**, 700.

Biehs, S.-A., and G. S. Agarwal, 2013b, Appl. Phys. Lett. **103**, 243112.

Biehs, S.-A., and P. Ben-Abdallah, 2016, Phys. Rev. B **93**, 165405.

Biehs, S.-A., and P. Ben-Abdallah, 2017, Z. Naturforsch. A **72**, 115.

Biehs, S.-A., P. Ben-Abdallah, F. S. S. Rosa, K. Joulain, and J.-J. Greffet, 2011, Opt. Express **19**, A1088.

Biehs, S.-A., and J.-J. Greffet, 2010a, Phys. Rev. Lett. **105**, 234301.

Biehs, S.-A., and J.-J. Greffet, 2010b, Phys. Rev. B **82**, 245410.

Biehs, S.-A., and J.-J. Greffet, 2010c, Phys. Rev. B **81**, 245414.

Biehs, S.-A., O. Huth, and F. Rüting, 2008, Phys. Rev. B **78**, 085414.

Biehs, S.-A., O. Huth, F. Rüting, and M. Holthaus, 2010, J. Appl. Phys. **108**, 014312.

Biehs, S.-A., S. Lang, A. Yu. Petrov, M. Eich, and P. Ben-Abdallah, 2015, Phys. Rev. Lett. **115**, 174301.

Biehs, S.-A., V. M. Menon, and G. S. Agarwal, 2016, Phys. Rev. B **93**, 245439.

Biehs, S.-A., D. Reddig, and M. Holthaus, 2007, Eur. Phys. J. B **55**, 237.

Biehs, S.-A., M. Tschikin, and P. Ben-Abdallah, 2012, Phys. Rev. Lett. **109**, 104301.

Biehs, S.-A., M. Tschikin, R. Messina, and P. Ben-Abdallah, 2013, Appl. Phys. Lett. **102**, 131106.

Bimonte, G., 2009, Phys. Rev. A **80**, 042102.

Bimonte, G., T. Emig, M. Kardar, and M. Krüger, 2017, Annu. Rev. Condens. Matter Phys. **8**, 119.

Bliokh, K., and F. Nori, 2012, Phys. Rev. A **85**, 061801(R).

Bliokh, K. Y., and F. Nori, 2015, Phys. Rep. **592**, 1.

Boehm, R. F., and C. L. Tien, 1970, J. Heat Transfer **92**, 405.

Bouchet, D., D. Cao, R. Carminati, Y. De Wilde, and V. Krachmalnicoff, 2016, Phys. Rev. Lett. **116**, 037401.

Caloz, C., A. Alù, S. Tretyakov, D. Sounas, K. Achouri, and Z.-L. Deck-Léger, 2018, Phys. Rev. Applied **10**, 047001.

Castanié, E., R. Vincent, R. Pierrat, and R. Carminati, 2012, Int. J. Opt. **2012**, 452047.

Chapuis, P.-O., M. Laroche, S. Volz, and J.-J. Greffet, 2008a, Appl. Phys. Lett. **92**, 201906.

Chapuis, P.-O., M. Laroche, S. Volz, and J.-J. Greffet, 2008b, Phys. Rev. B **77**, 125402.

Chapuis, P.-O., S. Volz, C. Henkel, K. Joulain, and J.-J. Greffet, 2008, Phys. Rev. B **77**, 035431.

Chen, K., P. Santhanam, and S. Fan, 2016, Phys. Rev. Applied **6**, 024014.

Chen, K., P. Santhanam, S. Sandhu, L. Zhu, and S. Fan, 2015, Phys. Rev. B **91**, 134301.

Chen, Y., and Y. Xuan, 2015, J. Quant. Spectrosc. Radiat. Transfer **158**, 52.

Chiloyan, V., J. Garg, K. Esfarjani, and G. Chen, 2015, Nat. Commun. **6**, 6755.

Chiu, K. W., and J. J. Quinn, 1972, Nuovo Cimento Soc. Ital. Fis. B **10**, 1.

Choubdar, O. R., and M. Nikbakht, 2016, J. Appl. Phys. **120**, 144303.

Cravalho, E. G., C. L. Tien, and R. P. Caren, 1967, J. Heat Transfer **89**, 351.

Cuevas, C., and E. Scheer, 2017, *Molecular Electronics: An Introduction to Theory and Experiment* (World Scientific, Singapore).

Cuevas, J. C., and F. J. García-Vidal, 2018, ACS Photonics **5**, 3896.

Cui, L., S. Hur, Z. A. Akbar, J. C. Klöckner, W. Jeong, F. Pauly, S.-Y. Jang, P. Reddy, and E. Meyhofer, 2019, Nature (London) **572**, 628.

Cui, L., W. Jeong, V. Fernández-Hurtado, J. Feist, F. J. García-Vidal, J. C. Cuevas, E. Meyhofer, and P. Reddy, 2017, Nat. Commun. **8**, 14479.

Cui, L., W. Jeong, S. Hur, M. Matt, J. C. Klöckner, F. Pauly, P. Nielaba, J. C. Cuevas, E. Meyhofer, and P. Reddy, 2017, Science **355**, 1192.

Czapla, B., and A. Narayanaswamy, 2019, J. Quant. Spectrosc. Radiat. Transfer **227**, 4.

Dai, J., S. A. Dyakov, S. I. Bozhevolnyi, and M. Yan, 2016, Phys. Rev. B **94**, 125431.

Dai, J., S. A. Dyakov, and M. Yan, 2015, Phys. Rev. B **92**, 035419.

Dai, J., S. A. Dyakov, and M. Yan, 2016, Phys. Rev. B **93**, 155403.

Danz, N., R. Waldhusl, A. Bruer, and R. Kowarschik, 2002, J. Opt. Soc. Am. B **19**, 412.

Datta, S., 1997, *Electronic Transport in Mesoscopic Systems* (Cambridge University Press, Cambridge, England).

Dedkov, G. V., and A. A. Kyasov, 2007, Tech. Phys. Lett. **33**, 305.

Dedkov, G. V., and A. A. Kyasov, 2011, Europhys. Lett. **93**, 34001.

Deshmukh, R., S.-A. Biehs, E. Khwaja, T. Galfsky, G. S. Agarwal, and V. M. Menon, 2018, ACS Photonics **5**, 2737.

DeSutter, J., L. Tang, and M. Francoeur, 2019, Nat. Nanotechnol. **14**, 751.

Domingues, G., S. Volz, K. Joulain, and J.-J. Greffet, 2005, Phys. Rev. Lett. **94**, 085901.

Domoto, G. A., R. F. Boehm, and C. L. Tien, 1970, J. Heat Transfer **92**, 412.

Domoto, G. A., and C. L. Tien, 1970, J. Heat Transfer **92**, 399.

Dong, J., J. Zhao, and L. Liu, 2017a, Phys. Rev. B **95**, 125411.

Dong, J., J. M. Zhao, and L. H. Liu, 2017b, J. Quant. Spectrosc. Radiat. Transfer **197**, 114.

Dong, J., J. Zhao, and L. Liu, 2018, Phys. Rev. B **97**, 075422.

Dorofeyev, I., H. Fuchs, and J. Jersch, 2002, Phys. Rev. E **65**, 026610.

Dorofeyev, I. A., 1998, J. Phys. D **31**, 600.

Dorofeyev, I. A., and E. A. Vinogradov, 2011, Phys. Rep. **504**, 75.

Draine, B. T., 1988, Astrophys. J. **333**, 848.

Dyakov, S. A., J. Dai, M. Yan, and M. Qiu, 2015a, Appl. Phys. Lett. **106**, 064103.

Dyakov, S. A., J. Dai, M. Yan, and M. Qiu, 2015b, J. Phys. D **48**, 305104.

Dyakov, S. A., V. A. Semenenko, N. A. Gippius, and S. G. Tikhodeev, 2018, Phys. Rev. B **98**, 235416.

Dye-Zone, A., A. Narayanaswamy, and G. Chen, 2005, Phys. Rev. B **72**, 155435.

Eckhardt, W., 1982, Z. Phys. B **46**, 85.

Eckhardt, W., 1984, Phys. Rev. A **29**, 1991.

Edalatpour, S., M. Čuma, T. Trueax, R. Backman, and M. Francoeur, 2015, Phys. Rev. E **91**, 063307.

Edalatpour, S., J. DeSutter, and M. Francoeur, 2016, J. Quant. Spectrosc. Radiat. Transfer **178**, 14.

Edalatpour, S., and M. Francoeur, 2014, J. Quant. Spectrosc. Radiat. Transfer **133**, 364.

Edalatpour, S., and M. Francoeur, 2016, Phys. Rev. B **94**, 045406.

Ekeroth, R. M. A., P. Ben-Abdallah, J. C. Cuevas, and A. García-Martín, 2018, ACS Photonics **5**, 705.

Ekeroth, R. M. A., A. García-Martín, and J. C. Cuevas, 2017, Phys. Rev. B **95**, 235428.

Fan, L., Y. Guo, G. T. Papadakis, B. Zhao, Z. Zhao, S. Buddhiraju, M. Orenstein, and S. Fan, 2020, Phys. Rev. B **101**, 085407.

Fernández-Hurtado, S., F. J. García-Vidal, S. Fan, and J. C. Cuevas, 2017, Phys. Rev. Lett. **118**, 203901.

Ferreiros, Y., A. A. Zyuzin, and J. H. Bardarson, 2017, Phys. Rev. B **96**, 115202.

Fiorino, A., D. Thompson, L. Zhu, B. Song, P. Reddy, and E. Meyhofer, 2018, Nano Lett. **18**, 3711.

Fiorino, A., L. Zhu, D. Thompson, R. Mittapally, P. Reddy, and E. Meyhofer, 2018, Nat. Nanotechnol. **13**, 806.

Fiorino, A., *et al.*, 2018, ACS Nano **12**, 5774.

Francoeur, M., M. P. Mengüç, and R. Vaillon, 2008, Appl. Phys. Lett. **93**, 043109.

Francoeur, M., M. P. Mengüç, and R. Vaillon, 2009, J. Quant. Spectrosc. Radiat. Transfer **110**, 2002.

Francoeur, M., M. P. Mengüç, and R. Vaillon, 2010a, J. Phys. D **43**, 075501.

Francoeur, M., M. P. Mengüç, and R. Vaillon, 2010b, J. Appl. Phys. **107**, 034313.

Francoeur, M., M. P. Mengüç, and R. Vaillon, 2011, Phys. Rev. B **84**, 075436.

Fujimoto, S., 2009, Phys. Rev. Lett. **103**, 047203.

Ghashami, M., H. Geng, T. Kim, N. Iacopino, S. K. Cho, and K. Park, 2018, Phys. Rev. Lett. **120**, 175901.

Golyk, V. A., M. Krüger, and M. Kardar, 2013, Phys. Rev. B **88**, 155117.

Gu, W., G.-H. Tang, and W.-Q. Tao, 2015, Int. J. Heat Mass Transfer **82**, 429.

Gu, Y., and K. G. Kornev, 2010, J. Opt. Soc. Am. B **27**, 2165.

Guérout, R., J. Lussange, F. S. S. Rosa, J.-P. Hugonin, S. A. R. Dalvit, J.-J. Greffet, A. Lambrecht, and S. Reynaud, 2012, Phys. Rev. B **85**, 180301.

Guha, B., C. Otey, C. B. Poitras, S. Fan, and M. Lipson, 2012, Nano Lett. **12**, 4546.

Guo, Y., G. L. Cortes, S. Molesky, and Z. Jacob, 2012, Appl. Phys. Lett. **101**, 131106.

Guo, Y., and Z. Jacob, 2013, Opt. Express **21**, 15014.

Guo, Y., and Z. Jacob, 2014, J. Appl. Phys. **115**, 234306.

Hall, E. H., 1879, Am. J. Math. **2**, 287.

Hargreaves, C. M., 1969, Phys. Lett. **30A**, 491.

Harrington, R. F., 1989, J. Electromagn. Waves Appl. **3**, 1.

He, M.-J., H. Qi, Y. Li, Y.-T. Ren, W.-H. Cai, and L.-M. Ruan, 2019, Int. J. Heat Mass Transfer **137**, 12.

He, M.-J., H. Qi, Y.-T. Ren, Y.-J. Zhao, and M. Antezza, 2019, Appl. Phys. Lett. **115**, 263101.

He, M.-J., H. Qi, Y.-F. Wang, Y.-T. Ren, W.-H. Cai, and Li-M. Ruan, 2019, Opt. Express **27**, A954.

Herz, F., and S.-A. Biehs, 2019, Europhys. Lett. **127**, 44001.

Howell, J. R., M. P. Mengüç, and R. Siegel, 2016, *Thermal Radiation Heat Transfer* (CRC Press, Boca Raton).

Hu, L., A. Narayanaswamy, X. Chen, and G. Chen, 2008, Appl. Phys. Lett. **92**, 133106.

Huang, Z.-M., B. Han, and M. Stone, 2020, Phys. Rev. B **101**, 125201.

Hugonin, J.-P., M. Besbes, and P. Ben-Abdallah, 2015, Phys. Rev. B **91**, 180202.

Huth, O., F. Rüting, S.-A. Biehs, and M. Holthaus, 2010, Eur. Phys. J. Appl. Phys. **50**, 10603.

Iizuka, H., and S. Fan, 2018, Phys. Rev. Lett. **120**, 063901.

Ilic, O., M. Jablan, J. D. Joannopoulos, I. Celanovic, H. Buljan, and M. Soljačić, 2012a, Phys. Rev. B **85**, 155422.

Ilic, O., M. Jablan, J. D. Joannopoulos, I. Celanovic, and M. Soljačić, 2012b, Opt. Express **20**, A366.

Imry, Y., and R. Landauer, 1999, Rev. Mod. Phys. **71**, S306.

Incardone, R., T. Emig, and M. Krüger, 2014, Europhys. Lett. **106**, 41001.

Inyushkin, A. V., and A. N. Taldenkov, 2007, JETP Lett. **86**, 379–382.

Ito, K., A. Miura, H. Iizuka, and H. Toshiyoshi, 2015, Appl. Phys. Lett. **106**, 083504.

Ito, K., K. Nishikawa, H. Iizuka, and H. Toshiyoshi, 2014, Appl. Phys. Lett. **105**, 253503.

Ito, K., K. Nishikawa, A. Miura, H. Toshiyoshi, and H. Iizuka, 2017, Nano Lett. **17**, 4347.

Janowicz, M., D. Reddig, and M. Holthaus, 2003, Phys. Rev. A **68**, 043823.

Jin, W., R. Messina, and A. W. Rodriguez, 2017a, Opt. Express **25**, 14746.

Jin, W., R. Messina, and A. W. Rodriguez, 2017b, Phys. Rev. B **95**, 161409.

Jin, W., S. Molesky, Z. Lin, and A. W. Rodriguez, 2019, Phys. Rev. B **99**, 041403.

Jin, W., A. G. Polimeridis, and A. W. Rodriguez, 2016, Phys. Rev. B **93**, 121403.

Joulain, K., R. Carminati, J.-P. Mulet, and J.-J. Greffet, 2003, Phys. Rev. B **68**, 245405.

Joulain, K., J. Drevillon, and P. Ben-Abdallah, 2010, Phys. Rev. B **81**, 165119.

Joulain, K., Y. Ezzahri, J. Drevillon, and P. Ben-Abdallah, 2015, Appl. Phys. Lett. **106**, 133505.

Joulain, K., J.-P. Mulet, F. Marquier, R. Carminati, and J.-J. Greffet, 2005, Surf. Sci. Rep. **57**, 59.

Kan, Y. H., C. Y. Zhao, and Z. M. Zhang, 2019, Phys. Rev. B **99**, 035433.

Karplus, R., and J. M. Luttinger, 1954, Phys. Rev. **95**, 1154.

Kathmann, C., R. Messina, P. Ben-Abdallah, and S.-A. Biehs, 2018, Phys. Rev. B **98**, 115434.

Kathmann, C., M. Reina, R. Messina, P. Ben-Abdallah, and S.-A. Biehs, 2020, Sci. Rep. **10**, 3596.

Katsura, H., N. Nagaosa, and P. A. Lee, 2010, Phys. Rev. Lett. **104**, 066403.

Kemp, J. C., 1970, Astrophys. J. **162**, 169.

Kemp, J. C., J. B. Swedlund, J. D. Landstreet, and J. R. P. Angel, 1970, Astrophys. J. **161**, L77.

Khandekar, C., and Z. Jacob, 2019a, New J. Phys. **21**, 103030.

Khandekar, C., and Z. Jacob, 2019b, Phys. Rev. Applied **12**, 014053.

Khandekar, C., and A. W. Rodriguez, 2017, Appl. Phys. Lett. **111**, 083104.

Kim, K., *et al.*, 2015, Nature (London) **528**, 387.

Kittel, A., W. Müller-Hirsch, J. Parisi, S.-A. Biehs, D. Reddig, and M. Holthaus, 2005, Phys. Rev. Lett. **95**, 224301.

Kittel, A., U. Wischnath, J. Welker, O. Huth, F. Rüting, and S.-A. Biehs, 2008, Appl. Phys. Lett. **93**, 193109.

Klimchitskaya, G. L., and V. M. Mostepanenko, 2015, Phys. Rev. B **91**, 045412.

Kloppstech, K., N. Könne, S.-A. Biehs, A. W. Rodriguez, L. Worbes, D. Hellmann, and A. Kittel, 2017, Nat. Commun. **8**, 14475.

Kollyukh, O. G., A. I. Liptuga, V. Morozhenko, and V. I. Pipa, 2005, Phys. Rev. B **71**, 073306.

Komiyama, S., 2019, J. Appl. Phys. **125**, 010901.

Kralik, T., P. Hanzelka, M. Zobac, V. Musilova, T. Fort, and M. Horak, 2012, Phys. Rev. Lett. **109**, 224302.

Králík, T., V. Musilová, T. Fořt, and A. Srnka, 2017, Phys. Rev. B **95**, 060503(R).

Krüger, M., G. Bimonte, T. Emig, and M. Kardar, 2012, Phys. Rev. B **86**, 115423.

Krüger, M., T. Emig, and M. Kardar, 2011, Phys. Rev. Lett. **106**, 210404.

Krüger, M., V. A. Golyk, G. Bimonte, and M. Kardar, 2013, Europhys. Lett. **104**, 41001.

Kubo, R., 1966, Rep. Prog. Phys. **29**, 255.

Kubytskyi, V., S.-A. Biehs, and P. Ben-Abdallah, 2014, Phys. Rev. Lett. **113**, 074301.

Lakhtakia, A., 1992, Int. J. Mod. Phys. C **03**, 583.

Lakhtakia, A., V. K. Varadan, and V. V. Varadan, 1991, Int. J. Infrared Millim. Waves **12**, 1253.

Lang, S., G. Sharma, S. Molesky, P. U. Kränzien, T. Jalas, Z. Jacob, A. Yu. Petrov, and M. Eich, 2017, Sci. Rep. **7**, 13916.

Lang, S., M. Tschikin, S.-A. Biehs, A. Yu. Petrov, and M. Eich, 2014, Appl. Phys. Lett. **104**, 121903.

Langlais, M., J.-P. Hugonin, M. Besbes, and P. Ben-Abdallah, 2014, Opt. Express **22**, A577.

Laroche, M., R. Carminati, and J.-J. Greffet, 2006, J. Appl. Phys. **100**, 063704.

Latella, I., P. Ben-Abdallah, S.-A. Biehs, M. Antezza, and R. Messina, 2017, Phys. Rev. B **95**, 205404.

Latella, I., S.-A. Biehs, R. Messina, A. W. Rodriguez, and P. Ben-Abdallah, 2018, Phys. Rev. B **97**, 035423.

Latella, I., O. Marconot, J. Sylvestre, L. G. Frechette, and P. Ben-Abdallah, 2019, Phys. Rev. Applied **11**, 024004.

Latella, I., R. Messina, S.-A. Biehs, J. M. Rubi, and P. Ben-Abdallah, 2020, Sci. Rep. **10**, 8938.

Latella, I., R. Messina, J. M. Rubi, and P. Ben-Abdallah, 2018, Phys. Rev. Lett. **121**, 023903.

Latella, I., A. Pérez-Madrid, J. M. Rubi, S.-A. Biehs, and P. Ben-Abdallah, 2015, Phys. Rev. Applied **4**, 011001.

Latella, I., A. Prez-Madrid, L. C. Lapas, and J. M. Rubi, 2014, J. Appl. Phys. **115**, 124307.

Latella, Ivan, and Philippe Ben-Abdallah, 2017, Phys. Rev. Lett. **118**, 173902.

Lau, W. T., J.-T. Shen, and S. Fan, 2009, Phys. Rev. B **80**, 155135.

Lau, W. T., J.-T. Shen, G. Veronis, S. Fan, and P. V. Braun, 2008, Appl. Phys. Lett. **92**, 103106.

Leduc, M. A., 1887, J. Phys. 2e Ser. **6**, 378.

Lévy, P., 1937, *Théorie de l'Addition des Variables Aléatoires* (Gauthier-Villars, Paris).

Li, B., L. Wang, and G. Casati, 2006, Appl. Phys. Lett. **88**, 143501.

Lim, M., S. S. Lee, and B. J. Lee, 2013, Opt. Express **21**, 22173.

Lim, M., S. S. Lee, and B. J. Lee, 2015, Phys. Rev. B **91**, 195136.

Liu, J., and E. Narimanov, 2015, Phys. Rev. B **91**, 041403(R).

Liu, X., J. Shen, and Y. Xuan, 2019, Nanoscale Microscale Thermophys. Eng. **23**, 188.

Liu, X., R. Z. Zhang, and Z. M. Zhang, 2013, Appl. Phys. Lett. **103**, 213102.

Liu, X., R. Z. Zhang, and Z. Zhang, 2014a, ACS Photonics **1**, 785.

Liu, X., R. Z. Zhang, and Z. M. Zhang, 2014b, Int. J. Heat Mass Transfer **73**, 389.

Liu, X., and Z. M. Zhang, 2015a, ACS Photonics **2**, 1320.

Liu, X., and Z. M. Zhang, 2015b, Appl. Phys. Lett. **107**, 143114.

Liu, X., B. Zhao, and Z. M. Zhang, 2015, Phys. Rev. A **91**, 062510.

Luo, C., A. Narayanaswamy, G. Chen, and J. D. Joannopoulos, 2004, Phys. Rev. Lett. **93**, 213905.

Luo, M., J. Dong, J. Zhao, L. Liu, and M. Antezza, 2019, Phys. Rev. B **99**, 134207.

Manjavacas, A., and F. J. G. de Abajo, 2012, Phys. Rev. B **86**, 075466.

Martynenko, Y. V., and L. I. Ognev, 2005, Tech. Phys. **50**, 1522.

Maslovski, S. I., C. R. Simovski, and S. A. Tretyakov, 2013, Phys. Rev. B **87**, 155124.

McCauley, A. P., M. T. H. Reid, M. Krüger, and S. G. Johnson, 2012, Phys. Rev. B **85**, 165104.

Menges, F., M. Dittberner, L. Novotny, D. Passarello, S. S. P. Parkin, M. Spieser, H. Riel, and B. Gotsmann, 2016, Appl. Phys. Lett. **108**, 171904.

Messina, R., and M. Antezza, 2011a, Europhys. Lett. **95**, 61002.

Messina, R., and M. Antezza, 2011b, Phys. Rev. A **84**, 042102.

Messina, R., and M. Antezza, 2014, Phys. Rev. A **89**, 052104.

Messina, R., M. Antezza, and P. Ben-Abdallah, 2012, Phys. Rev. Lett. **109**, 244302.

Messina, R., and P. Ben-Abdallah, 2013, Sci. Rep. **3**, 1383.

Messina, R., and P. Ben-Abdallah, 2020, Phys. Rev. B **101**, 165435.

Messina, R., P. Ben-Abdallah, B. Guizal, and M. Antezza, 2017, Phys. Rev. B **96**, 045402.

Messina, R., P. Ben-Abdallah, B. Guizal, M. Antezza, and S.-A. Biehs, 2016, Phys. Rev. B **94**, 104301.

Messina, R., S.-A. Biehs, and P. Ben-Abdallah, 2018, Phys. Rev. B **97**, 165437.

Messina, R., J.-P. Hugonin, J. J. Greffet, F. Marquier, Y. De Wilde, A. Belarouci, L. Frechette, Y. Cordier, and P. Ben-Abdallah, 2013, Phys. Rev. B **87**, 085421.

Messina, R., W. Jin, and A. W. Rodriguez, 2016, Phys. Rev. B **94**, 121410.

Messina, R., A. Noto, B. Guizal, and M. Antezza, 2017, Phys. Rev. B **95**, 125404.

Messina, R., M. Tschikin, S.-A. Biehs, and P. Ben-Abdallah, 2013, Phys. Rev. B **88**, 104307.

Miller, D. A. B., 2000, Appl. Opt. **39**, 1681.

Miller, D. A. B., 2007, J. Opt. Soc. Am. B **24**, A1.

Miller, O. D., S. G. Johnson, and A. W. Rodriguez, 2014, Phys. Rev. Lett. **112**, 157402.

Miller, O. D., S. G. Johnson, and A. W. Rodriguez, 2015, Phys. Rev. Lett. **115**, 204302.

Miller, O. D., A. G. Polimeridis, M. T. H. Reid, C. W. Hsu, B. G. DeLacy, J. D. Joannopoulos, M. Soljačić, and S. G. Johnson, 2016, Opt. Express **24**, 3329.

Modest, M. F., 2013, *Radiative Heat Transfer* (Academic Press, New York).

Molesky, S., P. S. Venkataram, W. Jin, and A. W. Rodriguez, 2020, Phys. Rev. B **101**, 035408.

Moncada-Villa, E., and J. C. Cuevas, 2020, Phys. Rev. B **101**, 085411.

Moncada-Villa, E., V. Fernández-Hurtado, F. J. García-Vidal, A. García-Martín, and J. C. Cuevas, 2015, Phys. Rev. B **92**, 125418.

Mosso, N., U. Drechsler, F. Menges, P. Nirmalraj, S. Karg, H. Riel, and B. Gotsmann, 2017, Nat. Nanotechnol. **12**, 430.

Mulet, J.-P., K. Joulain, R. Carminati, and J.-J. Greffet, 2001, Appl. Phys. Lett. **78**, 2931.

Mulet, J.-P., K. Joulain, R. Carminati, and J.-J. Greffet, 2002, Microscale Thermophys. Eng. **6**, 209.

Müller, B., R. Incardone, M. Antezza, T. Emig, and M. Krüger, 2017, Phys. Rev. B **95**, 085413.

Musilová, V., T. Králík, T. Fořt, and M. Macek, 2019, Phys. Rev. B **99**, 024511.

Nagaosa, N., J. Sinova, S. Onoda, A. H. MacDonald, and N. P. Ong, 2010, Rev. Mod. Phys. **82**, 1539.

Narayanaswamy, A., and G. Chen, 2003, Appl. Phys. Lett. **82**, 3544.

Narayanaswamy, A., and G. Chen, 2005, J. Quant. Spectrosc. Radiat. Transfer **93**, 175.

Narayanaswamy, A., and G. Chen, 2008, Phys. Rev. B **77**, 075125.

Narayanaswamy, A., S. Shen, and G. Chen, 2008, Phys. Rev. B **78**, 115303.

Nefedov, I. S., and C. R. Simovski, 2011, Phys. Rev. B **84**, 195459.

Neto, A. H Castro, F. Guinea, N. M. R. Peres, K. S. Novoselov, and A. K. Geim, 2009, Rev. Mod. Phys. **81**, 109.

Newman, W. D., C. L. Cortes, A. Afshar, K. Cadien, A. Meldrum, R. Fedosejevs, and Z. Jacob, 2018, Sci. Adv. **4**, eaar5278.

Nikbakht, M., 2014, J. Appl. Phys. **116**, 094307.

Nikbakht, M., 2015, Europhys. Lett. **110**, 14004.

Nikbakht, M., 2017, Phys. Rev. B **96**, 125436.

Novotny, L., and B. Hecht, 2006, *Principles of Nano-Optics* (Cambridge University Press, Cambridge, England).

Onose, Y., T. Ideue, H. Katsura, Y. Shiomi, N. Nagaosa, and Y. Tokura, 2010, Science **329**, 297–299.

Onsager, L., 1931, Phys. Rev. **37**, 405.

Ordonez-Miranda, J., L. Tranchant, S. Gluchko, and S. Volz, 2015, Phys. Rev. B **92**, 115409.

Ordonez-Miranda, J., L. Tranchant, K. Joulain, Y. Ezzahri, J. Drevillon, and S. Volz, 2016, Phys. Rev. B **93**, 035428.

Otey, C., and S. Fan, 2011, Phys. Rev. B **84**, 245431.

Otey, C. R., W. T. Lau, and S. Fan, 2010, Phys. Rev. Lett. **104**, 154301.

Otey, C. R., L. Zhu, S. Sandhu, and S. Fan, 2014, J. Quant. Spectrosc. Radiat. Transfer **132**, 3.

Ott, A., P. Ben-Abdallah, and S.-A. Biehs, 2018, Phys. Rev. B **97**, 205414.

Ott, A., and S.-A. Biehs, 2020, Phys. Rev. B **101**, 155428.

Ott, A., S.-A. Biehs, and P. Ben-Abdallah, 2020, Phys. Rev. B **101**, 241411(R).

Ott, A., R. Messina, P. Ben-Abdallah, and S.-A. Biehs, 2019a, J. Photonics Energy **9**, 032711.

Ott, A., R. Messina, P. Ben-Abdallah, and S.-A. Biehs, 2019b, Appl. Phys. Lett. **114**, 163105.

Ottens, R. S., V. Quetschke, S. Wise, A. A. Alemi, R. Lundock, G. Mueller, D. H. Reitze, D. B. Tanner, and B. F. Whiting, 2011, Phys. Rev. Lett. **107**, 014301.

Papadakis, G. T., B. Zhao, S. Buddhiraju, and S. Fan, 2019, ACS Photonics **6**, 709.

Pendry, J. B., 1999, J. Phys. Condens. Matter **11**, 6621.

Pendry, J. B., 2000, Phys. Rev. Lett. **85**, 3966.

Pendry, J. B., L. Martin-Moreno, and F. J. Garcia-Vidal, 2004, Science **305**, 847.

Pérez-Madrid, A., J. M. Rubi, and L. C. Lapas, 2008, Phys. Rev. B **77**, 155417.

Pineider, F., G. Campo, V. Bonanni, C. de Julian Fernandez, G. Mattei, A. Caneschi, D. Gatteschi, and C. Sangregorio, 2013, Nano Lett. **13**, 4785.

Planck, M., 1914, *The Theory of Heat Radiation* (Blakiston, Philadelphia).

Poddubny, A., I. Iorsh, P. Belov, and Y. Kivshar, 2013, Nat. Photonics **7**, 948.

Polder, D., and M. van Hove, 1971, Phys. Rev. B **4**, 3303.

Polimeridis, A. G., M. T. H. Reid, W. Jin, S. G. Johnson, J. K. White, and A. W. Rodriguez, 2015, Phys. Rev. B **92**, 134202.

Polimeridis, A. G., M. T. H. Reid, S. G. Johnson, J. K. White, and A. W. Rodriguez, 2015, IEEE Trans. Antennas Propag. **63**, 611.

Poudel, A., X. Chen, and M. A. Ratner, 2016, J. Phys. Chem. Lett. **7**, 955.

Prodhomme, H., J. Ordonez-Miranda, Y. Ezzahri, J. Drévillon, and K. Joulain, 2016, J. Appl. Phys. **119**, 194502.

Prodhomme, H., J. Ordonez-Miranda, Y. Ezzahri, J. Drévillon, and K. Joulain, 2018, J. Quant. Spectrosc. Radiat. Transfer **210**, 52.

Purcell, E. M., and R. C. Pennypacker, 1973, Astrophys. J. **186**, 705.

Raj, B., M. Van de Voorde, and Y. Mahajan, 1995, *Nanotechnology for Energy Sustainability* (Wiley, New York).

Ramirez, F. V., and A. J. H. McGaughey, 2017, Phys. Rev. B **96**, 165428.

Reid, M. T. H., and S. G. Johnson, 2015, IEEE Trans. Antennas Propag. **63**, 3588.

Reid, M. T. H., O. D. Miller, A. G. Polimeridis, A. W. Rodriguez, E. M. Tomlinson, and S. G. Johnson, 2017, arXiv:1708.01985.

Reid, M. T. H., A. W. Rodriguez, and S. G. Johnson, 2013, Proc. IEEE **101**, 531.

Reid, M. T. H., J. White, and S. G. Johnson, 2013, Phys. Rev. A **88**, 022514.

Rengarajan, S. R., and Y. Rahmat-Samii, 2000, IEEE Antennas Propag. Mag. **42**, 122.

Righi, A., 1887, Mem. Acc. Lincei **4**, 433.

Rodriguez, A. W., O. Ilic, P. Bermel, I. Celanovic, J. D. Joannopoulos, M. Soljai, and S. G. Johnson, 2011, Phys. Rev. Lett. **107**, 114302.

Rodriguez, A. W., M. T. H. Reid, and S. G. Johnson, 2013, Phys. Rev. B **88**, 054305.

Rodriguez, A. W., M. T. H. Reid, J. Varela, J. D. Joannopoulos, F. Capasso, and S. G. Johnson, 2013, Phys. Rev. Lett. **110**, 014301.

Rodriguez-Lopez, P., W.-K. Tse, and D. A. R. Dalvit, 2015, J. Phys. Condens. Matter **27**, 214019.

Rousseau, E., A. Siria, G. Jourdan, S. Volz, F. Comin, J. Chevrier, and J.-J. Greffet, 2009, Nat. Photonics **3**, 514.

Rüting, F., S.-A. Biehs, O. Huth, and M. Holthaus, 2010, Phys. Rev. B **82**, 115443.

Rytov, S. M., Y. A. Kravtsov, and V. I. Tatarskii, 1989, *Principles of Statistical Radiophysics 3* (Springer, New York).

Sääskilahti, K., J. Oksanen, and J. Tulkki, 2014, Phys. Rev. B **89**, 134301.

Salihoglu, H., V. Iyer, T. Taniguchi, K. Watanabe, P. D. Ye, and X. Xu, 2019, Adv. Funct. Mater. **30**, 1905830.

Salihoglu, H., W. Nam, L. Traverso, M. Segovia, P. K. Venuthurumilli, W. Liu, Y. Wei, W. Li, and X. Xu, 2020, Nano Lett. **20**, 6091.

Sasihithlu, K., 2018, J. Photonics Energy **9**, 032709.

Sasihithlu, K., and G. S. Agarwal, 2018, Nanophotonics **7**, 1581.

Sasihithlu, K., and A. Narayanaswamy, 2011, Phys. Rev. B, **83**, 161406(R).

Sernelius, B. E., 2012, Phys. Rev. B **85**, 195427.

Shen, S., A. Mavrokefalos, P. Sambegoro, and G. Chen, 2012, Appl. Phys. Lett. **100**, 233114.

Shen, S., A. Narayanaswamy, and G. Chen, 2009, Nano Lett. **9**, 2909.

Shi, J., P. Li, B. Liu, and S. Shen, 2013, Appl. Phys. Lett. **102**, 183114.

Shi, K., F. Bao, and S. He, 2017, ACS Photonics **4**, 971.

Shi, K., R. Liao, G. Cao, F. Bao, and S. He, 2018, Opt. Express **26**, A591.

Shi, K., Y. Sun, Z. Chen, N. He, F. Bao, J. Evans, and S. He, 2019, Nano Lett. **19**, 8082.

Shi, K. Z., F. L. Bao, N. He, and S. L. He, 2019, Int. J. Heat Mass Transfer **134**, 1119.

Shlesinger, M. F., G. M. Zaslavsky, and U. Frisch, 1995, *Lévy Flights and Related Topics in Physics* (Springer-Verlag, Berlin).

Silveirinha, M. G., 2017, Phys. Rev. B **95**, 115103.

Simchi, H., 2017, J. Appl. Phys. **121**, 094301.

Simovski, C., S. Maslovski, I. Nefedov, and S. Tretyakov, 2013, Opt. Express **21**, 14988.

Song, B., A. Fiorino, E. Meyhofer, and P. Reddy, 2015, AIP Adv. **5**, 053503.

Song, B., D. Thompson, A. Fiorino, Y. Ganjeh, P. Reddy, and E. Meyhofer, 2016, Nat. Nanotechnol. **11**, 509.

Song, B., *et al.*, 2015, Nat. Nanotechnol. **10**, 253.

Song, J., Q. Cheng, Z. Luo, X. Zhou, and Z. Zhang, 2019, Int. J. Heat Mass Transfer **140**, 80.

Song, J. L., L. Lu, Q. Cheng, and Z. X. Luo, 2018, J. Heat Transfer **140**, 082005.

St-Gelais, R., L. Zhu, S. Fan, and M. Lipson, 2016, Nat. Nanotechnol. **11**, 515.

St-Gelais, Raphael, Biswajeet Guha, Linxiao Zhu, Shanhui Fan, and Michal Lipson, 2014, Nano Lett. **14**, 6971.

Strohm, C., G. L. J. A. Rikken, and P. Wyder, 2005, Phys. Rev. Lett. **95**, 155901.

Svetovoy, V. B., and G. Palasantzas, 2014, Phys. Rev. Applied **2**, 034006.

Svetovoy, V. B., P. J. van Zwol, and J. Chevrier, 2012, Phys. Rev. B **85**, 155418.

Tervo, E., M. Francoeur, B. A. Cola, and Z. M. Zhang, 2019, Phys. Rev. B **100**, 205422.

Tervo, E. J., O. S. Adewuyi, J. S. Hammonds, and B. A. Cola, 2016, Mater. Horiz. **3**, 434.

Tervo, E. J., B. A. Cola, and Z. M. Zhang, 2020, J. Quant. Spectrosc. Radiat. Transfer **246**, 106947.

Tervo, E. J., M. E. Gustafson, Z. M. Zhang, B. A. Cola, and M. A. Filler, 2019, Appl. Phys. Lett. **114**, 163104.

Thomas, N. H., M. C. Sherrott, J. Broulliet, H. A. Atwater, and A. J. Minnich, 2019, Nano Lett. **19**, 3898.

Thompson, D., L. Zhu, E. Meyhofer, and P. Reddy, 2020, Nat. Nanotechnol. **15**, 99.

Tomchuk, P. M., and N. I. Grigorchuk, 2006, Phys. Rev. B **73**, 155423.

Tretyakov, S., 2014, Plasmonics **9**, 935.

Tschikin, M., P. Ben-Abdallah, and S.-A. Biehs, 2012, Phys. Lett. A **376**, 3462.

Tschikin, M., S.-A. Biehs, P. Ben-Abdallah, S. Lang, A. Yu. Petrov, and M. Eich, 2015, J. Quant. Spectrosc. Radiat. Transfer **158**, 17.

Tschikin, M., S.-A. Biehs, R. Messina, and P. Ben-Abdallah, 2013, J. Opt. **15**, 105101.

Tschikin, M., S.-A. Biehs, P. Ben-Abdallah, and F. S. S. Rosa, 2012, Eur. Phys. J. B **85**, 233.

Van Mechelen, T., and Z. Jacob, 2016, Optica **3**, 118.

van Zwol, P., L. Ranno, and J. Chevrier, 2012, Phys. Rev. Lett. **108**, 234301.

van Zwol, P., S. Thiele, C. Berger, W. A. de Heer, and J. Chevrier, 2012, Phys. Rev. Lett. **109**, 264301.

van Zwol, P. J., K. Joulain, P. Ben Abdallah, J.-J. Greffet, and J. Chevrier, 2011, Phys. Rev. B **83**, 201404.

van Zwol, P. J., K. Joulain, P. Ben-Abdallah, and J. Chevrier, 2011, Phys. Rev. B **84**, 161413.

Velizhanin, K. A., and T. V. Shahbazyan, 2012, Phys. Rev. B **86**, 245432.

Venkataram, P. S., J. Hermann, A. Tkatchenko, and A. W. Rodriguez, 2018, Phys. Rev. Lett. **121**, 045901.

Venkataram, P. S., S. Molesky, W. Jin, and A. W. Rodriguez, 2020, Phys. Rev. Lett. **124**, 013904.

Volokitin, A. I., and B. N. J. Persson, 2001, Phys. Rev. B **63**, 205404.

Volokitin, A. I., and B. N. J. Persson, 2002, Phys. Rev. B **65**, 115419.

Volokitin, A. I., and B. N. J. Persson, 2004, Phys. Rev. B **69**, 045417.

Volokitin, A I., and B. N. J. Persson, 2007, Rev. Mod. Phys. **79**, 1291.

Volokitin, A. I., and B. N. J. Persson, 2011, Phys. Rev. B **83**, 241407.

Wang, J.-S., and J. Peng, 2017, Europhys. Lett. **118**, 24001.

Wang, Y., and J. Wu, 2016, AIP Adv. **6**, 025104.

Weber, W. H., and G. W. Ford, 2004, Phys. Rev. B **70**, 125429.

Weick, G., and D. Weinmann, 2011, Phys. Rev. B **83**, 125405.

Wen, S.-B., 2010, J. Heat Transfer **132**, 072704.

Werner, G. R., C. A. Bauer, and J. R. Cary, 2013, J. Comput. Phys. **255**, 436.

Worbes, L., D. Hellmann, and A. Kittel, 2013, Phys. Rev. Lett. **110**, 134302.

Wunsch, B., T. Stauber, F. Sols, and F. Guinea, 2006, New J. Phys. **8**, 318.

Xiao, S., X. Zhu, B.-H. Li, and N. A. Mortensen, 2016, Front. Phys. **11**, 117801.

Yang, J., W. Du, Y. Su, Y. Fu, S. Gong, S. He, and Y. Ma, 2018, Nat. Commun. **9**, 1.

Yang, Y., S. Basu, and L. Wang, 2013, Appl. Phys. Lett. **103**, 163101.

Yannopapas, V., and N. V. Vitanov, 2013, Phys. Rev. Lett. **110**, 044302.

Zhang, Y., M. Antezza, H.-L. Yi, and H.-P. Tan, 2019, Phys. Rev. B **100**, 085426.

Zhang, Y., H.-L. Yi, and H.-P. Tan, 2018, ACS Photonics **5**, 3739.

Zhang, Y., H.-L. Yi, H.-P. Tan, and M. Antezza, 2019, Phys. Rev. B **100**, 134305.

Zhang, Z. M., 2007, *Nano/Microscale Heat Transfer* (McGraw-Hill, New York).

Zhao, B., K. Chen, S. Buddhiraju, G. Bhatt, M. Lipson, and S. Fan, 2017, Nano Energy **41**, 344.

Zhao, B., B. Guizal, Z. M. Zhang, S. Fan, and M. Antezza, 2017, Phys. Rev. B **95**, 245437.

Zheng, Z. H., and Y. M. Xuan, 2011, Nanoscale Microscale Thermophys. Eng. **15**, 237.

Zhu, L., and S. Fan, 2014, Phys. Rev. B **90**, 220301(R).

Zhu, L., and S. Fan, 2016, Phys. Rev. Lett. **117**, 134303.

Zhu, L., Y. Guo, and S. Fan, 2018, Phys. Rev. B **97**, 094302.

Zundel, L., and A. Manjavacas, 2020, Phys. Rev. Applied **13**, 054054.